



University of Kentucky
UKnowledge

Theses and Dissertations--Electrical and
Computer Engineering

Electrical and Computer Engineering

2015

Hybrid Single and Dual Pattern Structured Light Illumination

Minghao Wang

University of Kentucky, mwa236@g.uky.edu

[Right click to open a feedback form in a new tab to let us know how this document benefits you.](#)

Recommended Citation

Wang, Minghao, "Hybrid Single and Dual Pattern Structured Light Illumination" (2015). *Theses and Dissertations--Electrical and Computer Engineering*. 74.
https://uknowledge.uky.edu/ece_etds/74

This Doctoral Dissertation is brought to you for free and open access by the Electrical and Computer Engineering at UKnowledge. It has been accepted for inclusion in Theses and Dissertations--Electrical and Computer Engineering by an authorized administrator of UKnowledge. For more information, please contact UKnowledge@lsv.uky.edu.

STUDENT AGREEMENT:

I represent that my thesis or dissertation and abstract are my original work. Proper attribution has been given to all outside sources. I understand that I am solely responsible for obtaining any needed copyright permissions. I have obtained needed written permission statement(s) from the owner(s) of each third-party copyrighted matter to be included in my work, allowing electronic distribution (if such use is not permitted by the fair use doctrine) which will be submitted to UKnowledge as Additional File.

I hereby grant to The University of Kentucky and its agents the irrevocable, non-exclusive, and royalty-free license to archive and make accessible my work in whole or in part in all forms of media, now or hereafter known. I agree that the document mentioned above may be made available immediately for worldwide access unless an embargo applies.

I retain all other ownership rights to the copyright of my work. I also retain the right to use in future works (such as articles or books) all or part of my work. I understand that I am free to register the copyright to my work.

REVIEW, APPROVAL AND ACCEPTANCE

The document mentioned above has been reviewed and accepted by the student's advisor, on behalf of the advisory committee, and by the Director of Graduate Studies (DGS), on behalf of the program; we verify that this is the final, approved version of the student's thesis including all changes required by the advisory committee. The undersigned agree to abide by the statements above.

Minghao Wang, Student

Dr. Laurence Hassebrook, Major Professor

Dr. Caicheng Lu, Director of Graduate Studies

HYBRID SINGLE AND DUAL PATTERN STRUCTURED LIGHT ILLUMINATION

DISSERTATION

A dissertation submitted in partial fulfillment of the requirements for the degree of
Doctor of Philosophy in the College of Engineering at the University of Kentucky

By

Minghao Wang

Advisor: Dr. Laurence Hassebrook,
Electrical and Computer Engineering Department

Copyright © Minghao Wang 2015

Abstract of Dissertation

HYBRID SINGLE AND DUAL PATTERN STRUCTURED LIGHT ILLUMINATION

Structured Light Illumination is a widely used 3D shape measurement technique in non-contact surface scanning. Multi-pattern based Structured Light Illumination methods reconstruct 3-D surface with high accuracy, but are sensitive to object motion during the pattern projection and the speed of scanning process is relatively long. To reduce this sensitivity, single pattern techniques are developed to achieve a high speed scanning process, such as Composite Pattern (CP) and Modified Composite Pattern (MCP) technique. However, most of single pattern techniques have a significant banding artifact and sacrifice the accuracy. We focus on developing SLI techniques can achieve both high speed, high accuracy and have the tolerance to the relative motion. We first present a novel Two-Pattern Full Lateral Resolution (2PFLR) SLI method utilizing an MCP pattern for non-ambiguous phase followed by a single sinusoidal pattern for high accuracy. The surface phase modulates the single sinusoidal pattern which is demodulated using a Quadrature demodulation technique and then unwrapped by the MCP phase result. A single sinusoidal pattern reconstruction inherently has banding error. To effectively de-band the surface, we propose Projector Space De-banding algorithm (PSDb). We use projector space because the band error is aligned with the projector coordinates allowing more accurate estimation of the banding error. 2PFLR system only allows the relative motion within the FOV of the scanner, to extend the application of the SLI, we present the research on Relative Motion 3-D scanner which utilizes a single pattern technique. The pattern in RM3D system is designed based on MCP but has white space area to capture the surface texture, and a constellation correlation filter method is used to estimate the scanner's trajectory and then align the 3-D surface reconstructed by each frame to a point cloud of the whole object surface.

KEYWORDS: Structured Light Illumination, Computer Vision, 3-D Depth Measuring

Minghao Wang

Student's Signature

05/20/2015

Date

HYBRID SINGLE AND DUAL PATTERN STRUCTURED LIGHT ILLUMINATION

By

Minghao Wang

Laurence Hassebrook

Director of Dissertation

Caicheng Lu

Director of Graduate Studies

05/20/2015

Date

Acknowledgement

I would like to thank my academic advisor, Dr. Laurence Hassebrook, for the opportunity he gave me to pursue my degree in the field of 3D measuring, and all the guidance and help I've received from him all through these years. This thesis would be impossible without his extensive knowledge and innovative ideas in this field.

Special thanks should be accorded to Charles Casey for providing technical assistance. I would also like to thank Dr. Ruigang Yang, Dr. Kevin Donohue and Dr. Lau for serving as committee members, and for the insightful guidance I've received from them.

Last but not least, I would like to express my deepest gratitude to my parents, for the endless love and support I have always been with since I was born.

Table of Contents

Acknowledgement	III
List of Figures	VI
List of Tables	X
Chapter 1 Introduction and Historical Prospectus	1
1.1 Introduction	1
1.2 Historical Prospectus	3
1.3 Contribution	7
Chapter 2 Background	11
2.1 Structure Light Illumination	11
2.2 Classical Phase Measuring Profilometry (PMP) Method	13
2.3 Composite Pattern Technique	16
2.4 Microsoft Kinect 3-D Sensor	18
Chapter 3 Two-Pattern Full Lateral Resolution SLI Depth Measuring	20
3.1 Modified Composite Pattern (MCP)	20
3.2 2PFLR system setup	22
3.3 Non-ambiguous Pattern analysis	24
3.4 Quadrature Phase Pattern Analysis	34
3.5 Experiments Results	41
3.6 Summary	49
Chapter 4 Projector Space De-banding Algorithm	51
4.1 Introduction to Projector Space De-banding Algorithm	51
4.2 Mathematical Model of Projector Space De-banding Algorithm (PSDb)	53
4.3 Notations for Mathematical Model of De-Banding Algorithm	68

4.4 Experimental Results of PSDb Algorithm	71
4.5 Depth Modulation Transfer Function Performance Characterization for SLI system	74
4.6 Summary	79
Chapter 5 Relative Motion 3-D Scanner (RM3D)	81
5.1 Introduction to Relative Motion 3-D Scanning System	82
5.2 Relative Motion 3-D Pattern Analysis	86
5.3 3-D Surface Alignment Based on Estimated Transformation Matrix	103
5.4 Post Processing to Decrease the Accumulate Error	105
5.5 Experimental Results of 3-D Motion Scanner	106
5.6 Summary	108
Chapter 6 Conclusion and Future Research	110
6.1 Conclusion	110
6.2 Future Research	112
References	113
VITA	125

List of Figures

Figure 2.1 (Left) SLI geometry and (Right) stripe pattern on a sphere from Guan. et al [6]	11
Figure 2.2 Geometry of SLI to reconstruct 3D surface from [1]	12
Figure 2.3 An object projected with a sinusoidal pattern	13
Figure 2.4 (left) phase calculated by using $k=1$, and (right) phase calculated by using $k=16$	14
Figure 2.5 Composite Pattern technique [6]	16
Figure 2.6 Fourier Transform of Composite Pattern Image [6]	17
Figure 2.7 Block diagram of demodulate Composite Pattern [6]	18
Figure 2.8 A Picture of Kinect	18
Figure 2.9 Pattern from Kinect (Images are from flickr.com)	19
Figure 2.10 Captured reflected image from Kinect (left), Reconstructed Depth Map (right). (Images are from Wikipedia.org/wiki/Kinect)	19
Figure 3.1 A MCP pattern [10]	22
Figure 3.2 The two patterns used in Two-Pattern System	23
Figure 3.3 Two-Pattern System block diagram	24
Figure 3.4 Pre-Filter the image. Original Image (left), filtered image (right)	27
Figure 3.5 Snake Detection Process. Captured Image (left), detected snakes image (right)	28
Figure 3.6 Detected Snake Peaks image (negative image)	29
Figure 3.7 The snake before filtering (left), the snake after filtering (right)	30

Figure 3.8 Algorithm of Modified Composite Pattern processing	33
Figure 3.9 S_y image (left), linear interpolated phase image (right).....	34
Figure 3.10 Quadrature Phase Demodulator.....	36
Figure 3.11 Wrapped Phase Image	38
Figure 3.12 Object Bolder in black(left), masked out ROI image(right).....	38
Figure 3.13 One column signal of both phase images, Green in wrapped phase image, Blue is the baseline unwrapped phase image.....	39
Figure 3.14 Unwrapped phase and baseline phase	40
Figure 3.15 Unwrapped Quadrature Processing Phase Image.....	41
Figure 3.16 Two-Pattern Full Lateral Resolution Scanner Structure	42
Figure 3.17 Calibration Target [94]	43
Figure 3.18 Automatically detect the rings' centers (left), Phase Image with detected center in green (right).....	44
Figure 3.19 3D surface reconstructed only use MCP	45
Figure 3.20 Surface after Trend-filtering.....	46
Figure 3.21 3D surface with color texture	46
Figure 3.22 3D reconstruction by using Quadrature Phase Processing	47
Figure 3.23 QP reconstructed surface after trend filter.....	48
Figure 3.24 Colored 3D surface.....	49
Figure 4.1 Mapping a camera space image (left) to a projector space image (right).	54
Figure 4.2 Projector Space differential of the phase image with interpolation	56

Figure 4.3 Estimate Expectation of differential phase image	57
Figure 4.4 Estimated Expectation of Phase Value.....	58
Figure 4.5 Differential wrapped phase image in camera space	60
Figure 4.6 Branch Cuts image in projector space	62
Figure 4.7 Zoomed in branch cuts image.....	63
Figure 4.8 Image indicates the rows have branch cuts in projector space	64
Figure 4.9 Interpolated reference phase ramp.....	65
Figure 4.10 Estimated Banding Error	66
Figure 4.11 De-band Phase Image	67
Figure 4.12 A Baseline Flat Board to test the PSDb Algorithm	71
Figure 4.13 Reconstructed 3-D surface, front view (left) and rotated view (right)	72
Figure 4.14 Side view of the reconstructed 3-D surface of the flat board: Surface with Banding error (left), De-Band Result (Right)	72
Figure 4.15 Human Face Scan. Left One is with texture, right one is metallic 3D surface	73
Figure 4.16 Set of Sinusoidal Grid in the Experiment(left), scanner settings (right)	76
Figure 4.17 Sinusoidal Grid on the rotation stage, rotate the grid counter-clock-wisely from 90 degree (grid is vertical, top left), 60 degree (top right), 30 degree (bottom left) to 0 degree (grid is horizontal, bottom right).	77
Figure 4.18 DMTF for 90 degree to 0 degree	78
Figure 5.1 Relative Motion 3-D Scanning system, folded for portable	83
Figure 5.2 Relative Motion 3-D Scanner, Folded (left) and infolded for operation (right)	

.....	84
Figure 5.3 Optical Pattern for Relative Motion Scanning system	86
Figure 5.4 Original Image under test (left), result after PSR peak detection process (right)	88
Figure 5.5 Snake Matrix S_y for Relative Motion 3-D pattern	90
Figure 5.6 RM3D scan of test surface (left), PSR detection result(right).....	91
Figure 5.7 4-Connected Neighborhood.....	91
Figure 5.8 Snakes Peaks Detection result after snake growing	93
Figure 5.9 Partitions (white areas) for Constellation Correlation.....	95
Figure 5.10(a) Number 3 partition in current frame; (b) Number 3 Partition in previous frame; (c) Correlation results with shifting the peak to the middle of the image	96
Figure 5.11 Exponential MSD of 14 Partitions	98
Figure 5.12 Geometry of estimation of 3-D transformation matrix.....	102
Figure 5.13 Block Diagram for Snake Tracking and Constellation Correlation for Transformation Matrix Estimation algorithm.....	103
Figure 5.14 Recovered Phase Image for the nine snakes, depth information for only nine snakes	104
Figure 5.15 Point Cloud for 3-D reconstruction of all aligned patches, side view (left), frontal view (right).....	104
Figure 5.16 Experimental setup	107
Figure 5.17 Front view of scanned object surface (left), side view of scanned object (right)	108

List of Tables

Table 3-1 Phase Code (PC), Snake Code (SC) and Gray code (GC)	26
Table 3-2 The weights for matched filters used in our research.....	31
Table 4-1 Notations for Math Model of PSDB.....	68
Table 4-2 Comparison between Different De-Banding techniques	74
Table 4-3 Depth measurement performance characterization for MCP only	79
Table 4-4 Depth measurement performance characterization for 2PFLR	79

Chapter 1 Introduction and Historical Perspectus

In this chapter, we first introduce our research in section 1.1 which describes our motivation for doing the research in relative motion SLI area, and briefly introduces the methods used and techniques we developed. Section 1.2 is a historical prospectus of the related researches. Both passive and active computer vision techniques are reviewed, and the previous de-banding algorithms are also briefly described. Section 1.3 lists our contributions to the research areas of SLI and the details of our contribution are illustrated in the following chapters.

1.1 Introduction

Non-ambiguous depth accuracy and high speed data acquisition are the most important aspects of a 3-D capture technique. Ambiguous depth is a significant problem in many high speed approaches [1]. High accuracy ensures the quality of the 3D model reconstructed and many methods achieve high accuracy under certain environmental and scene. However, while most of the high accuracy techniques like Structured Light Illumination (SLI) produce very dense 3D points cloud, they require the object to be stationary for several seconds [11]-[13]. This limits SLI applications compared with some other methods such as Stereo Vision and Structure from Motion which allow the relative motion between the object and the scanner. Our group's research focuses on solving the problems in SLI method to allow for the relative motion between the target object or scene and the scanning system. Given the "relative motion" problem, we address two research aspects of that problem: (1) Relative Motion within Field of View (FOV) of a scan and (2) Relative Motion across a scene larger than the FOV.

The first direction of our research is a SLI scanner algorithm that allows the relative motion within the Field of View (FOV) of the Scanner. To achieve this goal, we need to address the scan time issue, which is that most of SLI methods require projecting a series of patterns temporally onto an object in order to capture its 3D surface. Our group inspired by the composite filter theory and communication theory has developed methods

to spatially modulate several patterns into one pattern. In this way the 3D model can be reconstructed by using a single pattern. This single pattern system gives the SLI technique ability to capture the 3D motion of the object limited only by the capture speed of the camera. However, the spatial modulation decreases the spatial resolution of the reconstruction results. Low spatial resolution makes the SLI technique less appealing. So a trade-off decision is made between the spatial resolution and the number of the patterns used (less patterns means less sensitivity to 3D motion). Previous research on fast PMP 3D scanning requires at least 3 patterns whereas the spatial modulation method only requires 1 pattern [57]-[61]. Based on previous research we have developed a two-pattern method which achieves both non-ambiguous and high spatial resolution. The two-pattern method is a synergistic combination of a non-ambiguous pattern and a sinusoidal pattern. The first pattern is a Modified Composite Pattern (MCP) which is a non-ambiguous pattern but the 3D result has low lateral resolution along the phase direction. The second pattern is a sinusoidal pattern with same spatial frequency with MCP, and this 2nd pattern is ambiguous but with quadrature demodulation achieves high spatial resolution. In another level of synergism the ambiguous pattern is used to locate the non-ambiguous pattern features. So we do not just use a non-ambiguous pattern to unwrap the second, but we make use of an almost symbiotic relationship between the two patterns.

The second direction of our research is to study a SLI method that allows the relative motion beyond the Field of View of the scanner. This requires the scanner to be portable and not tethered to a computer, analogous to a commercial camera which captures 2D imagery. We refer to this as a “3D” camera which outputs the 3D model of the scene instead of a photograph. Our study of a 3D motion scanner is a good application of this idea. Inspired by the idea of finding correspondence between two parallax images in Stereo Vision, we designed a pattern which utilizes both the spatial modulation method of SLI and the correspondence matching method to reconstruct the 3D of a scanned surface. Unlike the classical SLI pattern which is just a series of sinusoidal pattern or the MCP which modulated the pattern, this motion scanning pattern only has a few lines of snakes that cover just part of the FOV and rest of the FOV is left open for correspondence matching. With three snakes groups we achieve the accurate 3D depth information. And

with the blank area in the pattern, we capture the texture of the surface which offers us the information for correspondence between the images captured by the scanner since there are a large overlapping areas. Many algorithms have been developed to reconstruct 3-D shape using images with overlapping area [65]-[68]. By utilizing a constellation correlation filter which dramatically increases the efficiency and accuracy of the correlation. We then match the sparse 3D points cloud and merge them into one dense 3D surface. By moving the scanner across the scene, we achieve the goal to scan a large object by using a portable hand held scanner.

1.2 Historical Prospectus

Over the decades 3D optical metrology industry has required higher speed and higher accuracy 3D surface measurement and reconstruction technology for the application in many fields [19]. These include process control and yield management in manufacturing, surveillance system, privacy protection and security, and medical imaging area [16]. Numerous 3D reconstruction and measurement methods have been developed in Computer Vision area such as Stereo Vision, Time of Flight (ToF), Structure from Motion (SfM), Unstructured Lumingraph, and Structure Light Illumination (SLI). All of the depth estimation methods can be further divided into two categories: Passive method and Active Method [100]. In this section, we briefly describe the methods which are related to our research historically.

1.2.1 Passive Methods

Passive methods utilize the images taken from one or two cameras without interference with the object. That is, only cameras are used in these methods and most of these techniques are developed based on the multi-view geometry as illustrated in [101]. Based on the principle of multi-view triangulation, a point's 3D position can be reconstructed by intersection the lines of sight of the corresponding pixels in multiple images [101]. Two of the most important methods, Structure from Motion and Stereo Vision, belong to this class.

Stereo Vision. The idea of the Stereo Vision has evolved from mimicking the human

eyes. In a classical Stereo Vision method, the configurations of the camera are known by using the calibration method. And the correspondence of the pixels in multi-view images is computed to reconstruct a dense 3D surface [33]. However, the accuracy of Stereo Vision highly depends on the image-to-image correspondence which is complicated and usually fails for scenes with little texture or non-Lambertian [100]. Due to the computation complexity, dynamic programming framework is often necessary [40].

Structure from Motion. Unlike the Stereo Vision techniques, SfM does not require known configurations for the camera [99]. And given an image sequence with estimated correspondences of the feature points, the SfM is able to reconstruct both the camera trajectory and the 3D surface of the object. In [101], the pipe line of SfM is described. However, the correspondences across the image sequence are established for a few image feature points, so the reconstruction of the SfM usually has very sparse 3D points.

1.2.2 Active Methods

Active methods actively project the radiance or patterns onto the object and then the depth is estimated based on the captured reflected images. Among these methods, SLI technology provides the highest accuracy in reconstruction 3D surface [90]-[93]. The idea of SLI is to project a pre-designed pattern, which is usually a stripe pattern or grid pattern, onto an object [17] [32]. Then, a camera captures the reflected pattern which is laterally distorted by the 3D surface, and based on the triangulation geometry of the 3D scanning system, the 3D depth information is calculated [7].

Multi-pattern SLI. Classical high accuracy SLI technology uses multi-pattern projection technique. It is widely researched to achieve a high accuracy 3D reconstruction and a high quality phase must to be recovered [35-39] [47]. So to reduce the phase error is of great significance, which is the reason for requiring projection of multiple sinusoidal patterns onto the object as in classical SLI methods. High reliability in identification of light patterns with minimum assumptions about the nature of the surface are achieved by time multiplexing, i.e. by sequentially projecting several patterns on the object. Kak, et al. proposed the gray level encoding time multiplexing pattern which is a binary-encoded SLI in 1980's [1]. Later on, Kak, et al. proposed assigning a binary code word to each

projected stripe of a series of multiple stripe projections, where associated code word determines the presence of any given stripe [2]. This encoding method did achieve the non-ambiguous range sensing [14] [15] [44] [91] [93]. However it is limited by the device's lateral resolution, because the resolution is dependent on each identified stripes.

Phase Measuring Profilometry (PMP). Another widely used time multiplexing technique is known as Phase Measuring Profilometry (PMP) [3] [25], which uses a series of sinusoidal patterns across the surface of the object. In this way the patterns modulate each pixel with a unique phase value. However, the single frequency PMP technique's accuracy and depth ambiguity is dependent on the frequency of the sinusoidal pattern. That is, a high frequency PMP technique maintains a high depth resolution but led to depth ambiguity, where as a low frequency results in noisy non-ambiguity reconstructed surface. To avoid the difficulties caused by single frequency, a multi-frequency PMP has been adopted in many applications [23]. Multi-frequency PMP techniques use low frequency for the non-ambiguity and high frequency pattern for the high depth resolution, and achieve a better result than the single frequency PMP. But the tradeoff of the multi-pattern PMP is it requires the object to be remain motionless for all the patterns which leads to a long scanning process [61]. To improve the performance, high speed projection and capture systems have been developed. Liu et al. proposed a high speed SLI PMP system which achieves 120 frames per second acquisition, processing, and display 3D point cloud [24], however their system only utilized 3 patterns which decreased the accuracy of the 3D reconstruction result. In addition to this, low numbers of patterns are susceptible to banding artifacts.

Color-multiplexing SLI. To reach the goal of high speed that allows the relative motion between scanner and object [90], single pattern Structure Light Illumination technique have been developed by using different spatial modulation methods or pattern design [5] [11]. A single pattern SLI approach is to use Color-multiplexing. Color-multiplexing combines the individual patterns of multi-pattern SLI techniques into several color channels, then processing them by decoding each channel's image. For instance, one can easily combine three patterns from PMP technique into a color image's R, G, and B channel. Then after capture of the color image, those three patterns are acquired from the

3 channels. However, this technique's accuracy is limited by the channels that can be used and the color of the scanned object [17], which can cause both ambiguous, noisy and low depth resolution.

Composite Pattern. The Composite Pattern technique was developed by Guan, et al. [6] [94] modulates patterns from a time multiplexed method, such as the PMP method, into one single pattern by using several known spatial carrier frequencies [63]. This idea comes from communication theory and signal modulation [67] [81], but unlike the Color-multiplexing technique which combines the PMP patterns in the three color channels, all the PMP patterns in the Composite Pattern technique are the same "color" spectrum. So, by using demodulating procedure, all the PMP patterns are separated and processed for depth. CP method based SLI system achieves a very high speed 3D data acquisition with satisfactory accuracy [62]-[64]. However, the lateral resolution of CP is low, and when this technique is applied to human scanning [88], the Human skin's Spatial Modulation Transfer Function's (SMTF) attenuation of spatial frequencies components introduces errors in depth measurement [83] [84].

Modified Composite Pattern. To solve the SMTF problems of Composite Pattern, instead of modulating PMP patterns, Pratibha [9] utilized binary Gray Code patterns in the modulation procedure. Casey, et al. improved lateral resolution of the gray code Composite Pattern by introducing a new pattern named Modified Composite Pattern (MCP) [10] [55] [95]. MCP is a pattern encoded along the orthogonal axis of the image, and each encoded stripes are encoded following the Gray Code sequence introduced by Pratibha. The biggest achievements of MCP technique are that it not only maintains the advantage of Composite Pattern but is also insensitive to skin SMTF, and has increased lateral resolution [8] [95]-[98].

Pseudorandom Noise Pattern SLI. Instead of projecting the sinusoidal wave patterns onto the object, pseudorandom noise pattern SLI techniques utilize the generated pseudorandom noise as the projection pattern [102]. By using the similar correspondence estimating techniques utilized in Stereo Vision, the correspondence of each pixel is established between the captured reflected image with a reference image. The advantage

of this technique is by projecting the random noise to the object surface, the features points for correspondence are actively “projected” to object surface and do not have banding artifacts. The noise is utilized to establish a dense correspondence estimation map and then used to estimate the depth. However, in order to efficiently process the reflected image, dynamic programming is required as illustrated in [102], which increases the complexity of the algorithm dramatically.

1.2.3 De-banding Algorithm and Gamma Distortion Correction for SLI

As mentioned before, while the single pattern techniques make high speed 3D scanning possible, the banding error in the phase is a significant problem. For reducing banding error, the state-of-art research direction is to calibrate the nonlinear response of the system and then compensate for the error actively or passively. The active method modifies the projected pattern such as the non-sinusoidal fringe model proposed by Wang, and Zhu, et al. [25], in this way the error is suppressed by the pattern itself. The passive method is to compensate the phase banding error using post-processing method after capturing the image [26] [27]. Most of the passive methods focus on the gamma calibration and defocusing algorithms.

1.3 Contribution

Our research contribution for high speed relative motion SLI systems include: 1) Improved Post-processing technique for MCP; 2) Two Pattern Full Lateral Resolution techniques (2PFLR) with quadrature post-processing; 3) The Projector Space De-banding Algorithm (PSDb); 4) Performance Characterization for SLI system using Depth Modulation Transfer Function (DMTF); 5) Relative Motion 3D scanning system for relative motion beyond FOV.

Our first contribution is the improved processing technique for MCP. Based on Casey’s work on MCP, we developed an improved processing algorithm by utilizing the Matched Filter Bank. The original processing technique proposed by Casey uses the 2-D Fourier Transform to detect and demodulate the snakes, but the results in the frequency space have significant noise which reduces the demodulation performance. And Casey’s

detection algorithm is sensitive to the surface discontinuity. Our processing algorithm reduces these problems by using 1-D Matched Filter Bank.

To solve the problem of detection the modulated snakes in MCP and increase the resolution and accuracy of the MCP technique, the 2PFLR system is developed. This 2PFLR is our second contribution. By adding another high frequency sinusoidal pattern, the problem of detecting the modulated snakes in MCP is reduced by identifying the snakes in the second sinusoidal pattern which improves the snake detection with high SNR. Also, we introduce a novel Quadrature Phase processing technique which processes the sinusoidal pattern efficiently and effectively to get the full lateral resolution wrapped phase image. This 2PFLR system is a significant contribution to SLI research. There is a trade-off between the high speed and high accuracy of the SLI system. To achieve high speed, single pattern SLI techniques are good solutions. However, single pattern techniques sacrifice the accuracy of the system. Instead of focusing on improving the performance of the single pattern technique such as CP and MCP, we develop this 2PFLR system. The first MCP is used to reconstruct the coarse non-ambiguous surface and the second sinusoidal pattern is used to get the high resolution but ambiguous depth. We combine these two results together to achieve both non-ambiguous and high resolution at the same time. Although we added another pattern into the single pattern MCP system, this system is still considered as a high speed acquisition algorithm because it allows the relative motion between the scanner and the object during the scanning process, as long as the motion of the object between the projection the first and second pattern is less than half of a spatial wavelength along the phase direction. Our contribution in 2PFLR system opens a new direction of the research for high speed and high accuracy SLI depth measuring system, i.e. we can combine the advantage of the single pattern technique with the multi-pattern technique.

Our third contribution is the Projector Space De-banding algorithm (PSDb). Due to the gamma distortion of the projected sinusoidal pattern and the quantization error in the hardware, the 3-D surface reconstructed by SLI techniques usually has significant banding distortion. This banding distortion corrupts the final results and decreases the accuracy of the depth measuring system. Unlike the widely used Gamma model for

compensating the banding distortion, our PSDb does not need to pre-calibrate the banding distortion for each system and can be actively applied to any 3-D model reconstructed by SLI technique. We assume the banding distortion is a 1-D signal along the phase direction, and we estimate the banding distortion in Projector space then correct it in the camera space. The reason to map the phase image to projector space is the phase value in the camera space is proportional to the row index in the projector space, so the curved snakes in camera space are straight in projector space. So, each column (along the phase direction) is a stochastic signal associated with banding distortion. We apply the stochastic signal processing techniques to estimate the 1-D banding distortion and then suppress it in camera space.

The next contribution is the performance characterization of the SLI system. Although SLI is a widely research topic since 1990, there is not a standard performance characterization for any SLI systems. Inspired by the Modulation Transfer Function, we introduce a model of Depth Modulation Transfer Function (DMTF) performance characterization for SLI depth measuring system. By using several sinusoidal grids with different spatial frequencies and a rotation stage, we can characterize performance for any SLI systems. By using this performance characterization system, both the accuracy and the precision of the SLI system can be measured. The accuracy is measured by the reconstructed 3-D sinusoidal surface's peak to peak value, and the precision of the system is measured by the DMTF value as a function of spatial depth frequencies. Moreover, the rotation stage gives the ability to measure the performance of the SLI system for directions.

The last contribution is Relative Motion 3-D (RM3D) scanning system. This system allows the motion of the object beyond the FOV of the scanner. We design a new single pattern technique especially for the RM3D system, and this pattern is designed based on MCP. The non-ambiguous single pattern technique used in RM3D makes the system tolerant to the motion of the object or the scanner, however, only this technique alone cannot reconstruct a whole 3-D surface. Since the 3-D surface reconstructed by the SLI is relative to the scanner, we do not have the absolute 3-D coordinates for the 3-D surface. So we apply and adapt a Correlation Constellation Filter method to align the images

captured by the camera and use this method to estimate the camera position for each frame in the image sequence. Compared with other camera tracking techniques in the Computer Vision area, our method is presently limited to in-plane rotation and x , y translation. However, the contribution to RM3D gives a clear direction for achieving additional affine distortion including out-plane rotation, scale and depth translation.

Chapter 2 Background

The background related to our research is introduced briefly. Since our research mainly focuses on SLI technology, we first describe the fundamental idea, system and process of SLI method in section 2.1. Phase Measuring Profilometry method is a classical SLI technique that offers the one of the best 3D reconstruction results which is non-ambiguous and high accuracy. Also many other SLI techniques are inspired by classical PMP method, so we introduced PMP method in section 2.2. In section 2.3, Composite Pattern (CP) method is introduced as background for our research on single and double SLI depth measuring methods.

2.1 Structure Light Illumination

Structured Light Illumination (SLI) is a well-known 3D measuring method which is used in acquiring the depth information of a surface by measuring the deformation in the light pattern projected onto the surface. Compared with many other 3D reconstruction methods in computer vision area, SLI offers one of most accurate 3D depth measuring results which is used for many application including finger print scanning, industrial measurement, human computer interface and special effects.

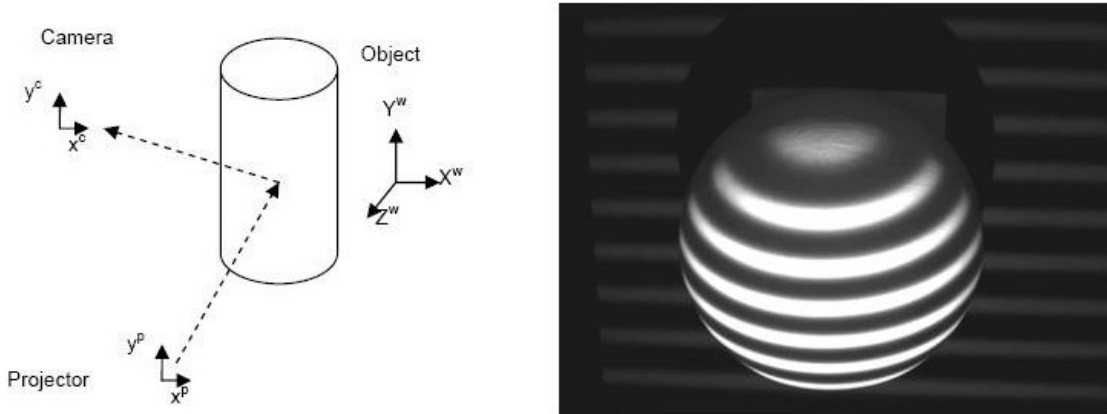


Figure 2.1 (Left) SLI geometry and (Right) stripe pattern on a sphere from Guan. et al [6]

Fig. 2.1 shows the classical SLI technology. An SLI system always consists of two parts: one is a camera and the other part is a projector, and the geometry of the system is shown

in Fig. 2.1 left to make sure the camera and projector are setup at relative angle for triangulation. And Fig. 2.1 right shows a classical sinusoidal pattern that is projected onto an object showing the lateral distortion caused by depth variation of a sphere.

Since the sinusoidal pattern is curved by the object surface, we reconstruct the 3D depth of the surface by calculating the phase shift of the pattern. As shown in Fig. 2.2, we need to calculate the depth of surface at point A by using SLI. The depth at A is h to the reference plane. By using simple geometry of similar triangles, the depth at point A is calculated:

$$h = \frac{BC \cdot L}{d + BC} \quad (2.1)$$

L and d in the system are constant parameters which are determined by the calibration procedure. And the BC is determined by the phase difference of the sinusoidal pattern:

$$BC = \beta(\varphi_C - \varphi_B) \quad (2.2)$$

Where β is also a constant parameter which is calibrated in the calibration process, and φ_C and φ_B are the unwrapped phase value at point C and point B.

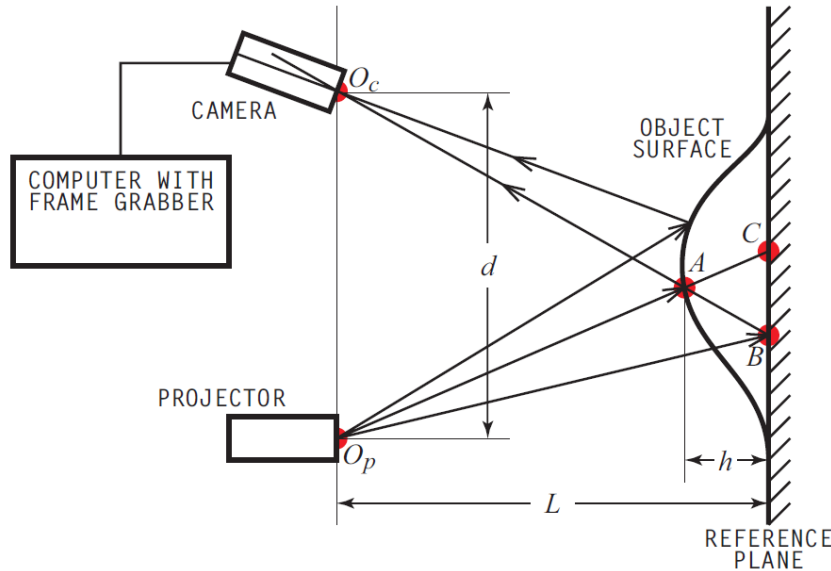


Figure 2.2 Geometry of SLI to reconstruct 3D surface from [1]

Because the depth value is determined by the unwrapped value calculated at point B and point C, so the accuracy of the depth value depends on the accuracy of the phase value and the unwrapping algorithm.

2.2 Classical Phase Measuring Profilometry (PMP) Method

Phase Measuring Profilometry is a well know and widely used method in SLI research, since it offers the highly accurate 3D reconstruction by using multiple projected patterns. The accuracy of the 3D reconstruction is directly related to the number of patterns and the pattern spatial frequency. The sampling rate is equal to N times the number of the pixels per frame of a high resolution image, where N is the number of phase steps used in an N-step PMP algorithm [3].

When using PMP technique, we still use the classical SLI system setup as shown in Fig. 2.2, and the patterns that needed to be projected are a series of sinusoidal patterns with different spatial frequency and then phase shift the patterns N steps. Fig. 2.3 shows an object which is projected with one of the sinusoidal pattern and captured with the camera.

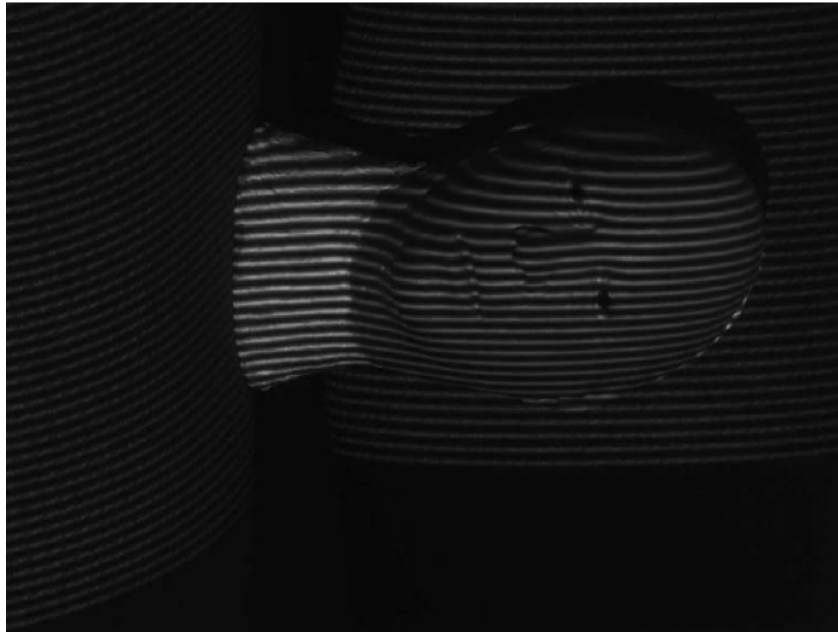


Figure 2.3 An object projected with a sinusoidal pattern

The basic idea of PMP is to use those captured image sequence to estimate the phase

shifting due to the depth distortion. For the image shown in Fig. 2.3, it can be expressed as

$$I_k(x, y) = A(x, y) + B(x, y)\cos[\varphi_k(x, y)] \quad (2.3)$$

where $A(x, y)$ is the ambient light intensity, and $B(x, y)/A(x, y)$ is the fringe contrast. The phase function $\varphi(x, y)$ contains the information for the 3D depth value at (x, y) point as mentioned before. For the general N-shift with k_c frequency PMP method, to calculate phase function, we use the following equation:

$$\varphi_k(x, y) = \arctan[(\sum_{n=1}^N I_{k_c, n}(x, y)\sin(2\pi n/N))/(\sum_{n=1}^N I_{k_c, n}(x, y)\cos(2\pi n/N))] \quad (2.4)$$

where $I_{k_c, n}(x, y)$ is the captured image with k spatial frequency pattern projected on the object, and N is the total number of phase shifted patterns. Note that if the spatial frequency k_c is greater than 1, then the phase calculated by using the equation is wrapped into the range of its principal values as shown in Fig. 2.4 right.

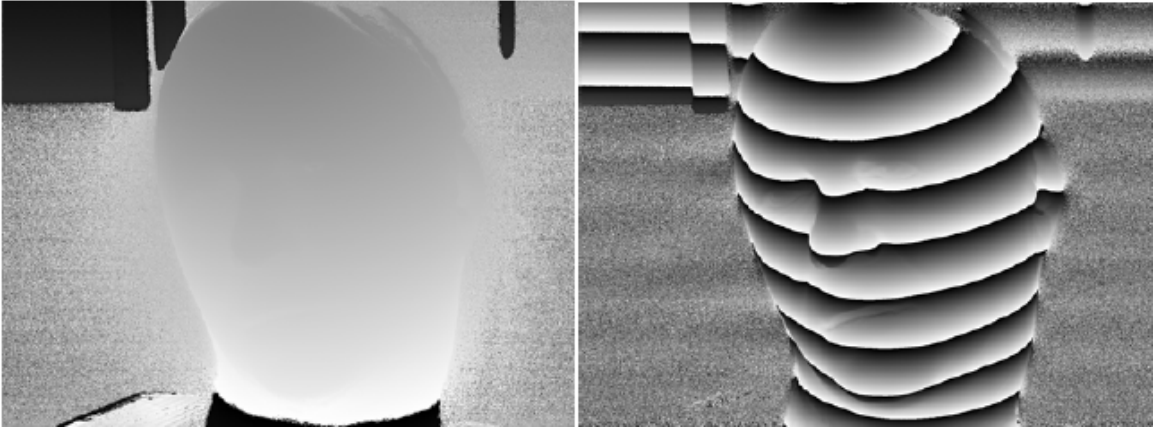


Figure 2.4 (left) phase calculated by using $k=1$, and (right) phase calculated by using $k=16$

Fig. 2.4 shows the two different phase images calculated based on two different spatial frequencies. Left phase image is calculated by N phase shifting of a sinusoidal pattern with spatial frequency equals to 1, and right phase image is calculated by a sinusoidal pattern with spatial frequency of $k_c=16$. The difference between phase images calculated by different spatial frequencies is the low spatial frequency phase image (Fig. 2.4 left) provides the phase with non-ambiguity but high noise, whereas the high frequency phase

image provides low noise but ambiguous phase. we can obtain both non-ambiguity and low noise by unwrapping the high spatial frequency phase image with the low spatial frequency phase image. In this way, a high accuracy non-ambiguity phase image will be acquired.

The fundamental idea of unwrapping algorithm in PMP method is to utilize $k=1$ phase image as a reference to unwrap the other phase images. We first need to normalize the high spatial frequency image by dividing the phase value by the pattern spatial frequency k , for example, for the phase image shown in Fig. 2.4 (right), we need to divide it by 16 in order to normalize it. Then the second step is to obtain the integer number of the phase unwrapping cycles that are at or below the desired value such that

$$\lambda(x, y) = \text{floor}(k\varphi_1(x, y) - \varphi_{k_c}(x, y)/2\pi) \quad (2.5)$$

where k_c is the spatial frequency of the phase image that need to be unwrapped, and φ_1 is the reference phase.

Then, the difference between the reference phase or baseline phase and the unwrapping phase is calculated as

$$r(x, y) = (k\varphi_1(x, y) - \varphi_{k_c}(x, y) - 2\pi\lambda(x, y))/2\pi \quad (2.6)$$

The final adjustment of the unwrapping cycles are done by using the remainder $r(x, y)$,

$$\lambda_u(x, y) = \begin{cases} \lambda(x, y) + 1, & \text{for } r(x, y) > 0.5 \\ \lambda(x, y) - 1, & \text{for } r(x, y) < -0.5 \end{cases} \quad (2.7)$$

After calculating the phase unwrapping cycles, we obtain the unwrapped phase by

$$\varphi_{k_c, \text{unwrapped}}(x, y) = (2\pi\lambda_u(x, y) + \varphi_k(x, y)) \quad (2.8)$$

After we unwrap the high spatial frequency phase, we get a high accuracy phase map without wrapping which we utilize it direction to get the depth by using Eq. (2.1) and Eq. (2.2). And also we note that the accuracy of the depth directly related to the accuracy of the phase image.

2.3 Composite Pattern Technique

Composite Pattern method is proposed by Guan, et al. And the details about this technique are described in [6]. The purpose of the technique is to create a single pattern SLI technique which reconstructs non-ambiguous 3D surface and can be used in real-time high speed 3D data acquisition system. The basic idea of the Composite Pattern (CP) is to use the modulation theory to modulate the PMP patterns into one pattern, the details of the theory and similar ideas are described in [75]-[82], and then demodulate the captured reflected image into the separate distorted pattern.

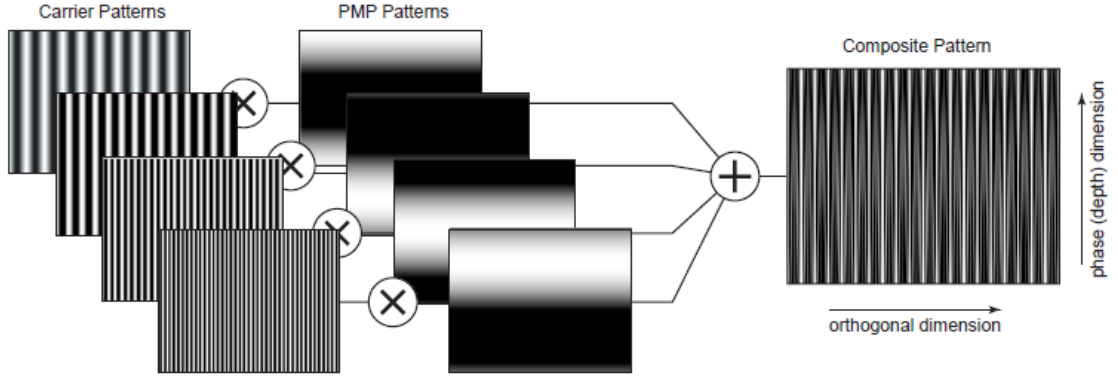


Figure 2.5 Composite Pattern technique [6]

Fig. 2.5 shows the pipeline of creating a Composite Pattern by modulating four PMP patterns. We have four carrier patterns which are sinusoidal patterns in orthogonal direction, each with a different spatial frequency. Each PMP pattern is multiply by a carrier pattern and they are added together to yield a single Composite Pattern.

The PMP patterns in Fig. 2.5 are expressed as

$$I_n^p = c + \cos(2\pi f_\phi y^p - 2\pi n/N) \quad (2.10)$$

where c is a constant that offset the pattern's intensity to above 0. Then the Amplitude modulation is expressed as

$$I^p = A^p + B^p \sum_{n=1}^N I_n^p \cos(2\pi f_n^p x^p) \quad (2.11)$$

where f_n^p is the n th carrier frequency, and A^p , B^p are calculated as:

$$A^p = I_{min} - B^p \cdot \min\{\sum_{n=1}^N I_n^p \cos(2\pi f_n^p x^p)\} \quad (2.12)$$

$$B^p = \frac{(I_{max} - I_{min})}{(\max\{\sum_{n=1}^N I_n^p \cos(2\pi f_n^p x^p)\} - \min\{\sum_{n=1}^N I_n^p \cos(2\pi f_n^p x^p)\})} \quad (2.13)$$

where I_{max} and I_{min} are maximum and minimum pixel intensity in the pattern image. The equations of A^p and B^p ensure the intensity range of the composite pattern falls into the interval $[I_{min}, I_{max}]$.

After capturing the reflected image of composite pattern, we need to demodulate it, so the PMP patterns are retrieved and are used to reconstruct the 3D surface by using classical PMP techniques. To demodulate the Composite Pattern image, band pass filters are used to identify the response of each carrier frequency and then demodulate each PMP pattern. As shown in Fig. 2.6, the Fourier transform of the Composite Pattern image has four isolated peaks which represent four modulated patterns, and then four band pass filters are applied to isolate each of the modulated patterns.

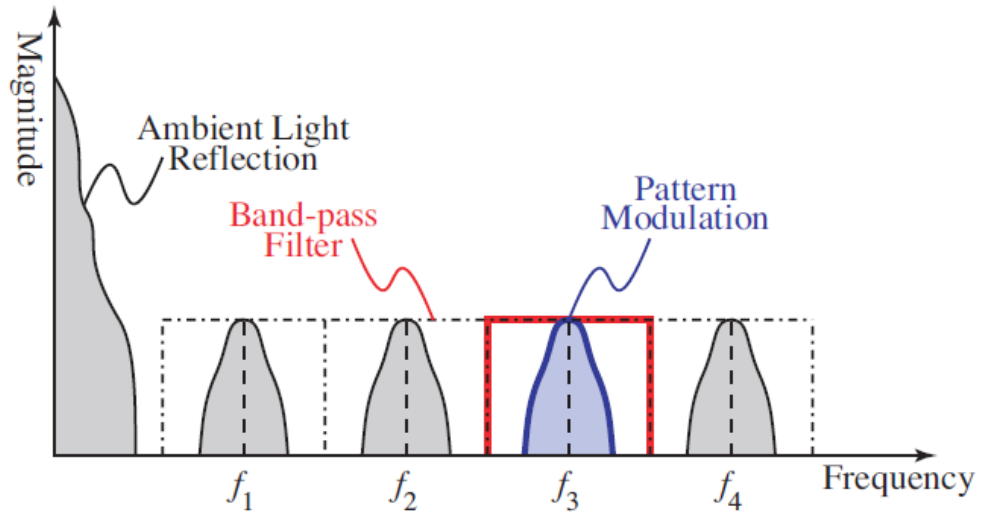


Figure 2.6 Fourier Transform of Composite Pattern Image [6]

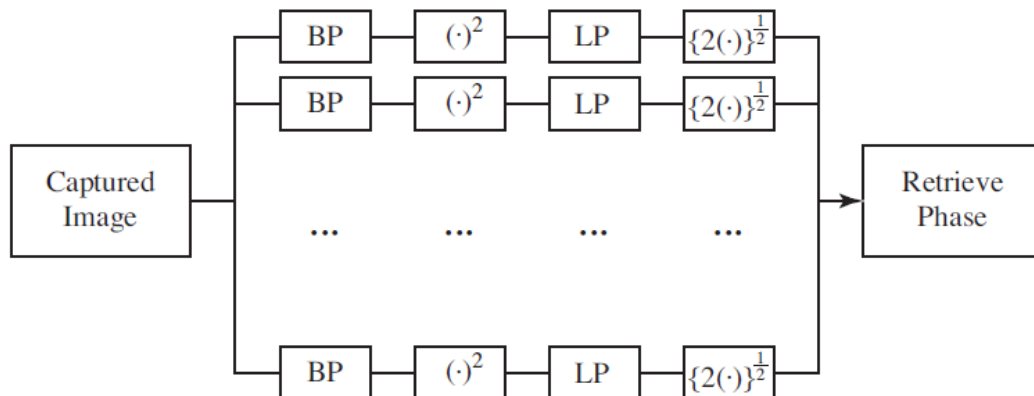


Figure 2.7 Block diagram of demodulate Composite Pattern [6]

Fig. 2.7 shows the process of Composite Pattern demodulation. After passing through the band pass filters, a classical AM demodulating method is utilized to extract the PMP patterns.

2.4 Microsoft Kinect 3-D Sensor

Microsoft introduced its first generation 3-D sensor Kinect for gaming platform XBOX360 in 2010, and from that time on, Kinect became a widely used 3-D sensor especially for 3-D motion sensing.



Figure 2.8 A Picture of Kinect

Fig. 2.8 shows a picture of the Kinect. Kinect consists of 3 components for depth sensing: a RGB camera for texture, a near infrared camera and a near infrared projector. So the technology utilized in the first generation of Kinect is the infrared SLI. However, unlike projecting the sinusoidal wave in our research, Kinect's projector omits the pseudorandom noise pattern as shown in Fig. 2.9.

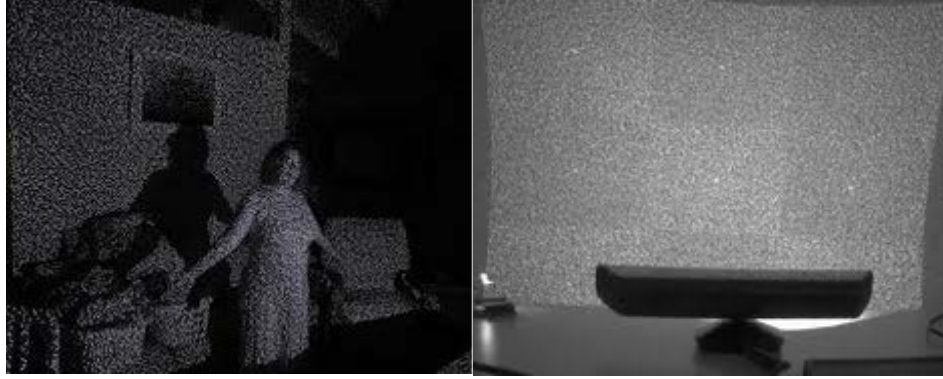


Figure 2.9 Pattern from Kinect (Images are from flickr.com)

As briefly introduced in Chapter 1, pseudorandom noise pattern is a single pattern SLI technique which is able to estimate the depth by using 1 captured image. In this way, Kinect has the ability to sense the 3-D motion in real time. A depth map reconstructed from Kinect is shown in Fig. 2.10.

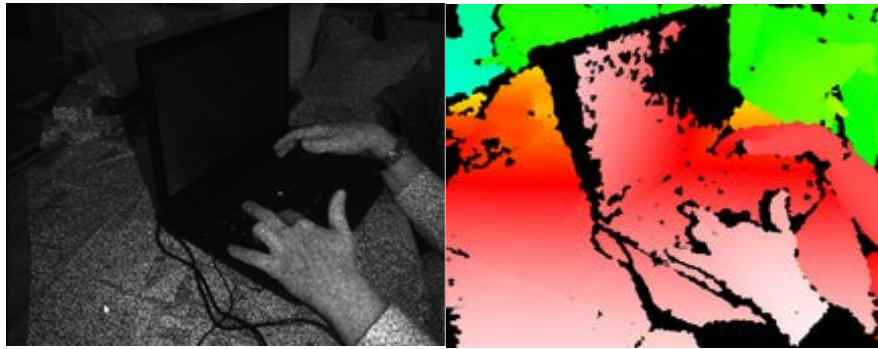


Figure 2.10 Captured reflected image from Kinect (left), Reconstructed Depth Map (right). (Images are from Wikipedia.org/wiki/Kinect)

Compared with other single pattern technologies such as CP and MCP, the biggest advantage of pseudorandom noise pattern is the reconstructed 3-D surface does not have a significant banding artifact which is caused by gamma distortion of the projected sinusoidal pattern. And by using a well-designed dynamic programming framework, the accuracy of the depth map can be improved. However, the limitation of this technique is the resolution of reconstructed surface is not as high as CP or MCP .

Chapter 3 Two-Pattern Full Lateral Resolution SLI Depth Measuring

The chapter describes our first research direction which focuses on the study of a high-speed Structure Light Illumination system that allows the relative motion between the 3D scanner and the object within the Field of View of the scanner [28].

Part of the Two-Pattern technique is based on a single pattern SLI method that proposed by Casey et al. [10], named the Modified Composite Pattern (MCP) method. In section 3.1, we briefly describe the MCP technique and its restriction as a single pattern SLI technique. By adding a new high frequency sinusoidal pattern as the second pattern, we introduce a novel two-pattern SLI system [28]. In section 3.2, we introduce the overall system design and the pattern design, and briefly describe the system setup and the 3D reconstruction process. The two patterns have individual functions as well as interactive processing between them. The primary function of the first pattern is to allow reconstruction of the 3D surface without ambiguity, so in section 3.3, we describe non-ambiguous pattern analysis method and processing technique. The second pattern is a high frequency sinusoidal pattern for full lateral resolution 3D reconstruction. We introduce a novel quadrature phase processing technique to process the second pattern. In section 3.4, the quadrature phase pattern analysis method is presented. In section 3.5, the experiments results are presented and a Depth Matched Transfer Function (DMTF) performance characterization method is described. Section 3.6 is the summary of the two-pattern full lateral resolution SLI depth measuring method.

3.1 Modified Composite Pattern (MCP)

As mentioned in the Background Chapter 2, the Composite Pattern (CP) technique is a single pattern technique which is proposed to create a high-speed 3D depth measuring system. However, a problem with using CP became apparent which was the skin spatial frequency response was not flat and therefore corrupted the weighting of the individual patterns [10]. In this case, the 3-D reconstruction result is highly banded or distorted.

MCP was proposed by Casey, et al. [10] based on the fundamental idea of Composite Pattern. To solve the problem with the skin spatial response; a binary encoding method

was introduced where a binary Gray code structured light pattern allows 3D reconstruction insensitive to variation in spatial frequency. The uniquely encoded binary value always corresponds to a point in the projector space, which means the depth of this point can be calculate. The values collected during the sequence create a binary number identified as the point's Gray code value. The Gray code form of CP, and especially MCP SLI allows a single frame equivalent of these multiple projections.

In a MCP which uses Gray Code encoding, a single modulated "snake" will be associated with a specific Gray code value, where snake means the stripe in the SLI pattern. This novel design places an un-modulated snake between every two Gray code snakes. Using Composite Pattern analysis and processing techniques each modulated snake is able to be identified, but in addition to this, each un-modulated snake can be used for 3D reconstruction as well, since any un-modulated snake located between two sequential Gray code snakes is uniquely identifiable. The presence of un-modulated stripes effectively doubles the amount of useful information in a Modified Composite Pattern. A typical MCP is shown in Fig. 3.1.

The mathematical expression of a MCP will be illustrated in next section. For the MCP in Fig. 3.1, we use four different frequencies to do the horizontal modulation. The spatial frequencies are 40, 80, 120 and 160 cycles per FOV. Each of the horizontally modulated snakes are demodulated after captured, and the demodulated snake gives us the information of the phase value of the sinusoidal pattern in the phase direction, since the phase value for each modulated snake is calibrated during the calibration procedure. Also, the un-modulated snakes which are located between the modulated snakes are identified after the modulated snakes are demodulated. The un-modulated snakes' phase values are also identified from calibration. After the phase value is identified for each snake (modulated or un-modulated), we form a phase image which has the phase value for each of the snakes, then linear interpolation for each column is utilized to calculate the phase value between the two adjacent snakes. As a result, a phase image is obtained, and is able to unwrap the phase obtained from the second pattern.

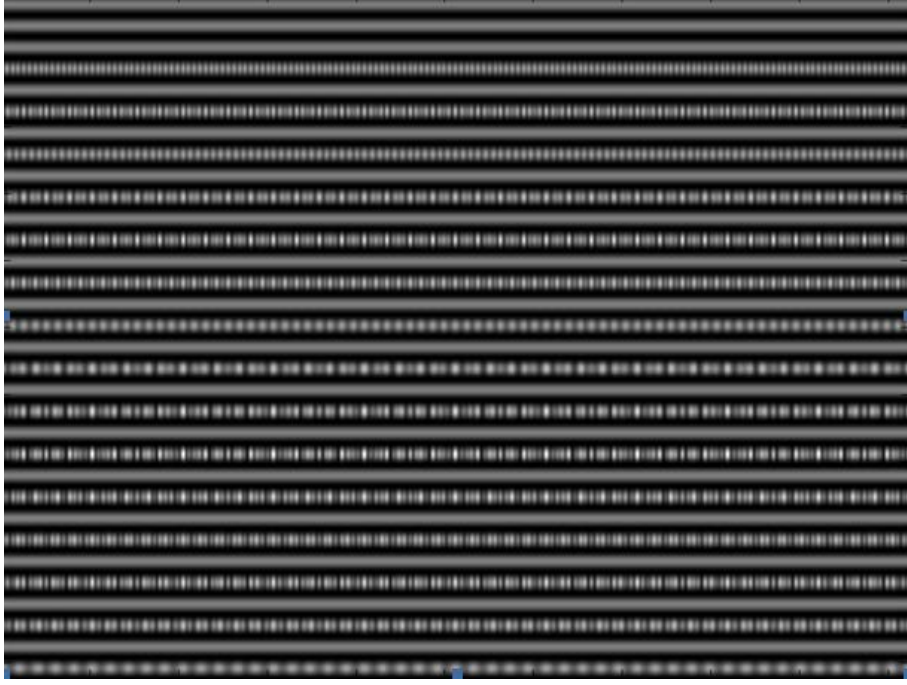


Figure 3.1 A MCP pattern [10]

3.2 2PFLR system setup

This section describes the Two-Pattern full lateral resolution depth measuring system setup. As stated in the introduction Chapter 1, the Two-Pattern system is composed of a Modified Composite Pattern and a high frequency sinusoidal pattern (sinusoidal wave variation along the phase direction) and are sequentially projected onto the object surface. Since only two patterns are used, the projection time is intensively reduced compared with classical PMP method which needs to project at least 3 patterns and phase shifting N steps. In this way, like the single pattern technique, we allow the relative motion between the scanner and object within the Field of View of the scanner. And the speed of relative motion depends on the projection rate. Furthermore, since the final phase image is the unwrapped 2nd pattern phase, the Two-Pattern technique is tolerant of motion between the 2 pattern projection as long as the motion distortion does not exceed the spatial wavelength of the 2nd pattern. In the Two-Pattern system, the MCP pattern is used for non-ambiguity and the high frequency sinusoidal wave pattern is used to achieve full

lateral resolution in depth.

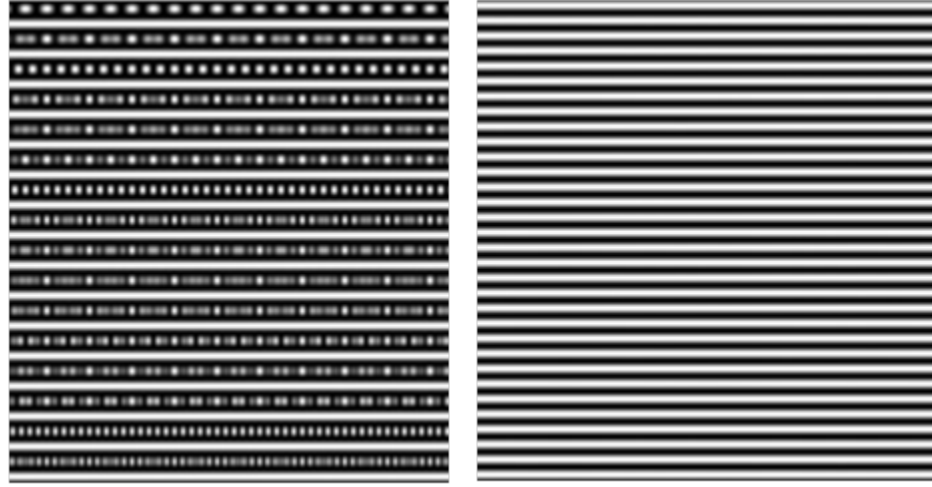


Figure 3.2 The two patterns used in Two-Pattern System

Fig. 3.2 left shows an MCP with 15 horizontal modulated snakes (stripes in the horizontal direction). And Fig. 3.2 right shows the sinusoidal pattern with twice the spatial frequency, along the phase direction (y direction of the image), as the MCP. The system setup is a traditional SLI system that consists of a projector and a camera, and set to satisfy the triangulation principle. The system block diagram is shown in Fig. 3.3.

As shown in Fig. 3.3, in the Two-Pattern full lateral resolution SLI depth measuring system, we project the Modified Composite Pattern onto the object surface first and captured the reflected image by the camera, and then the sinusoidal pattern is projected and captured. After the two reflected images are acquired, they are processed into a non-ambiguous phase which is then used to reconstruct the 3D surface. The analysis algorithm and processing procedure will be discussed in the following sections.

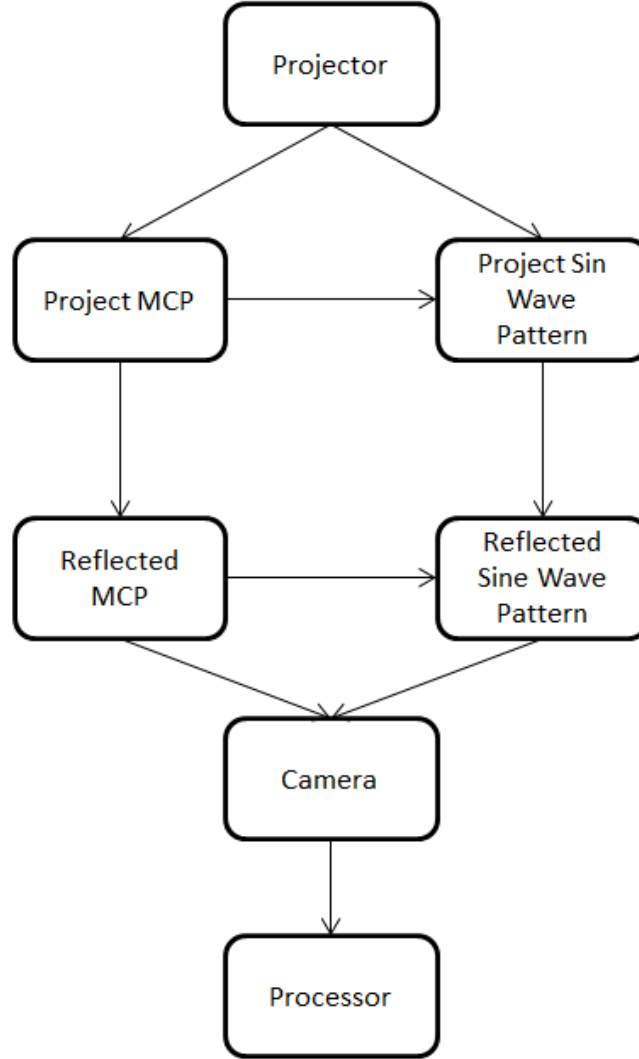


Figure 3.3 Two-Pattern System block diagram

3.3 Non-ambiguous Pattern analysis

We discuss the MCP analysis algorithm which is utilized to reconstruct a non-ambiguous 3D surface approximation. The final result of the Two-Pattern system high depends on the accuracy and non-ambiguity of the depth measuring results from MCP. In Casey's [10] proposed MCP processing method, the 2D Fourier Transform and Band-Pass filtering is used to demodulate the MCP. The accuracy of the demodulation relies on the filtering performance and requires identification of each frequency component. We

introduce a new MCP analysis algorithm that utilizes the 2nd sinusoidal pattern to improve snake detection.

MCP is a pattern encoded both along the phase and orthogonal dimensions. Casey, et al. thoroughly describes the details of MCP design in reference [10]. A MCP has two kinds of snakes. One is un-modulated “white” snakes; the other is horizontally modulated snakes. The Amplitude-Modulation (AM) modulated snakes are a weighted combination of different sinusoidal waves with different spatial frequencies. The weight is based on a gray code. The phase image is non-ambiguous at each of the modulated snakes. A MCP in Fig. 3.2 left is defined as

$$I(x, y) = \left\{ \left[\sum_{i=1}^N \frac{1}{2} G_i(x, y) \cdot (\cos(2\pi f_i x) + 1) \right] \cdot S(x, y) + W(x, y) \right\} \cdot A_{PMP}(x, y) \quad (3.1)$$

where

$$A_{PMP}(x, y) = a(x, y) + b(x, y) \cos(2\pi f_c y), \quad (3.2)$$

$$S(x, y) = \sum_{m=1}^{N_s} \text{rect} \left(\frac{y - 2mT_c}{T_c} \right), \quad (3.3)$$

and

$$W(x, y) = \sum_{m=1}^{N_s} \text{rect} \left(\frac{y - (2m+1)T_c}{T_c} \right). \quad (3.4)$$

The result, $I(x, y)$, is the Modified Composite Pattern image, and i is the index number of Gray Code modulated snakes from 1 to N . G_i is the i th binary Gray code pattern. The i th modulation carrier frequency is f_i , S is the rectangular stripe mask function which modifies the Composite Pattern, and W is the rectangular function defining the un-modulated stripes [17]. The multiplication operation used here is Hadamard element-wise matrix multiplication [22], and $T_c = 1/f_c$.

The number of carrier frequencies can be varied based on the spatial frequency of the sinusoidal wave along the phase direction. In our Two-Pattern system, four carrier spatial frequencies are used, since there are total 32 snakes in the pattern. As shown in Table 3-1 the MCP uses 4 orthogonal frequencies so the maximum number of modulated snakes

are $2^4 - 1 = 15$ where $\{0, 0, 0, 0\}$ pattern is not included. These modulated snakes are identified by a snake code number and a phase code as shown in Table 3-1.

Table 3-1 Phase Code (PC), Snake Code (SC) and Gray code (GC)

PC	SC	GC $\{f_4, f_3, f_2, f_1\}$	PC	SC	GC $\{f_4, f_3, f_2, f_1\}$
0	0	N/A	8	12	1100
1	1	0001	9	13	1101
2	3	0011	10	15	1111
3	2	0010	11	14	1110
4	6	0110	12	10	1010
5	7	0111	13	11	1011
6	5	0101	14	9	1001
7	4	0100	15	8	1000

The Phase code (PC) of a snake in the table is the snake number, since each snake is indexed along the phase direction from the top of the image to the bottom, so the modulated snake on the top most of the image is number as 1 and the other are numbered accordingly. The Gray Code (GC) of a snake indicates which carrier frequencies are used to modify the current snake, for example, if the Gray Code of a modulated snake is 1011, then this snake is horizontally modulated by three carrier frequencies: f_4, f_2 , and f_1 , since $\{f_4, f_3, f_2, f_1\}$ represents the Gray Code of the snake. And Snake Code (SC) is the decimal representation of the Gray Code.

3.3.1 Peak Isolation

MCPimage analysis and processing begins with a single image of an object illuminated by the projected MCP i.e. pattern 1. The first step is isolation of the stripe peaks. To get a better result, a 1-D filter is used to pre-filter the captured image along the phase direction. The 1-D filter is a moving average filter on the phase direction, and it is one column wide

and the height of the filter corresponds to half of the vertical period of the snakes. This filter will blur the image slightly in the phase direction without affecting the details in the orthogonal direction. In this way, it will improve detection of the modulated snakes in the next step. As shown in Fig. 3.4, the left image is the original captured image, and the right one is the image after filtering. We can see the eyebrow part is suppressed in the filtered image.

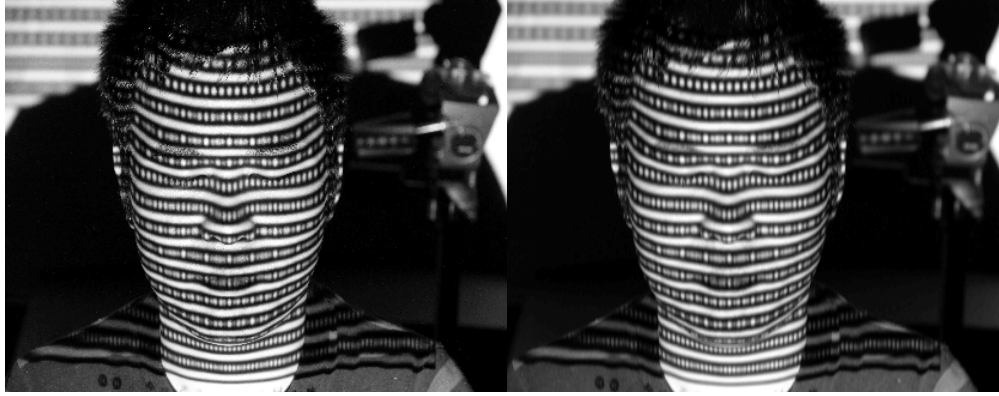


Figure 3.4 Pre-Filter the image. Original Image (left), filtered image (right)

To isolate the peaks of the snakes of the MCP, the high frequency sinusoidal pattern is utilized. The second pattern has the same spatial frequency along the phase direction as the MCP image, so the snake peak locations are exactly the same. To get the peak location along phase direction of 2nd pattern, a threshold T_s is set to detect the snake region of the 2nd pattern. A snake isolation mask is defined by Eq. (3.5).

$$B_{pr}(x, y) = \begin{cases} 0, & I_2(x, y) < T_s \\ 1, & I_2(x, y) \geq T_s \end{cases} \quad (3.5)$$

Where $B_{pr}(x, y)$ the binarized peak region is image, and $I_2(x, y)$ is the reflected sinusoidal pattern image.

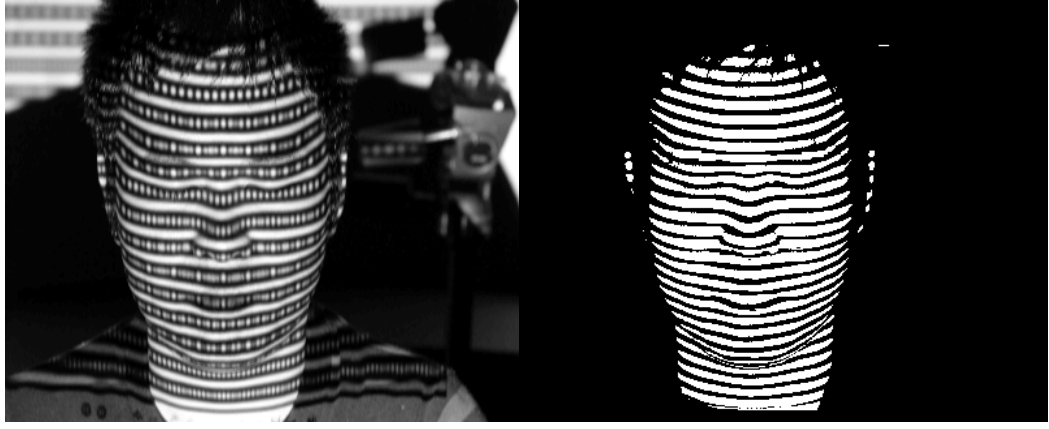


Figure 3.5 Snake Detection Process. Captured Image (left), detected snakes image (right)

As shown in Fig. 3.5 right, the detected snakes regions are in white. Since we don't use negative snakes in the Modified Composite Pattern, we only need to detect the "positive snakes" which are either horizontally modulated or not.

Furthermore, we define the very center of the region of each isolated snake along the phase direction in B_{pr} as the peak location image B_{peak} . B_{peak} is used as an indicator image to isolate the peak pixels in the MCP image as

$$P(x, y) = B_{peak}(x, y) \cdot I_2(x, y) \quad (3.6)$$

where P is the peaks location and The multiplication operation used in Eq. (3.6) is the Hadamard element-wise matrix multiplication. Fig. 3.6 shows the result image of peak isolation, although in the Fig. 3.6 the peaks lines seem discontinued, it is caused by the MATLAB display function down-sampling process.

In our peak isolation algorithm, instead of identifying the peak location directly in Modified Composite Pattern image, we utilize the 2nd pattern to help isolation. This is a big advantage of using a 2nd pattern compared with single pattern technique that just using MCP to isolate the peaks of each snakes, since the snakes are modulated horizontally which corrupts the results of the binarization of the image, and other image segmentation algorithms also have a hard time to identify the peaks.

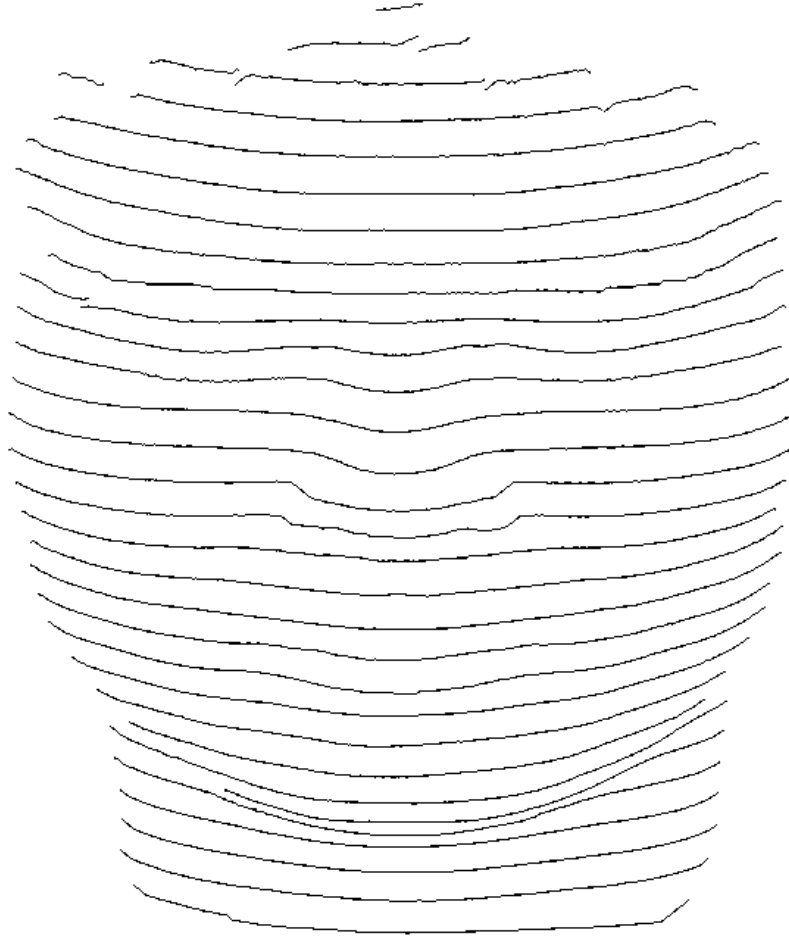


Figure 3.6 Detected Snake Peaks image (negative image)

After the peaks locations are identified, each snake's peak pixel intensity in P is mapped to a sequence in matrix Y defined as

$Y \equiv$ Matrix of Sequences of each snake's peak intensity , and in matrix form Y such that

$$Y = \begin{bmatrix} y_1 \\ y_2 \\ \vdots \\ y_{M_s} \end{bmatrix} \quad (3.7)$$

where $M_s \equiv$ Number of detected snakes , $N_s \equiv$ Maximum length of the snakes , and $y_i \equiv$ 1 by N_s vector.

In this way, we store each detected snakes' peaks into a row of matrix \mathbf{Y} as shown in Eq. (3.7). The reason to create a matrix \mathbf{Y} is that demodulating a 1D Amplitude Modulated signal is much easier than demodulating a 2D AM image. We also apply a 1-D low-pass filter to each of the 1-D snakes' peaks to filter out some high frequency noise, as shown in Fig. 3.7.

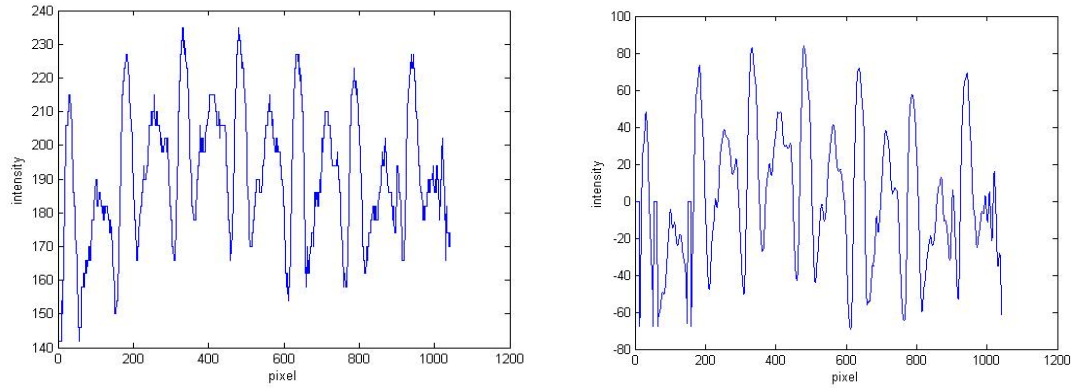


Figure 3.7 The snake before filtering (left), the snake after filtering (right)

3.3.2 Modified Composite Pattern Demodulation by Using Matched Filter Bank

The second step is the MCP demodulation. A Matched Filter bank method is used to identify each snake. There are 4 frequency components in each snake so we need to use 15 matched filters. Each frequency component has N_s length, and according to the Surface Modulation Transfer Function (SMTF), the higher frequencies may be suppressed in the captured image, so the matched filter is formed from a selected subset of weighted cosine waves defined by

$$s_1(n) = \alpha_1 \cdot \cos\left(2\pi \frac{k_1}{N_s} n\right) \quad (3.8a)$$

$$s_2(n) = \alpha_2 \cdot \cos\left(2\pi \frac{k_2}{N_s} n\right) \quad (3.8b)$$

$$s_3(n) = \alpha_3 \cdot \cos\left(2\pi \frac{k_3}{N_s} n\right) \quad (3.8c)$$

$$s_4(n) = \alpha_4 \cdot \cos\left(2\pi \frac{k_4}{N_s} n\right) \quad (3.8d)$$

The weights are set by experience to compensate for the frequency attenuation. A set of weights use for this study is in the Table 3-2.

Table 3-2 The weights for matched filters used in our research

	α_1	α_2	α_3	α_4
<i>value</i>	<i>1.2</i>	<i>1.2</i>	<i>0.45</i>	<i>0.15</i>

A matrix of 15 matched filters is given by Eq. (3.9), where \mathbf{H} is a 15 by N_s matrix.

$$\mathbf{H} = \begin{bmatrix} s_1(n) & , \text{when } SC = 1 \\ s_1(n) + s_2(n) & , \text{when } SC = 3 \\ s_2(n) & , \text{when } SC = 2 \\ \vdots & \\ s_1(n) + s_2(n) + s_3(n) + s_4(n) & , \text{when } SC = 15 \end{bmatrix} \quad (3.9)$$

To simplify the representation, we refer each row of \mathbf{H} as a vector \mathbf{h}_i :

$$\mathbf{H} = \begin{bmatrix} \mathbf{h}_1 \\ \mathbf{h}_2 \\ \vdots \\ \mathbf{h}_i \\ \vdots \\ \mathbf{h}_{15} \end{bmatrix} \quad (3.10)$$

Then, we utilize the prebuilt Matched Filter Bank to demodulate the extracted 1-D snakes' peaks which are stored in matrix \mathbf{Y} as expressed in Eq. (3.7). The matched filter correlation is implemented by:

$$\mathbf{e}_{i,j} = \mathbf{y}_i * \mathbf{h}_j^*(-n) \quad (3.11)$$

where superscript *denotes conjugation and operator *denotes convolution. After the Discrete Fourier Transform (DFT) of both sides of Eq. (3.11), we get

$$DFT[\mathbf{e}_{i,j}] = DFT[\mathbf{y}_i] \cdot DFT[\mathbf{h}_j^*(-n)] \quad (3.12)$$

which can be rewritten as

$$\hat{e}_{i,j}(f) = \hat{y}_i(f) \cdot \hat{h}_j^*(f) \quad (3.13)$$

where \wedge denotes the DFT form of the signal. In matrix form this yields

$$\hat{\mathbf{E}} = \hat{\mathbf{Y}} \cdot \hat{\mathbf{H}}^T = \begin{bmatrix} \hat{e}_{1,1}(f) & \hat{e}_{1,2}(f) & \cdots & \hat{e}_{1,15}(f) \\ \hat{e}_{2,1}(f) & \vdots & \vdots & \vdots \\ \vdots & \hat{e}_{i,j}(f) & \vdots & \vdots \\ \hat{e}_{Ms,1}(f) & \cdots & \cdots & \hat{e}_{Ms,15}(f) \end{bmatrix}_{Ms \times (15 \cdot Ns)} \quad (3.14)$$

After the matched filter correlation, the maximum correlation peaks and the indices are found and represented by

$$\begin{aligned} \mathbf{C} &= \underset{j \text{ for each row}}{\operatorname{argmax}} \left(DFT^{-1}(\hat{\mathbf{E}}) \right) \\ &= \underset{j \text{ for each row}}{\operatorname{argmax}} (\mathbf{E}) = \begin{bmatrix} \mathbf{c}_1 \\ \mathbf{c}_2 \\ \vdots \\ \mathbf{c}_i \\ \vdots \\ \mathbf{c}_{Ms} \end{bmatrix}_{Ms \times 1} \end{aligned} \quad (3.15)$$

where $\mathbf{c}_i = j$ indicates that for the i th snake, the maximum correlation is with the j th code. If the maximum value for i th row in \mathbf{E} is below a threshold T_E , then this snake is considered as an un-modulated snake, and $\mathbf{c}_i = 0$ to eliminate that snake from the set of modulated snakes.

Fig. 3.8 summarizes the algorithm of non-ambiguity pattern analysis process. We first read in the captured MCP image and pre-filter it with a 1D moving average filter and then we identify the snake region by binarizing the second sinusoidal pattern. The 1D snakes peaks are extracted from the snake peak image and these 1D snake peaks are used for demodulation. For demodulation procedure, we first pre-build a Matched Filter Bank which consists of 15 matched filters, and then correlate the Matched Filter Bank with the 1D snake peaks to demodulate each snake and get the Snake Code back.

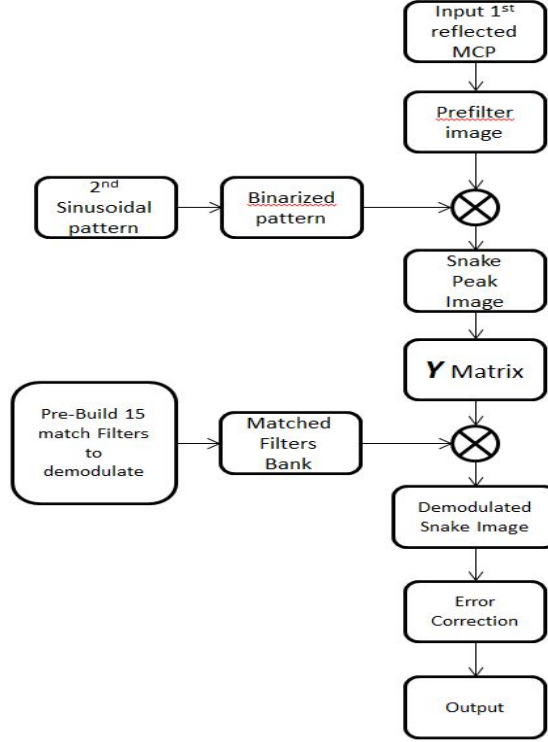


Figure 3.8 Algorithm of Modified Composite Pattern processing

3.3.3 Phase Image Reconstruction by Using Demodulated Snakes

After the demodulation process, based on the calibration results for each snakes in the MCP image, we reconstruct the S_y matrix as shown in Fig. 3.9 left. This format is named as MAT5, and the details of MAT5 are described in [9]. The S_y image indicates the depth for each snake peak, so in order to get phase image for the whole surface that covered by the MCP, we need to do 1-D linear interpolation along the phase direction between each two adjacent snakes. Fig. 3.9 right shows the final phase image (depth image) that is used for un-wrapping the second pattern phase. Also, from Fig. 3.9, we know that the phase image generated by MCP is non-ambiguous, since each snakes' Snake Code is different, which indicates the absolute phase value of the snake, and the phase value is obtained from calibration procedure. The phase value between the snakes is calculated by utilizing the linear interpolation, so the phase value is not wrapped, which means the phase image is not ambiguous.

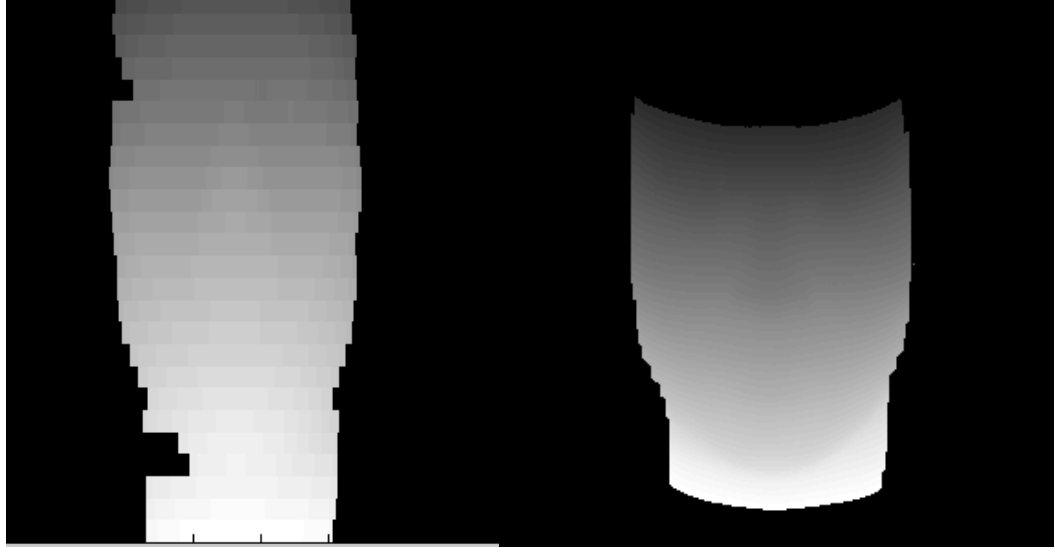


Figure 3.9 S_y image (left), linear interpolated phase image (right)

3.4 Quadrature Phase Pattern Analysis

In section 3.3, we discussed the method of processing non-ambiguous MCP data based on a Matched Filter Bank technique. However, the phase resolution of that processing is limited to the snake's width or period in the phase direction. In this section, we process the second pattern using a Quadrature Phase (QP) processing technique to achieve full lateral resolution.

Quadrature processing yields a wrapped phase image from a single captured pattern image. By using the non-ambiguous phase of modulated snakes that we already acquired in section 3.3, we un-wrap the wrapped phase image to achieve both high lateral resolution and non-ambiguous surface depth.

Section 3.4.1 illustrates the mathematical model for quadrature processing, and thoroughly discusses the details of this technique. Section 3.4.2 provides an explanation of unwrapping algorithm, and its implementation.

3.4.1 Mathematical model of Quadrature Processing (QP)

As we described in section 3.3, the mathematical representation of MCP is defined in Eq.

(3.1). To simplify the representation, we represent the Gray Code modulation as

$$G(x, y) = \left[\sum_{i=1}^N \frac{1}{2} G_i(x, y) \cdot (\cos(2\pi f_i x) + 1) \right] \quad (3.16)$$

The captured distorted MCP pattern in camera coordinate is:

$$I(x_c, y_c) = [\tilde{G}(x_c, y_c) \tilde{S}(x_c, y_c) + \tilde{W}(x_c, y_c)] \cdot \widetilde{A_{PMP}}(x_c, y_c) \quad (3.17)$$

Then by substituting $\widetilde{A_{PMP}}(x_c, y_c)$ by Eq. (3.2), the Eq. (3.17) is rewritten as Eq. (3.18a)

$$I(x_c, y_c) = M(x_c, y_c) \cdot a(x, y) + M(x_c, y_c) \cdot b(x, y) \cos(2\pi f_c y_c + \theta(x_c, y_c, z)) \quad (3.18a)$$

where $M(x_c, y_c)$ is:

$$M(x_c, y_c) = [G(x_c, y_c) S(x_c, y_c) + W(x_c, y_c)] \quad (3.18b)$$

the Eq. (3.18a) is rewritten as

$$I(x_c, y_c) = \hat{a}_{MCP}(x_c, y_c) + \hat{b}_{MCP}(x_c, y_c) \cos(2\pi f_c y_c + \theta(x_c, y_c, z)) \quad (3.19)$$

Also, The reflected 2nd pattern intensity in camera space $\{x, y\}$ is

$$I_2(x, y) = \hat{a}(x, y) + \hat{b}(x, y) \cos(2\pi f_c y + \theta(x, y, z_w)) \quad (3.20)$$

where $\hat{a}(x, y)$ is the reflected ambient plus projected light dc intensity times the surface albedo in the direction of the camera. The term $\hat{b}(x, y)$ is only the cosine contribution to the reflected light intensity, also multiplied by the surface albedo in the direction of the camera. All terms are also attenuated by the surface gradient. The phase term is a function of the camera coordinate and z_w is a world coordinate.

From Eq. (3.19) and Eq. (3.20), we know that both patterns have the similar mathematical form, which can be used for Quadrature Processing, the reason we introduce the 2nd pattern for Quadrature Processing is that the phase generated by the 2nd pattern has much less noise and is not corrupted by the horizontal modulation.

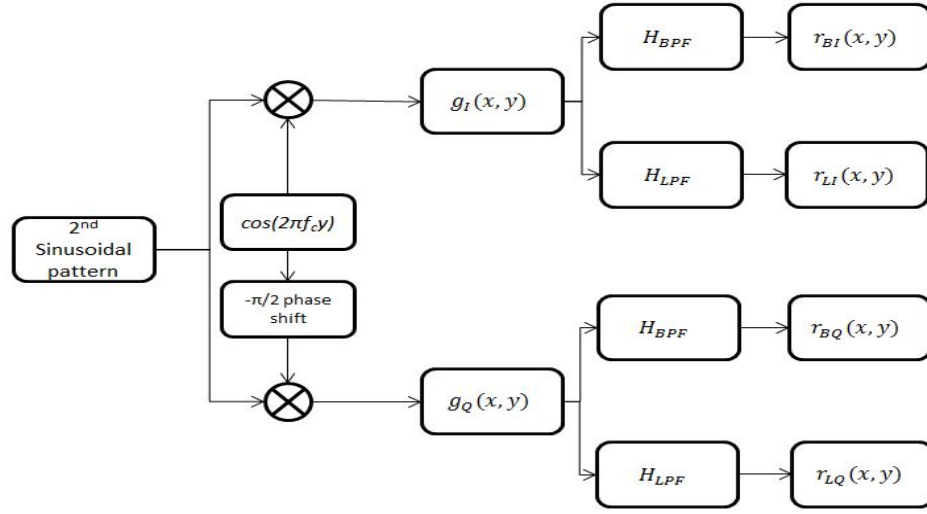


Figure 3.10 Quadrature Phase Demodulator

The Quadrature Processing procedure is shown in the Fig. 3.10. The first step is to generate an in-phase function $g_I(x, y)$, and quadrature function $g_Q(x, y)$, by multiplying the cosine image, $\cos(2\pi f_c y)$ and sine image, $\sin(2\pi f_c y)$ with reflected image $I_2(x, y)$. The reference frequency f_c is chosen to be the frequency of the captured image reflected off a flat calibration surface.

So, the in-phase component $g_I(x, y)$ and the quadrature component $g_Q(x, y)$ are

$$g_I(x, y) = (\hat{a}(x, y) + \hat{b}(x, y) \cos(2\pi f_c y + \theta(x, y))) \cdot \cos(2\pi f_c y), \quad (3.21)$$

and

$$g_Q(x, y) = (\hat{a}(x, y) + \hat{b}(x, y) \cos(2\pi f_c y + \theta(x, y))) \cdot \sin(2\pi f_c y), \quad (3.22)$$

respectively. Using trigonometric identities with Eq. (3.21) and (3.22) yields

$$\begin{aligned} g_I(x, y) &= \hat{a}(x, y) \cos(2\pi f_c y) + \frac{\hat{b}(x, y)}{2} \cos(\theta(x, y)) \\ &\quad + \frac{\hat{b}(x, y)}{2} \cos(4\pi f_c y + \theta(x, y)) \end{aligned} \quad (3.23)$$

and

$$\begin{aligned}
g_Q(x, y) = & \hat{a}(x, y) \sin(2\pi f_c y) - \frac{\hat{b}(x, y)}{2} \sin(\theta(x, y)) \\
& + \frac{\hat{b}(x, y)}{2} \sin(4\pi f_c y + \theta(x, y))
\end{aligned} \tag{3.24}$$

The filters in Fig. 3.10 are a 1-Dimensional and only applied along the phase dimension y . We use two filters; one is a band pass filter HBPF with center frequency at f_c and bandwidth smaller than $2f_c$, the other is a low pass filter HLPF with cut frequency at $f_L \leq f_c$. Both g_I and g_Q will be filtered to yield four filtered images as output. As shown in Fig. 3.10, the outputs images are $r_{BI}(x, y)$ and $r_{LI}(x, y)$, which come from by filtering the g_I , $r_{BQ}(x, y)$ and $r_{LQ}(x, y)$ which come from by filtering the g_Q .

$$r_{BI}(x, y) = \hat{a}(x, y) \cos(2\pi f_c y) \tag{3.25a}$$

$$r_{LI}(x, y) = \frac{\hat{b}(x, y)}{2} \cos(\theta(x, y)) \tag{3.25b}$$

$$r_{BQ}(x, y) = \hat{a}(x, y) \sin(2\pi f_c y) \tag{3.25c}$$

$$r_{LQ}(x, y) = -\frac{\hat{b}(x, y)}{2} \sin(\theta(x, y)) \tag{3.25d}$$

The high frequency components in Eq. (3.23) and Eq. (3.29) are filtered out. By using the four outputs in Eq. (3.25), the average intensity, $\hat{a}(x, y)$, intensity modulation, $\hat{b}(x, y)$ and phase, $\theta(x, y)$ can be calculated by

$$\hat{a}(x, y) = \sqrt{r_{BI}(x, y)^2 + r_{BQ}(x, y)^2} \tag{3.26a}$$

$$\hat{b}(x, y) = 4\sqrt{r_{LI}(x, y)^2 + r_{LQ}(x, y)^2} \tag{3.26b}$$

$$\theta(x, y) = \arctan\left(-\frac{r_{LQ}(x, y)}{r_{LI}(x, y)}\right) \tag{3.26c}$$

However, the phase image is wrapped, as shown in Fig. 3.11, so we need to use the MCP phase image as a baseline phase image to unwrap the $\theta(x, y)$.

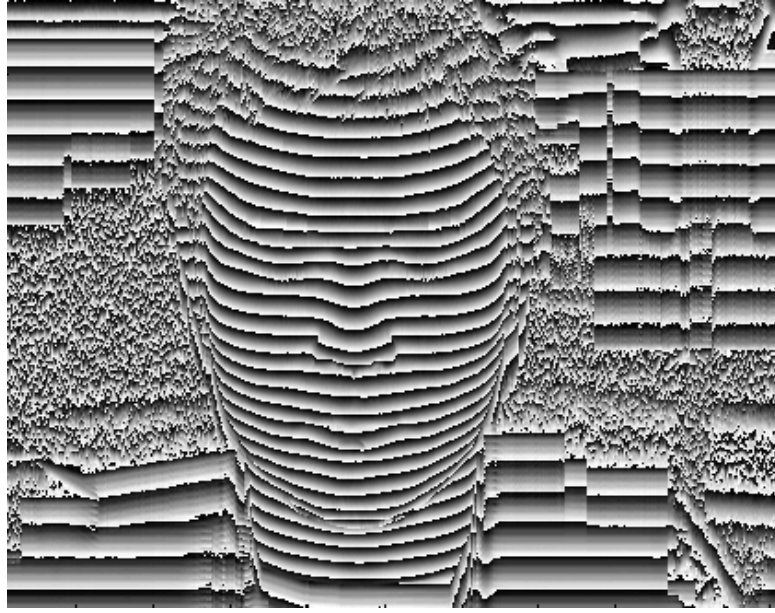


Figure 3.11 Wrapped Phase Image

3.4.2 Quadrature Processing Phase Unwrapping

The first step to unwrap the phase is to mask out the noise outside object border, since we only need the phase image for the object scanned. So we set our Region of Interest (ROI) to the object, mask out all the other noise. As shown in Fig. 3.12 left, the border of the object is in black.

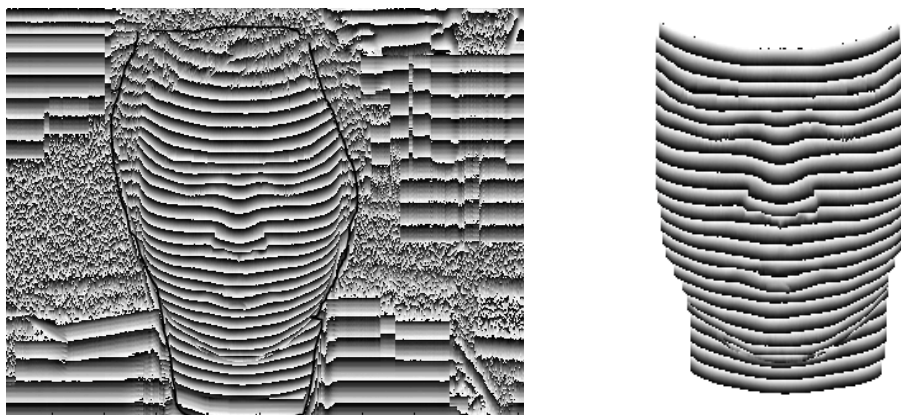


Figure 3.12 Object Bolder in black(left), masked out ROI image(right)

From Section 3.4.1, we get the average image, indicator image, and the phase image from

the quadrature processing, and to get the ROI of the phase image, we utilize the indicator image. A threshold T_b is set to binarize the intensity modulation image into an indicator image, which is

$$\hat{b}(x, y) = \begin{cases} 1, & \hat{b}(x, y) \geq T_b \\ 0, & \hat{b}(x, y) < T_b \end{cases} \quad (3.27)$$

Then, by multiplying the phase image by the binarized indicator image, we mask out the phase noise, such that

$$\theta(x, y) = \theta(x, y) \cdot \hat{b}(x, y) \quad (3.28)$$

The masked phase image boundary is shown in Fig. 3.12 right.

With noise removed, our unwrapping algorithm works robustly on the wrapped phase in Fig. 3.12 right. The basic idea of the unwrapping algorithm is to scale the wrapped phase to follow the trend of the Modified Composite Pattern phase we got from the first pattern. If we take a cross section (i.e., a single column) of both phase images, one is wrapped and the other is unwrapped baseline MCP phase image [86] [87], as shown in Fig. 3.13.

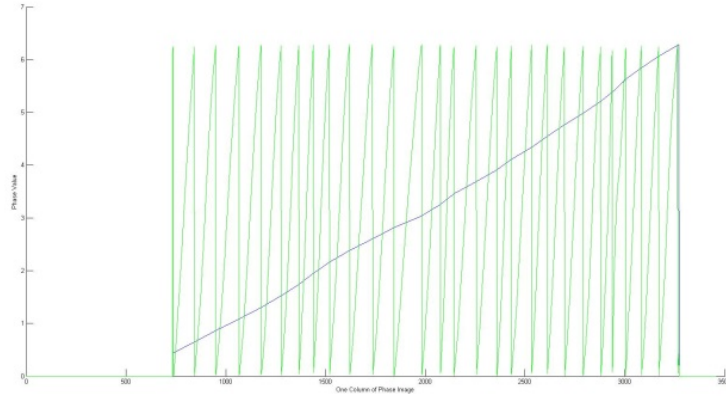


Figure 3.13 One column signal of both phase images, Green in wrapped phase image, Blue is the baseline unwrapped phase image

In preparation to unwrap the phase, $\theta(x, y)$, we normalize it by dividing by its pattern spatial frequency of $k_c = 29$. The two normalized signals have same gradient. The first step is to obtain the integer number of phase unwrapping wavelengths (unwrapping

cycles) that are at or below the desired value such that

$$\lambda(x, y) = \text{floor}\left(\frac{k_c \varphi_0(x, y) - \varphi_1(x, y)}{2\pi}\right) \quad (3.29)$$

where $\varphi_0(x, y)$ is the baseline unwrapped phase image, $\varphi_1(x, y)$ is the wrapped phase image, and k_c is the $\varphi_1(x, y)$ pattern spatial frequency. Then we need to scale the $\varphi_1(x, y)$ to baseline phase. So, in units of cycles, the difference between baseline phase and unwrapping cycle is calculated as

$$r(x, y) = \frac{k_c \varphi_0(x, y) - \varphi_1(x, y) - 2\pi \lambda(x, y)}{2\pi} \quad (3.30)$$

A final adjustment of +/- 1 unwrapping cycle is determined by evaluating the remainder such that

$$\lambda_u(x, y) = \begin{cases} \lambda(x, y) + 1, & \text{for } r(x, y) > 0.5 \\ \lambda(x, y) - 1, & \text{for } r(x, y) < -0.5 \end{cases} \quad (3.31)$$

The phase image is unwrapping by

$$\varphi_u(x, y) = \frac{2\pi \lambda_u(x, y) + \varphi_1(x, y)}{k_c} \quad (3.32)$$

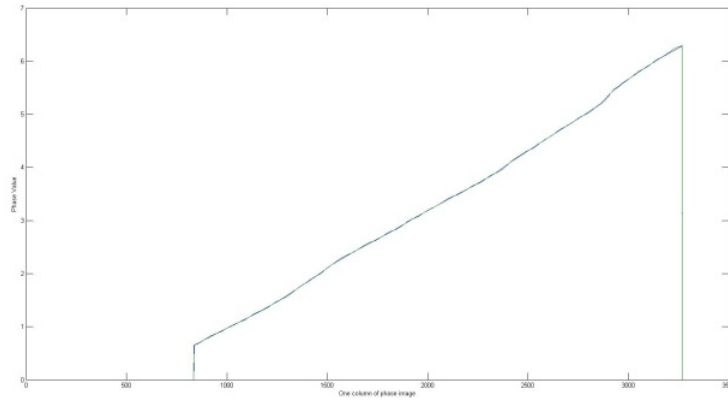


Figure 3.14 Unwrapped phase and baseline phase

Fig. 3.14 displays a column of the unwrapped quadrature phase plotted with baseline MCP phase. The unwrapped phase follows the baseline phase very closely. However, the unwrapped quadrature phase has much more high frequency components which represent

the details of the surface. And, the quadrature phase is full lateral resolution. The final unwrapped phase image is shown in fig. 3.15.

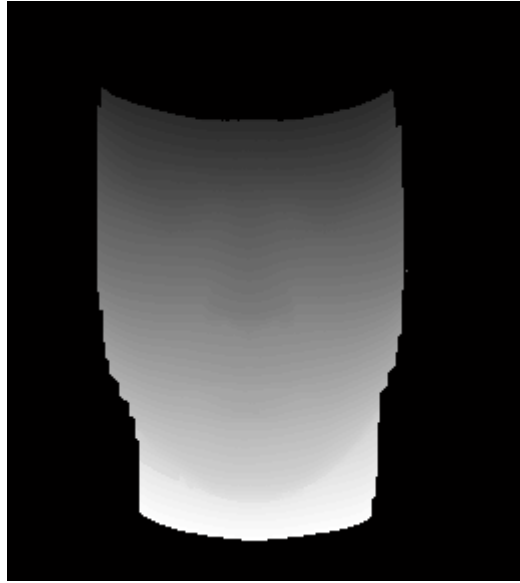


Figure 3.15 Unwrapped Quadrature Processing Phase Image

With the phase image shown in Fig. 3.15, we reconstruct the full lateral resolution 3D surface directly.

3.5 Experiments Results

The previous sections describe and discuss the research of Two-pattern Full Lateral Resolution (2PFLR) SLI depth measuring system, and in section 3.4 and section 3.5 explicitly illustrates the details of the analysis of the non-ambiguous pattern, which is Modified Composite Pattern, and analysis of Quadrature Phase Pattern, which is utilized for full lateral resolution 3-D reconstruction. In this section, we present the experiments results of our Two-pattern system.

In section 3.5.1, we demonstrate the Experiment setup for Two-Pattern Full Lateral Resolution SLI depth measuring system. Then, in section 3.5.2 we first present the 3D reconstruction results of using Modified Composite Pattern only. In section 3.5.3, we demonstrate our Two-pattern system's 3D surface reconstruction result and compared with other single pattern technique such as MCP or Composite Pattern.

3.5.1 Experiment Setup for Two-Pattern Full Lateral Resolution SLI System

The system apparatus for 2PFLR system is described. The Two-Pattern 3D scanner setup is based on the classical SLI scanner as shown in Fig. 3.16.

This system is a classic SLI system set up with a camera and a projector in triangulation geometry. A high definition camera is used here to capture the projected pattern. We use a Canon EOS-7D high definition camera with resolution 5184 x 3456 and a ViewSonic PJ260D digital projector with resolution 1024*768.

The distance between the camera and the projector is 14 inches, and the object is 24 inches away from the projector lens.



Figure 3.16 Two-Pattern Full Lateral Resolution Scanner Structure

To calibrate this system, we follow the calibration method by using a roof grid with circle features as shown in Fig. 3.17. Unlike some other classical calibration target such as Checker Board [85], this roof grid makes the calibration procedures for Structure Light

Illumination system to be based on one scan [29]-[31]. The calibration points are the known centers of all the circles on the calibration grid [34]. The angle of the roof is 90 degree. Here, the Z axis is pointing into the Fig. 3.17. The second step is to generate the phase image of the calibration grid by using our Two-Pattern Structure Light Illumination System. Then, in our calibration software, we read in the calibration target's captured image and automatically detect the center of each circle, and obtain the phase value associated with each center, as shown in Fig. 3.18. The green square around the ring means this ring is automatically identified, and the cross in the square points out the center of the ring. The automatic ring center detection algorithm is proposed by Hassebrook.

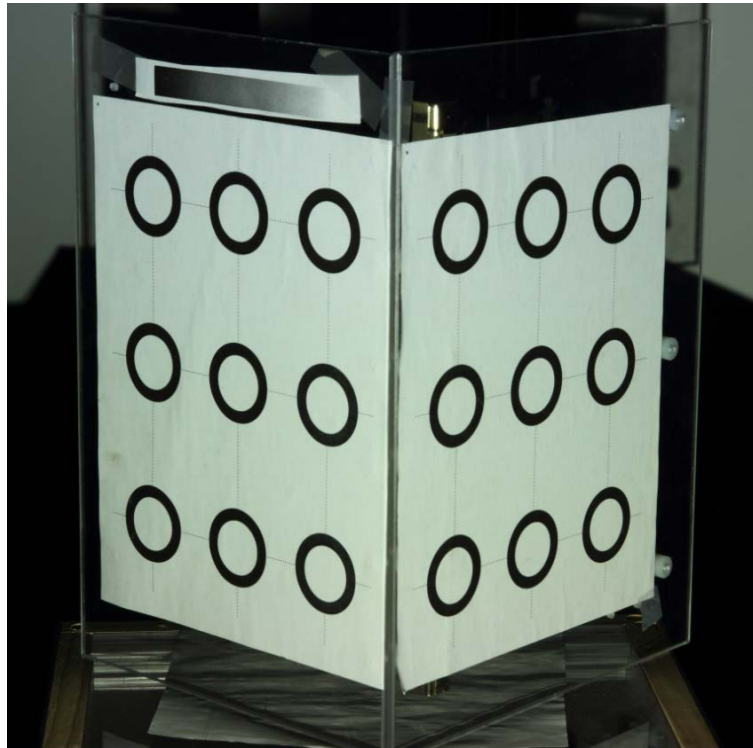


Figure 3.17 Calibration Target [94]

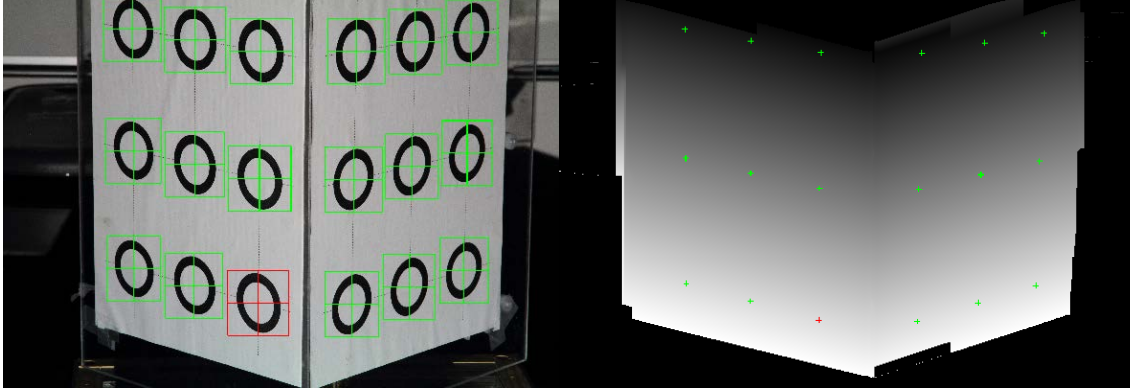


Figure 3.18 Automatically detect the rings' centers (left), Phase Image with detected center in green (right)

Each circle's center's world coordinates are known, and in this way, with the phase value of each center, the system parameters are calculated. The intrinsic and extrinsic parameters of the camera are calculated based on perspective transformation.

3.5.2 Modified Composite Pattern 3D reconstruction

As described in section 3.5.2, the 3D surface is reconstructed directly using the phase image generated by MCP as shown in Fig. 3.9. The reconstructed 3D surface by using single Modified Composite Pattern is shown in Fig. 3. 19.

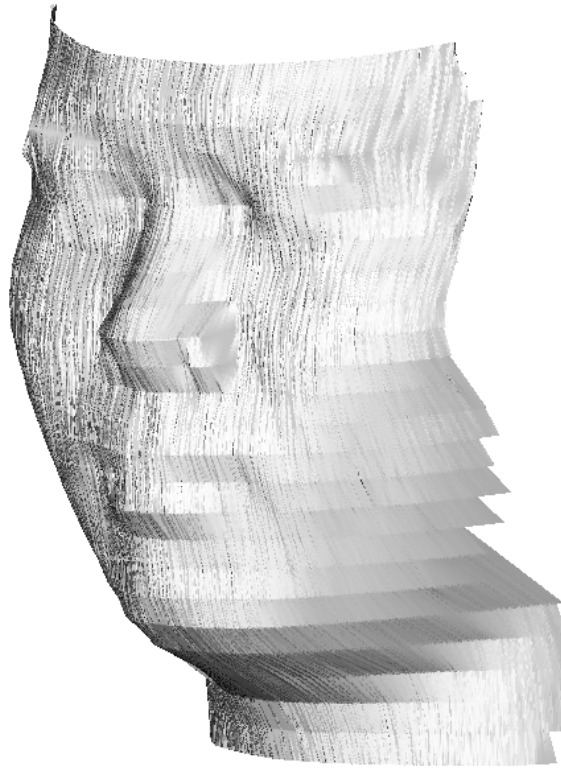


Figure 3.19 3D surface reconstructed only use MCP

We see in Fig. 3.19 the surface is not full lateral resolution since the phase image generated by Modified Composite Pattern is interpolated between adjacent snake peaks. If we are only going to use the MCP for 3-D reconstruction, then a trend filter is applied to smooth the sharp peaks on the 3D surface as shown in Fig. 3.20. The trend filter is a low pass filter, so the surface loses some high frequency details.



Figure 3.20 Surface after Trend-filtering



Figure 3.21 3D surface with color texture

Fig. 3.21 shows the final result with color texture mapping to it. Note that, even after some post processing procedure including trend filtering, there are still some obvious defects in the 3D surface such as the nose area.

3.5.3 Two-Pattern Full Lateral Resolution 3D reconstruction result

As demonstrated in section 3.5.2, reconstruction using only Modified Composite Pattern technique is not able to reach the full lateral resolution, and this is also the problem that all the other single pattern techniques have. As described in section 3.4, the Quadrature Phase processing of the 2nd high frequency sinusoidal pattern provides the phase image without interpolation.

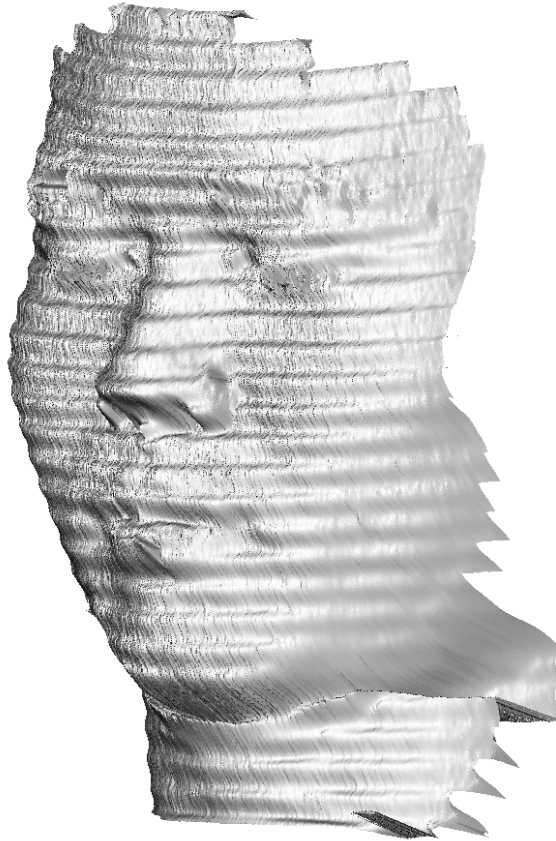


Figure 3.22 3D reconstruction by using Quadrature Phase Processing

Fig. 3.22 shows 3D reconstruction result by using Two-Pattern Full Lateral Resolution SLI system. The phase image used in reconstruction is shown in Fig. 3.15. As shown in Fig. 3.22, the 3D surface has a lot of banding artifact across the surface; we call this

“banding error” which is caused by the projected sinusoidal pattern. Banding error is a common issue of Structure Light Illumination techniques, especially in single pattern technique. We discuss the banding issue and propose a solution in the next chapter. However, compared with Fig. 3.22 with Fig. 3.19, we can easily see that the surface from Two-Pattern Full Lateral Resolution system has much higher resolution and much more details than the surface only using MCP. We just need to suppress the banding error.

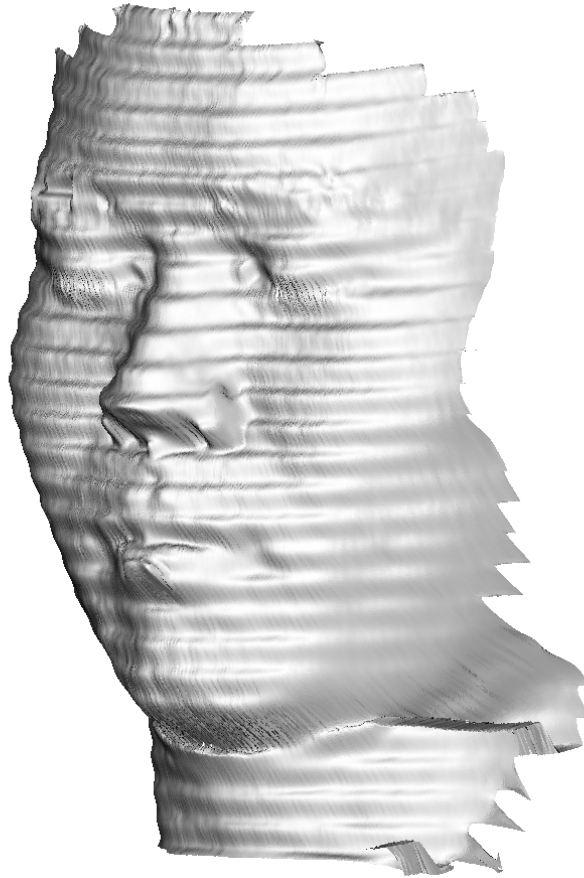


Figure 3.23 QP reconstructed surface after trend filter

Fig. 3.23 displays the Quadrature Phase reconstructed surface after trend filtering procedure as we did for MCP reconstructed surface. However, the banding error on the surface is not suppressed by filtering technique. The final result with color texture mapping is shown in Fig. 3.24.



Figure 3.24 Colored 3D surface

3.6Summary

This chapter we thoroughly define on Two-Pattern Full Lateral Resolution Structure Light Illumination depth measuring system. The full lateral resolution 3D surface result is able to be reconstructed by utilizing only two patterns by using our system. This is of great significance since we allow the relative motion between the scanner and the object within the FOV of the scanner just as other single pattern techniques,

In our system, two patterns are used to reconstruct the 3D surface. The first pattern is a Modified Composite Pattern, and this MCP is utilized as a non-ambiguous pattern, which means the 3D results reconstruct by this pattern is non-ambiguous. But MCP only is not able to provide the 3D result with full lateral resolution, only a coarse 3D surface. The second pattern is a high frequency sinusoidal pattern that is utilized as an ambiguous but full lateral resolution pattern. To process the sinusoidal pattern, we proposed a novel

Quadrature Phase processing method which effectively and efficiently processes the pattern and generates the ambiguous phase image. Then, a baseline un-wrapping method is needed to un-wrap the phase image; this method is much more robust compared with Goldstein un-wrapping method.

However, the reconstruction 3D surface is still corrupted by the banding error which is a noise caused by the projected sinusoidal pattern. We introduce methods to reduce this problem in next chapter.

Chapter 4 Projector Space De-banding Algorithm

We know that the accuracy of the 3D reconstruction results of the Structure Light Illumination system highly rely on the accuracy of the phase image, because the 3D surface is directly reconstructed by using the phase image. If there is banding noise or distortion in the phase image, the final 3D depth measurement will be corrupted. From many experiments, we know that SLI techniques are prone to banding error. As shown in Fig. 3.26, the Quadrature Phase Processing of the sinusoidal wave pattern has significant banding error. The de-banding of 3D is a research topic. As described in the introduction, utilizing more patterns does reduce and suppress harmonics, and in this way, reduce banding artifact. However, these multi-pattern methods sacrifice the time efficiency of 3D scanning system and are in conflict with our research purpose to develop a high speed 3D scanning system that allows the relative motion between the target surface and scanner.

Some de-banding methods use the de-focusing of the projected pattern to create a more ideal sinusoidal pattern. However, de-focused the projector has very limited measurement range. The majority state-of-art de-banding methods estimate the banding error and compensate distortion for it. However, to estimate the banding error is not easy since the projected pattern is curved by the object's surface. We propose a novel Projector Space De-banding algorithm to de-band the surface effectively and efficiently.

The following sections in this chapter are organized as follows: section 4.1 briefly describes our de-banding algorithm. Section 4.2 illustrates the mathematical model of the de-banding algorithm. Section 4.3 summarizes all the notations and mathematical representation used in the section 4.2 and put them into a table. Section 4.4 demonstrates the de-banded 3D surface and compared with other techniques. Section 4.5 describes a performance characterization method for any SLI system. Section 4.6 is the summary of the whole chapter.

4.1 Introduction to Projector Space De-banding Algorithm

As mentioned above, our research on de-banding is based on the main-sequence banding

error correction research, which focuses on eliminating the banding error in the calibration procedure and compensates for the distortion in the scanning procedure. However, most of the techniques focus on estimation of the nonlinear gamma distortion and try to eliminate the error by using gamma correction. Several algorithms are developed to estimate the gamma coefficients. However, as mentioned by Guo[12], the gamma distortion in a Structure Light System is not a simple single-parameter gamma function. And quantization error in both camera and projector need to be modeled. These problems limit the effectiveness of the gamma correction algorithms.

As we know, the multi-pattern PMP has the ability to suppress the banding distortion, so the fundamental idea of Projector Space De-banding algorithm is instead of estimating the model banding error directly from one pattern; we utilize our Two-Pattern Full Lateral Resolution SLI system to estimate the mapping from camera space to projector space prior to de-banding. Furthermore, the Modified Composite Pattern yield an interpolated surface between peaks where the peak snakes do not contain banding but do accurately measure the wave length boundaries of the second pattern, as displayed in Fig. 3.19. Note that the strip defect in Fig. 3.19 is caused by linear interpolation in the phase image. So the basic idea of our algorithm is to use the 1st pattern's recovered phase image to estimate the banding error in the 2nd sinusoidal pattern's recovered phase image. Then compensate it in the final phase image.

However, how to estimate the banding error in the 2nd pattern's recovered phase image is the biggest problem that has to be solved. Most passive de-banding methods estimate the banding error during the calibration process and utilize the calibrated banding error to compensate for all future scans. The problem is that the banding error is related to surface depth variation and albedo variation. These banding artifact are difficult to reduce because the phase is distorted by the surface depth and as such, the banding error is difficult to estimate.

We propose post-processing each scan to reduce banding. To avoid the problems with surface interference we introduce a novel Projector Space de-banding algorithm, which instead of estimating the banding error directly in the camera space, we map the

recovered both phase image from 1st and 2nd patterns to the projector space, then estimate the banding error. The advantage of mapping the phase image to the projector space is all the snakes are aligned straight along the horizontal direction, so the 1-D banding error is strictly along the phase direction. This simplified the estimation of the banding error. We use a stochastic signal processing method for the banding error estimation which will be illustrated in the following sections.

4.2 Mathematical Model of Projector Space De-banding Algorithm (PSDb)

The mathematical model Projector Space De-banding algorithm is defined and demonstrated for better understanding the algorithm. Our Projector Space De-banding algorithm is an automated banding error correction algorithm using mapping of the captured image to projector space to align the bands to the projector rows and thereby simplify and improve the banding error estimation.

4.2.1 Mapping to Projector Space

The first step is to map the phase images recovered by the Modified Composite Pattern and the 2nd sinusoidal pattern to the projector space. Given the unwrapped phase image, $Y_{pc}(x, y)$ and the wrapped phase image, $Y_{wc}(x, y)$, the Y_{pc} and Y_{wc} elements are between 0 to 2π radians. We now assume the number of rows in the Projector Space (PS) is M_p , so the mapping scale factor between radians and projector row is

$$\alpha_{PS} = \frac{M_p - 1}{2\pi} \quad (4.1)$$

Banding geometry corresponds to the projector space geometry. By mapping data from camera space (x, y) to partial projector space (x, y_{pp}) the depth distortion of the reflected banding is removed and all bands are aligned with the projector rows. We keep the x_p coordinate of the projector space image as the coordinate of the phase image in camera space, such that $\underline{Y}_{pp}(x, y_p)$ is the phase image in projector space. The y_{pp} is the y coordinate in projector space, it is calculated as

$$y_{pp}(x, y) = \alpha_{PS} \cdot Y_{pc}(x, y), \quad (4.2)$$

$$y_p = \text{round}\left(y_{pp}(x, y)\right), \quad (4.3)$$

The value in the image $y_{pp}(x, y)$ is the y_p coordinate for each point in unwrapped phase image $Y_{pc}(x, y)$. Now, the mapping function is denoted as $MAP_{cp}\{\cdot\}$.

Fig. 4.1 shows an example of mapping a camera space image to projector space. We can see that although the snakes are distorted by the surface in the camera space image, however, when we map it to projector space, all the snakes are aligned from left to right in the projector space. Note that we have some holes (black dots) in the projector space image. This is because the mapping between camera space and projector space is subject to spatial quantization resulting in “pin hole”.



Figure 4.1 Mapping a camera space image (left) to a projector space image (right).

Fig. 4.1 shows a demonstration of the PSDb mapping. In projector space, we only map the MCP phase result.

4.2.2 Calculate the Differential of the Banding Error

We treat the banding error as a 1D signal, and the surface albedo variation as a noise

signal added to the banding we are trying to estimate. So to estimate and recover the banding error along the phase direction in the projector space image we formulate the problem as a standard additive noise problem. Also mentioned in the algorithm introduction, we utilize the Modified Composite Pattern recovered phase image to map the baseline phase image to projector space. However, this phase image contains a linear ramp that is recovered by mapping the differential phase images to the projector space.

The differential of the phase image in projector space is approximated as a difference equation such that

$$\Delta Y_{pc}(x, y_p) = MAP_{cp}\{Y_{pc}(x, y) - Y_{pc}(x, y - 1)\}, \quad (4.4)$$

where $Y_{pc}(x, y)$ is the unwrapped phase image from 2nd pattern.

Note that the phase image now has banding error, so the phase image could be represented as the summation of the ideal phase, $Y_{pa}(x, y)$, and the banding error image, $\theta(x, y)$ such that

$$Y_{pp}(x, y_p) = Y_{pa}(x, y) + \theta_e(x, y), \quad (4.5)$$

So, $\Delta Y_{pc}(x, y_{pp})$ is rewritten as

$$\Delta Y_{pc}(x, y_p) = \Delta Y_{pa}(x, y_p) + \Delta \theta_e(x, y_p), \quad (4.6)$$

where,

$$\Delta Y_{pa}(x, y_p) = MAP_{cp}\{Y_{pa}(x, y) - Y_{pa}(x, y - 1)\}, \quad (4.7)$$

$$\Delta \theta_e(y_p) = MAP_{cp}\{\theta_e(x, y) - \theta_e(x, y - 1)\}, \quad (4.8)$$

In Eq. (4.5) to Eq. (4.7) we represent the banding error as a 2-D image $\theta(x, y)$. As illustrate above, we treat the banding error as a 1-D signal. So each column (along the phase direction) in the 2-D banding error image $\theta(x, y)$ is a banding error signal. In Eq. (4.7), after mapping, although the mapped result is still a 2-D image, we represent it as a 1-D signal since all the columns in the banding error image are the same 1-D banding

error signal, which means we assume $\Delta\theta_e(y_p)$ is only a function of projector row coordinate y_p .

As shown in Fig. 4.1, the pin holes in the projector space image cause problems in banding error estimation, since those black holes are like adding more noise into the projector space image. In our research, we use linear interpolation to fill in the holes in projector space image. The 1-D linear interpolation method is utilized along the phase direction to interpolate the projector space image. Fig. 4.2 shows the final result of the differential of the phase image mapped in the projector space with holes interpolated.



Figure 4.2 Projector Space differential of the phase image with interpolation

As we can see from Fig. 4.2 of the differential of phase image, the DC component is removed.

We assume the object surface is complicated and each column of $\Delta Y_{pc}(x, y_p)$ can be modeled as an ergodic random process with mean, $\mu_a(y_p)$. So the expected value is calculated for each row as

$$\mu_{\Delta}(y_p) = E\{\Delta Y_{pc}(x, y_p)|y_p\} \approx \frac{1}{N_x} \sum_{n=1}^{N_x} \Delta Y_{pc}(x_n, y_p), \quad (4.9)$$

Where $\mu_{\Delta}(y_p)$ is a 1-D vector sequence containing the expected value of each row of the $\Delta Y_{pc}(x, y_p)$ and N_x is the number of columns of $\Delta Y_{pc}(x, y_p)$.

Fig. 4.3 shows the estimate expectation of differential phase image, which is $\mu_{\Delta}(y_p)$ in Eq. (4.9). Note that from row 2500 to 2700, there is a phase jump in the phase image, which results in a sharp drop in the differential of phase image.

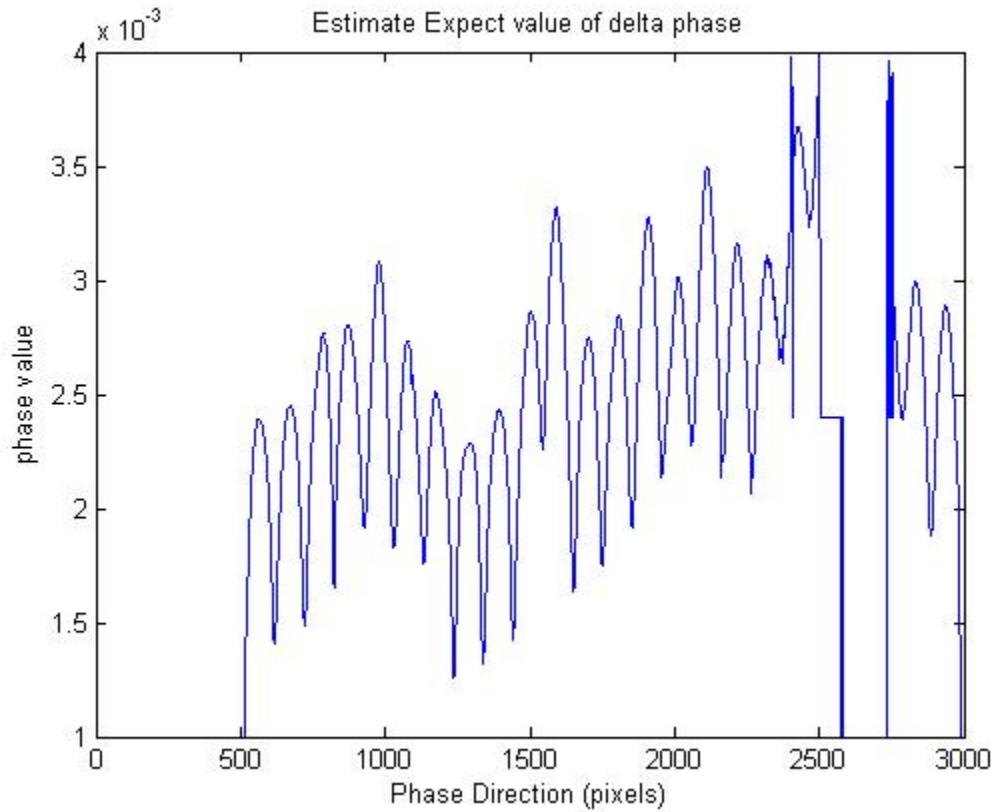


Figure 4.3 Estimate Expectation of differential phase image

From Fig. 4.3, we know that the high frequency component is caused by banding error and the low frequency component is the result of the differential of the phase ramp. Since

in Fig. 3.13, the baseline phase ramp is a low frequency signal. The expectation of differential phase image also supports our assumption that the banding error is a 1-D signal along the phase direction in the projector space, otherwise $\mu_{\Delta}(y_p)$ in Fig. 4.3 will be corrupted by the averaging operation in the Eq. (4.9), since we have nearly 3000 columns with banding error in the phase image.

Then, $\mu_{\Delta}(y_p)$ is numerically integrated to get $Y_{pp,I}(y_p)$ which contains the expected value of the actual phase $Y_{pp,a}(y_p)$ and the banding error $\theta_e(y_p)$ such that

$$Y_{pp,I}(y_p) = \sum_{m=1}^{y_p} \mu_{\Delta}(m) = Y_{pp,a}(y_p) + \theta_e(y_p), \quad (4.10)$$

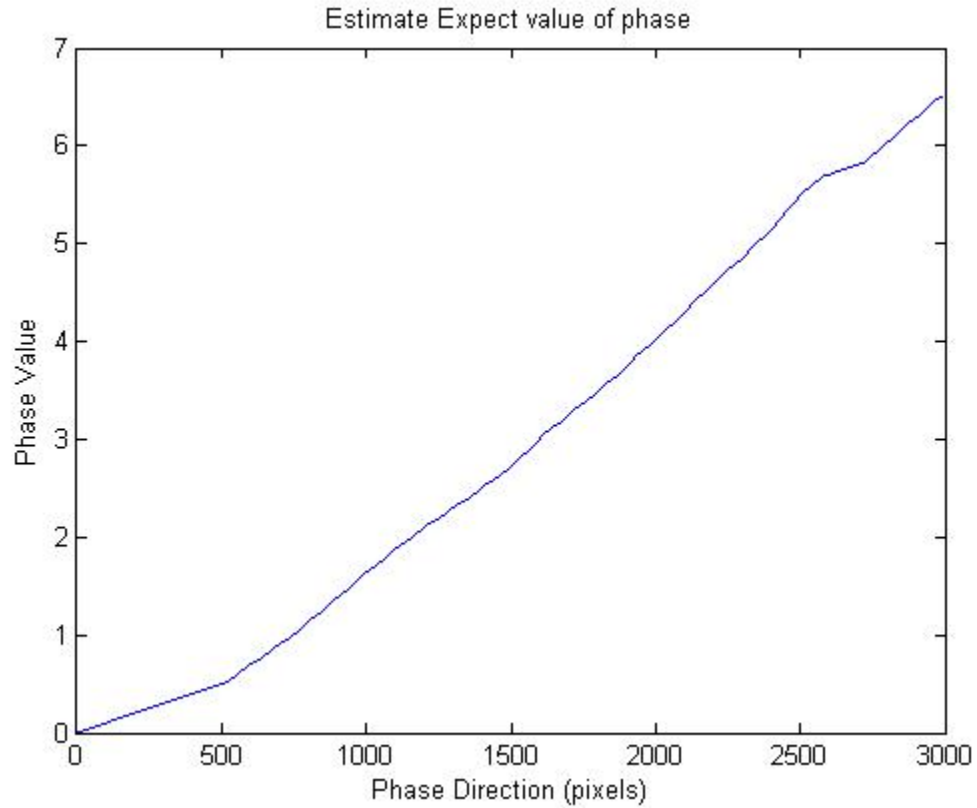


Figure 4.4 Estimated Expectation of Phase Value

The result of Eq. (4.10) is shown in Fig. 4.4. The phase banding error is difficult to observe along with the phase ramp, so that is why we use differential for the phase image.

4.2.3 Estimate Banding Error

In section 4.2.2, we estimate the expectation of the phase with banding error, and in this section we need to recover the banding error from it. From Eq. (4.10) we know that, the way to estimate the banding error is to subtract the actual phase ramp (ideal phase ramp without noise and banding error) from the estimated expectation. The actual phase ramp $Y_{pp,a}(y_p)$ is between 0 to 2π radians, so we need to estimate it and subtract it from the $Y_{pp,l}(y_p)$ to get the banding error.

To approximately calculate the actual phase ramp $Y_{pp,a}(y_p)$, we proposed to utilize the branch cut locations in the wrapped phase image recovered by Quadrature Phase Processing technique to fit a line between each branch cut point locations to estimate the actual phase. Also, since we have phase ramp from Modified Composite Pattern, we combine the two results together to get a better estimation.

We first illustrate the reason to use branch cuts points as baseline points for estimating the actual phase ramp. As shown in Fig. 3.11, the phase image is wrapped after Quadrature Phase Processing, which means the phase value along the phase direction is cyclic from 0 to 2π radians, and the period of the cycle corresponds to the period of the sinusoidal pattern. So, there are phase jumps between each two cycles that the phase value drops from 2π radians to 0 sharply. We call the phase jump in the wrapped phase image as branch cut.

Because the banding error is caused by the deterministic distortion of the digital projected sinusoidal pattern, so for each cycle of the sinusoidal pattern, the banding error is the same, which means banding error is cyclic with period of the highest frequency unwrapped phase result. In this way, the banding error ideally is the same within each of two branch cuts. So after unwrapping process, we are able to use the branch cut locations in the wrapped phase to fit a line between each of two of the branch cuts locations to approximate the actual phase ramp $Y_{pp,a}(y_p)$. The estimated $Y_{pp,a}(y_p)$ through line fitting is composed by several line segments, and between each two branch cuts locations, the phase is a linear ramp.

To get the branch cut points, we use the wrapped phase image shown Fig. 3.11, and calculate the differential along the phase image of the wrapped phase image. The reason to do differential along the phase image is to detect the phase jump.

$$\Delta Y_{wp}(x, y_p) = MAP_{cp}\{Y_{wc}(x, y) - Y_{wc}(x, y - 1)\}, \quad (4.11)$$

As illustrated in Eq. (4.11), $Y_{wc}(x, y)$ is the wrapped phase image in camera space, and the differential along the phase direction (y direction of the image) is calculated and then map to projector space through the same mapping factor $MAP_{cp}\{\cdot\}$. The result differentiated wrapped phase image $\Delta Y_{wp}(x, y_p)$ is shown in Fig. 4.5.

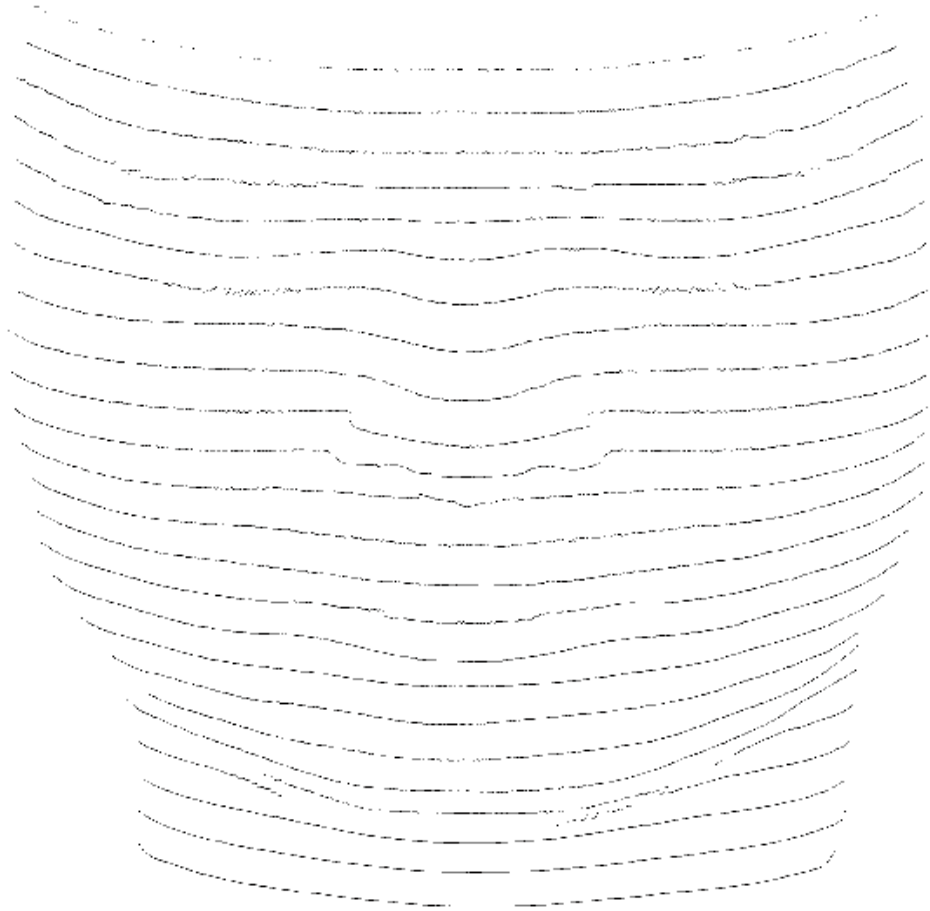


Figure 4.5 Differential wrapped phase image in camera space

Fig. 4.5 clearly shows the branch cuts locations in the image, highlighted in black. Then,

we identify those branch cuts by using a threshold T_{BC} as in

$$B_{BC}(x, y_p) = \begin{cases} 1, \Delta Y_{wp}(x, y_p) \geq T_{BC} \\ 0, \Delta Y_{wp}(x, y_p) < T_{BC} \end{cases}, \quad (4.12)$$

where $B_{BC}(x, y_p)$ is a 2-D branch cut image which is an binary image that stores the branch cuts locations. In the $B_{BC}(x, y_p)$, the branch cuts locations have value 1 and all the other has value 0. An example of 2-D branch cut image is shown in Fig. 4.6. Note that, in Fig. 4.6, most of the noise in Fig. 4.5 is filtered out through the threshold T_{BC} . In our research to filter out the noise robustly and keep the correct branch cuts locations, we use value 1.8π for threshold T_{BC} . This value is acquired by trial and error experiments.



Figure 4.6 Branch Cuts image in projector space

Although using T_{BC} as a global threshold can reject most of white noise in the branch cuts image $B_{BC}(x, y_p)$, however, due to the snakes' distortion in the camera space image and the non-bijection mapping factor $MAP_{cp}\{\cdot\}$, one horizontal branch cut is not a straight line locates in one row in the branch cuts image. As shown in Fig. 4.7 when we zoom in the branch cuts image, we see the branch cut is not strictly horizontal along the x direction.

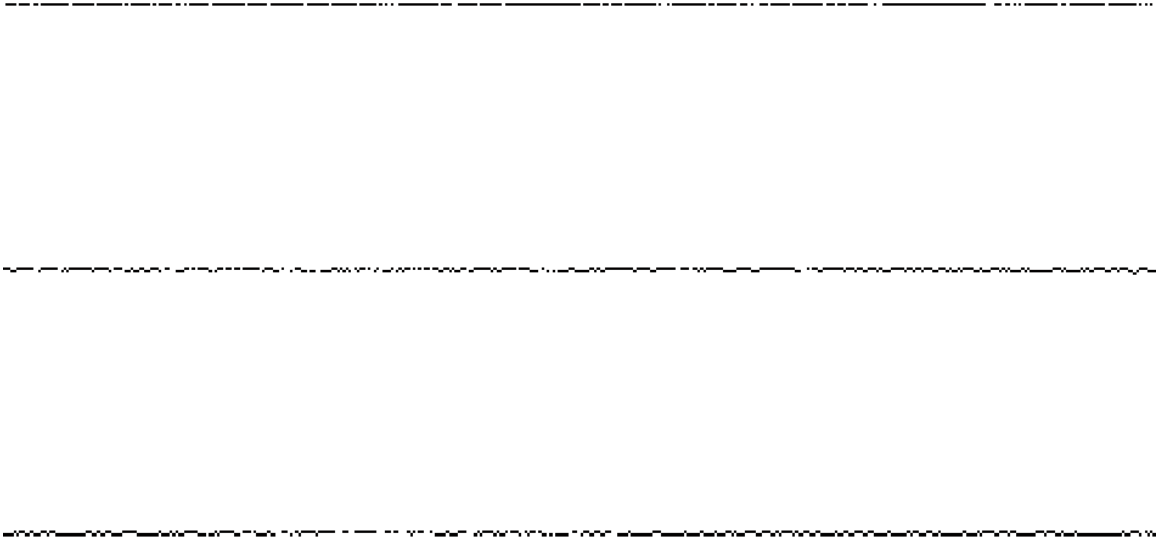


Figure 4.7 Zoomed in branch cuts image

So in order to estimate the branch cut locations, we utilize a histogram to estimate the branch cut locations for the 1-D phase ramp with banding error $Y_{pp,l}(y_p)$ in Eq. (4.10). We count the number of branch cuts points (number of ones) for each row of $B_{BC}(x, y_p)$ to get a 1D histogram vector as represented by

$$H_{BC}(y_p) = \text{Histogram}(B_{BC}(x, y_p)), \quad (4.13)$$

where $H_{BC}(y_p)$ is the 1-D histogram along the phase direction of $B_{BC}(x, y_p)$. Then another threshold T_p is set to decide the branch cuts points along the phase direction. The final result of branch cuts detection in projector space is shown in Fig. 4.8. In Fig. 4.8, the row which has a blue line means this row has a branch cut in it.

After we detect all the branch cuts in projector space, we need to store the phase value at the branch cuts locations for the interpolation, as expressed in Eq. (4.14).

$$Y_{BCI}(y_p) = \begin{cases} Y_{pp,l}(y_p), & \text{for } H_{BC}(y_p) \geq T_p \\ 0, & \text{for } H_{BC}(y_p) < T_p \end{cases}, \quad (4.14)$$

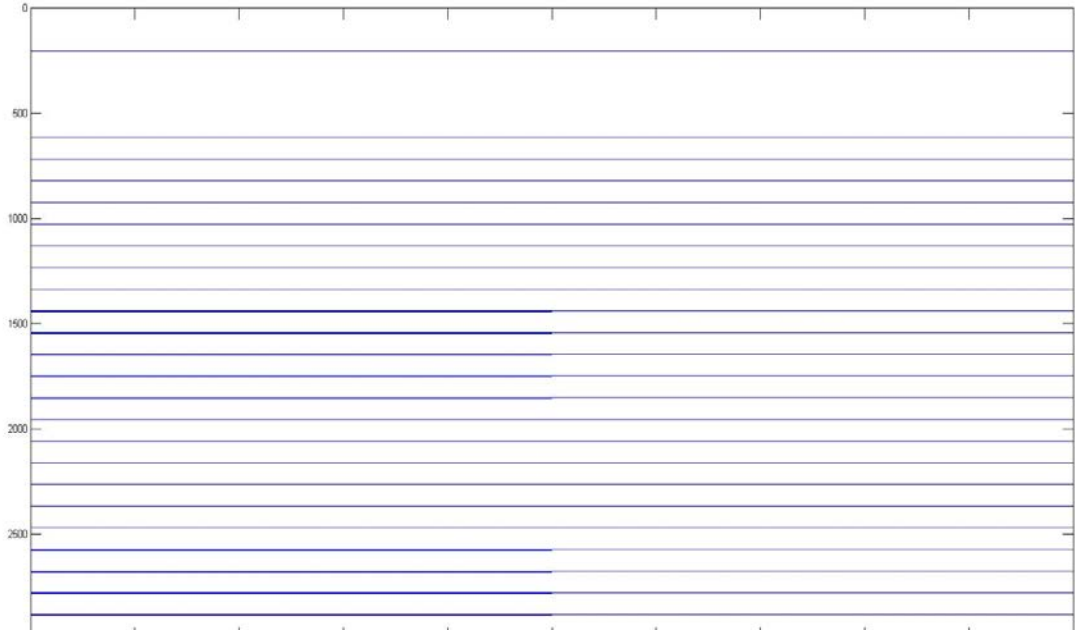


Figure 4.8 Image indicates the rows have branch cuts in projector space

In Eq. (4.14), the $Y_{BCI}(y_p)$ is a 1-D vector with length same as the number of rows in the phase image. So in $Y_{BCI}(y_p)$, only the branch cut locations have phase value, other points are zero. For efficiently, we use a vector that only stores the phase value of the branch cuts points as represented by

$$Y_{BConly}(n_{BC}) = Y_{BCI}(y_p) \text{ for } H_{BC}(y_p) \geq T_p, \quad (4.15)$$

The vector element $Y_{BConly}(n_{BC})$ contains only values of phase at branch cuts locations, $n_{BC} = 1, 2, \dots, M_{BC}$. Where M_{BC} is the number of branch cuts. Also, we need another vector stores the row index for the branch cuts locations as expressed in by

$$y_{p,BConly}(n_{BC}) = y_p \text{ for } H_{BC}(y_p) \geq T_p, \quad (4.16)$$

where $y_{p,BConly}(n_{BC})$ is the projector space row index only at BC locations. We use $y_{p,BConly}(n_{BC})$ and $Y_{BConly}(n_{BC})$ to fit line segments between every two adjacent branch points such that the interpolation values are

$$a_y(n) = \frac{Y_{BConly}(n+1) - Y_{BConly}(n)}{y_{p,BConly}(n+1) - y_{p,BConly}(n)}, \quad (4.17)$$

$$b_y(n) = Y_{BConly}(n) - a_y(n) \cdot y_{p,BConly}(n) \quad (4.18)$$

where $a_y(n)$ is the slope for the n th line segment, and $b_y(n)$ is the intercept. The interpolated phase acts as a reference phase

$$Y_{ref}(n) = a_y(n)y_p + b_y(n) \quad (4.19)$$

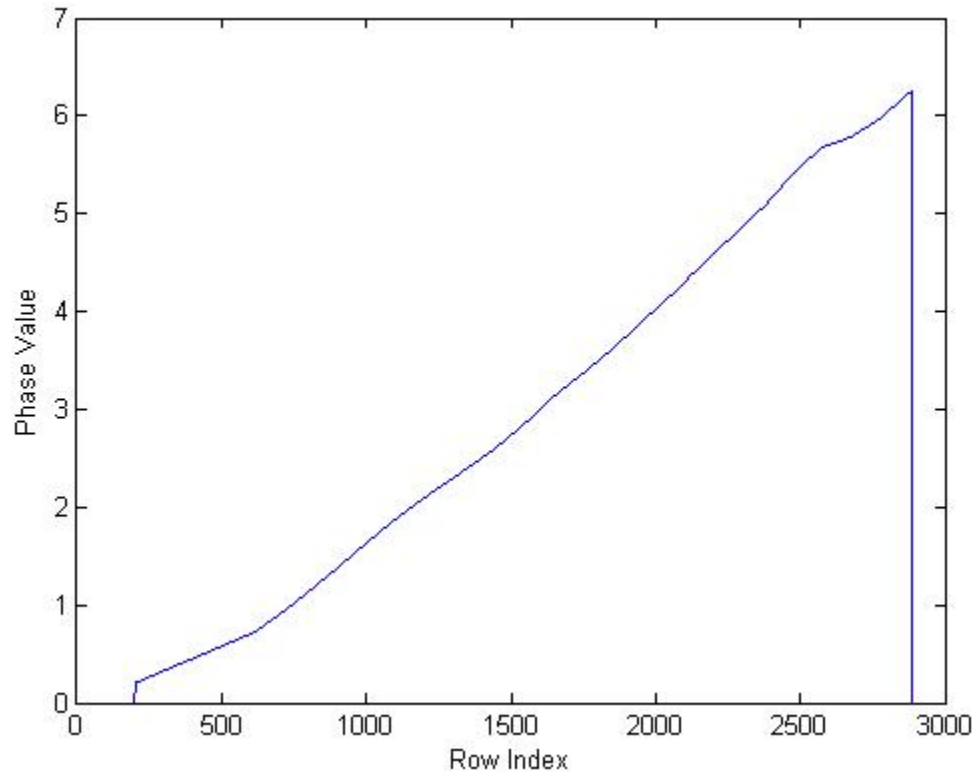


Figure 4.9 Interpolated reference phase ramp

Fig. 4.9 shows the result of interpolation. This reference phase ramp $Y_{ref}(n)$ is the estimation of the actual phase ramp in Eq. (4.10). And compared with Fig. 4.4, we can

see the estimated phase ramp is a good approximation to the actual phase ramp without banding error.

Based on Eq. (4.10) and Eq. (4.19), the banding error is estimated as the following equations:

$$\begin{aligned} \bar{\theta}(y_p) &= Y_{pp,I}(y_p) - Y_{ref}(y_p) = Y_{pp,I}(y_p) - (a_{yn} \cdot y_p + b_{yn}), \\ \text{for } x_n \leq y_p < x_{n+1} \end{aligned} \quad (4.20)$$

where the $\bar{\theta}(y_p)$ is the 1-D estimated banding error.

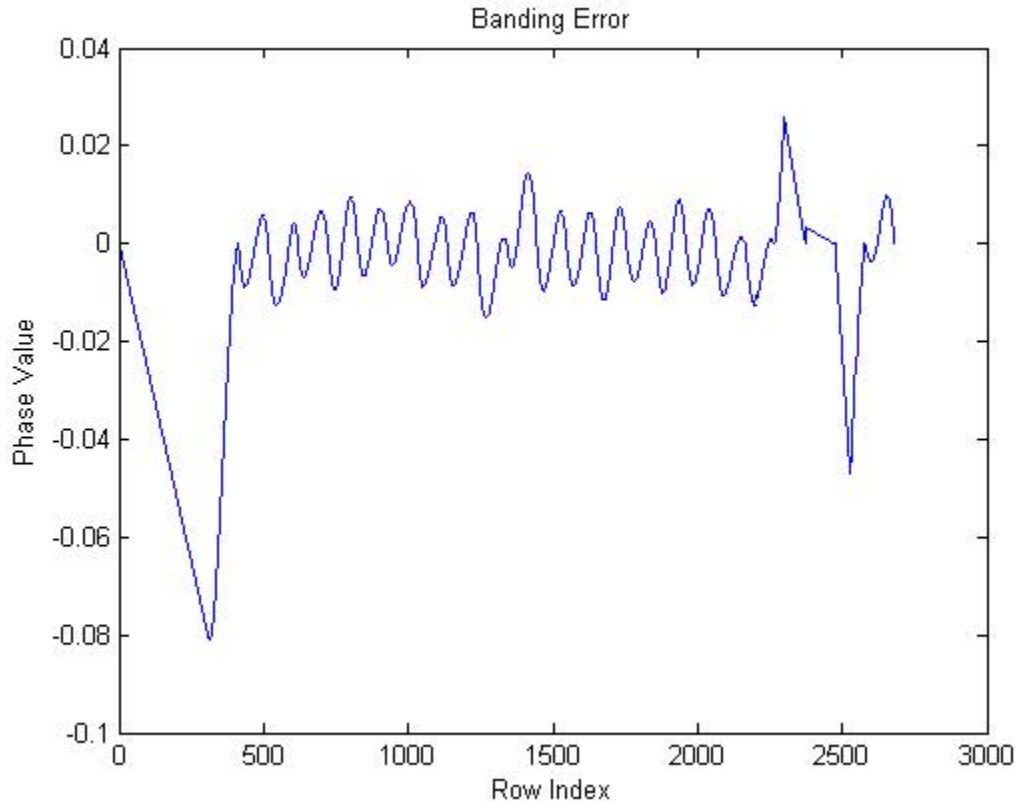


Figure 4.10 Estimated Banding Error

Fig. 4.10 shows the estimated banding error $\bar{\theta}(y_p)$. Note that the big jump at the beginning and end of the banding error vector is caused by the phase jump between the background and the object surface's phase, so the real banding error lies in the middle part of the plot in Fig. 4.10. From Fig. 4.10 we know that the range of the banding error,

that is the peak to peak phase value, is within ± 0.02 radian.

The final step is to correct the phase image based on estimated banding error. The procedure is map each point in $Y_p(x_c, y_c)$ to projector space to check the banding error of that point such as $\bar{\theta}(y_p)$, then we subtract the banding error out for this given point as

$$Y_{pc,D}(x, y) = Y_{pc}(x, y) - \bar{\theta}(y_p), \quad (4.21)$$

The de-band phase image is shown in Fig. 4.11. Although we cannot see much difference in the phase image compared with the previous phase image with the banding error, but the 3D reconstructed result has significantly less banding error which will be demonstrated in the following sections.

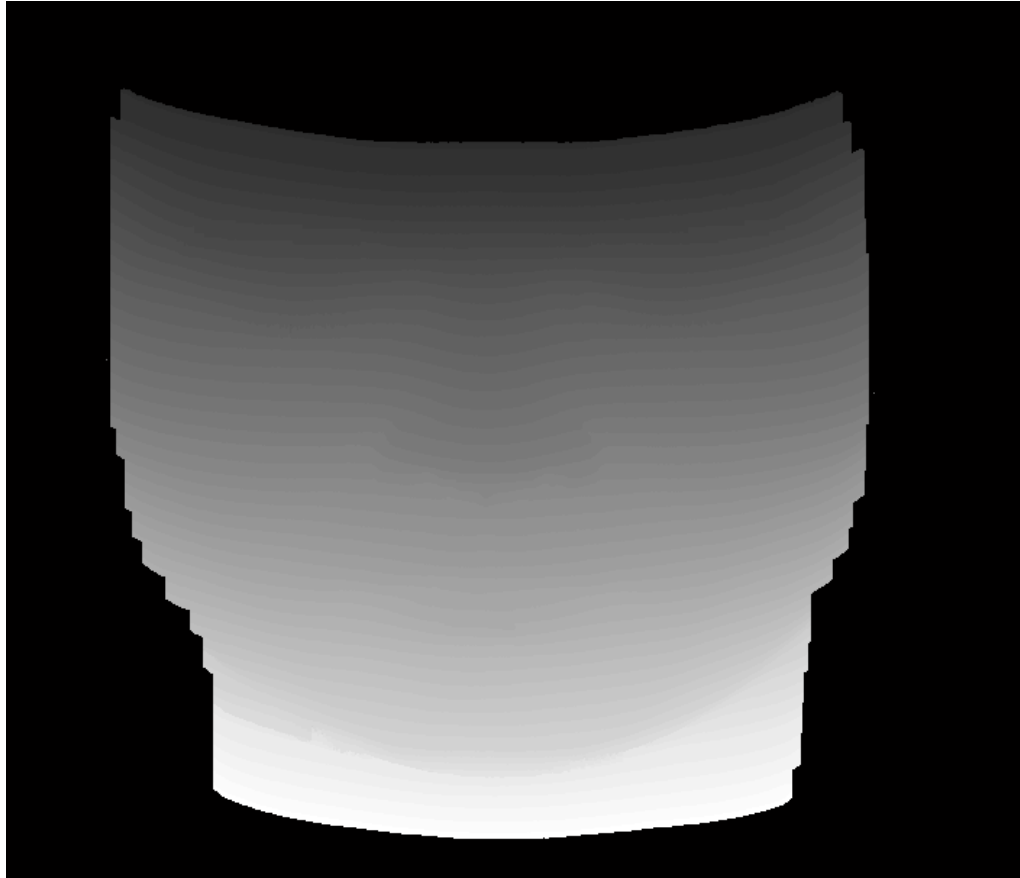


Figure 4.11 De-band Phase Image

4.3 Notations for Mathematical Model of De-Banding Algorithm

We summarize all the equations and notation used in the previous sections for a better understanding of our mathematical model of De-Banding algorithm. We separate all the equations into three categories: (1) Camera Space Notations and processing equations; (2) Projector Space Notations, Equations and processing techniques; (3) 1-D Banding Error estimation statistics.

Table 4-1 Notations for Math Model of PSDB

Notation	Meaning
CAMERA SPACE	
$\{x_c, y_c\}$	Camera Space Coordinates
$Y_{wc}(x_c, y_c)$	wrapped phase image in Camera Space
$Y_{pc}(x_c, y_c)$	unwrapped phase image in Camera Space
$Y_{pa}(x_c, y_c)$	Phase Image without banding error
$\theta_e(x_c, y_c)$	banding error in camera space
$Y_{pc,D}(x_c, y_c)$	De-banded phase image in camera space
PROJECTOR SPACE	
$\{x_c, y_p\}$	Partial Projector Space Coordinates
M_p	Number of rows in projector space
α_{PS}	scale factor between radians and projector row
$y_{pp}(x_c, y_c) = \alpha_{PS} \times Y_{pc}(x_c, y_c)$	Fractional projector row coordinate

	matrix
$y_p = \text{round}(y_{pp}(x_c, y_c))$	Integer projector row value
$Y_{wp}(x_c, y_p)$	Wrapped phase image in projector space
$Y_{pp}(x_c, y_p) = y_{pp}(x_c, y_c)$	Unwrapped phase image in projector space
PROJECTOR SPACE DIFFERENTIALS	
$\Delta Y_{pa}(x_c, y_p) = \text{MAP}_{cp}\{Y_{pa}(x_c, y_c) - Y_{pa}(x_c, y_c - 1)\}$	Phase difference image without banding error
$\Delta \theta_e(x_c, y_p) = \text{MAP}_{cp}\{\theta_e(x_c, y_c) - \theta_e(x_c, y_c - 1)\}$	Phase Banding Error Difference image
$\Delta Y_{pp}(x_c, y_p) = \Delta Y_{pa}(x_c, y_p) + \Delta \theta_e(x_c, y_p)$	Phase difference image including band error
$\Delta Y_{wp}(x_c, y_p) = \text{MAP}_{cp}\{Y_{wc}(x_c, y_c) - Y_{wc}(x_c, y_c - 1)\}$	Wrapped Phase difference image
T_{BC}	Threshold set to detect Branch Cuts points
$B_{BC}(x_c, y_p)$	Binary Branch Cut Indicator Image
1-D BANDING STATISTICS	
$\mu_\Delta(y_p) = E\{\Delta Y_{pp}(x_c, y_p) y_p\}$	Average Phase Difference image

$Y_{pp,I}(y_p)$	Average phase ramp
$Y_{pp,a}(y_p)$	actual phase ramp needs to be estimated
$\theta_e(y_p) = \theta_e(x_c, y_p)$	Banding phase error is not a function of x_c
$Y_{pp,I}(y_p) = \sum_{m=1}^{y_p} \mu_{\Delta}(m)$ $= Y_{pp,a}(y_p) + \theta_e(y_p)$	Numerical integration of Average Phase Difference
$H_{BC}(y_p) = \text{Histogram}(B_{BC}(x_c, y_p))$	Histogram of Binary Branch Cut Indicator Image
T_p	Threshold set to decide valid branch cuts
$Y_{BCI}(y_p) = \begin{cases} Y_{pp,I}(y_p) & \text{for } H_{BC}(y_p) \geq T_p \\ 0 & \text{for } H_{BC}(y_p) < T_p \end{cases}$	Values of Average Phase at BC locations
$Y_{BConly}(n_{BC}) = Y_{BCI}(y_p) \text{ for } H_{BC}(y_p) \geq T_p$	Values of Average Phase only at BC locations, $n_{BC}=1,2, \dots, M_{BC}$
M_{BC}	Number of branch cuts
$y_{p,BConly}(n_{BC}) = y_p \text{ for } H_{BC}(y_p) \geq T_p$	Projector space row indices only at BC locations
$a_y(n) = \frac{(y_{p,BConly}(n+1) - y_{p,BConly}(n))}{(Y_{BConly}(n+1) - Y_{BConly}(n))}$	Slope between BCs n and $n+1$ where $n=1,2,\dots,(M_{BC}-1)$
$b_y(n) = Y_{BConly}(n) - a_y(n) y_{p,BConly}(n)$	Intercept between BCs n and $n+1$
$Y_{ref}(n) = a_y(n) y_p + b_y(n)$	Reference angle between BCs
$\bar{\theta}(y_p) = Y_{pp,I}(y_p) - Y_{ref}(y_p)$	Estimated banding error projector space

4.4 Experimental Results of PSDb Algorithm

We present the experimental results of the PSDb algorithm. We still use the same system set-up as Two-Pattern Full Lateral Resolution SLI system as shown in Fig. 3.16. Note that although we use our Two-Pattern system to do the experiments, the PSDb algorithm is applicable to the phase image recovered by any SLI System.

A baseline object for testing the PSDb algorithm is a flat surface as shown in Fig. 4.12. The flat board in Fig. 4.12 is a piece of flat wood with 18cm by 18 cm size.

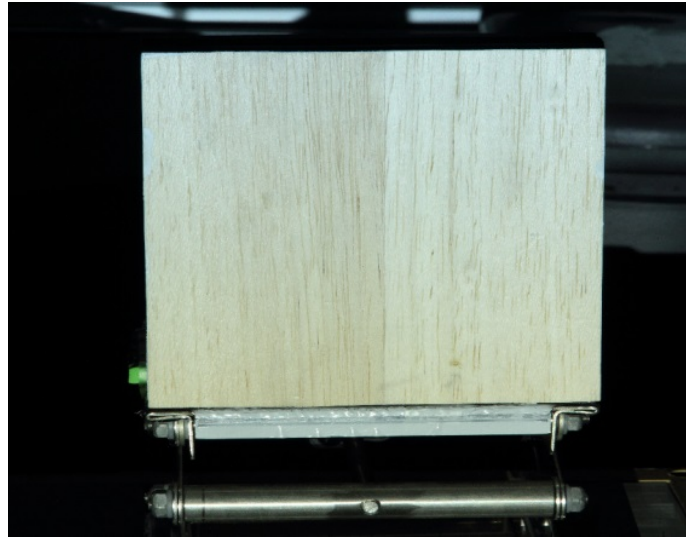


Figure 4.12 A Baseline Flat Board to test thePSDbAlgorithm

The 3-D reconstructed surface is shown in Fig. 4.13. The rotated view in Fig. 4.13 right demonstrates the banding error on the 3-D surface. To demonstrate the banding, in Fig. 4.14 left, the side view of the reconstructed 3-D surface of the flat board is displayed where the flat board 3-D reconstruction has a significant banding error. The measured average peak to peak value of the banding error is 2.058mm.

We apply the PSDb algorithm to de-band the recovered phase image from Quadrature Phase Processing method. The result of PSDb is shown in Fig. 4.14 right.



Figure 4.13 Reconstructed 3-D surface, front view (left) and rotated view (right)

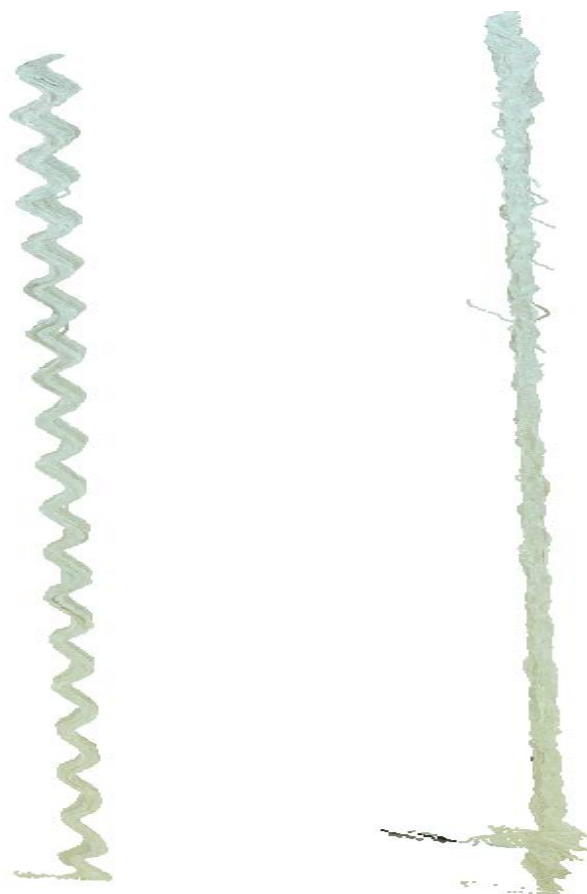


Figure 4.14 Side view of the reconstructed 3-D surface of the flat board: Surface with Banding error (left), De-Band Result (Right)

From the comparison of the surface with banding with the De-Banded result in Fig. 4.14, we can see the huge improvement in the 3-D surface reconstruction with the De-Banding algorithm. The measured average peak to peak value of the banding error is 0.07mm, which is 30 times less banding error.

Second experimented result is shown in Fig. 4.15, where a human face 3-D scanned by the Two-Pattern SLI system with our PSDb algorithm applied. The original surface with banding distortion is shown Fig. 3.22.

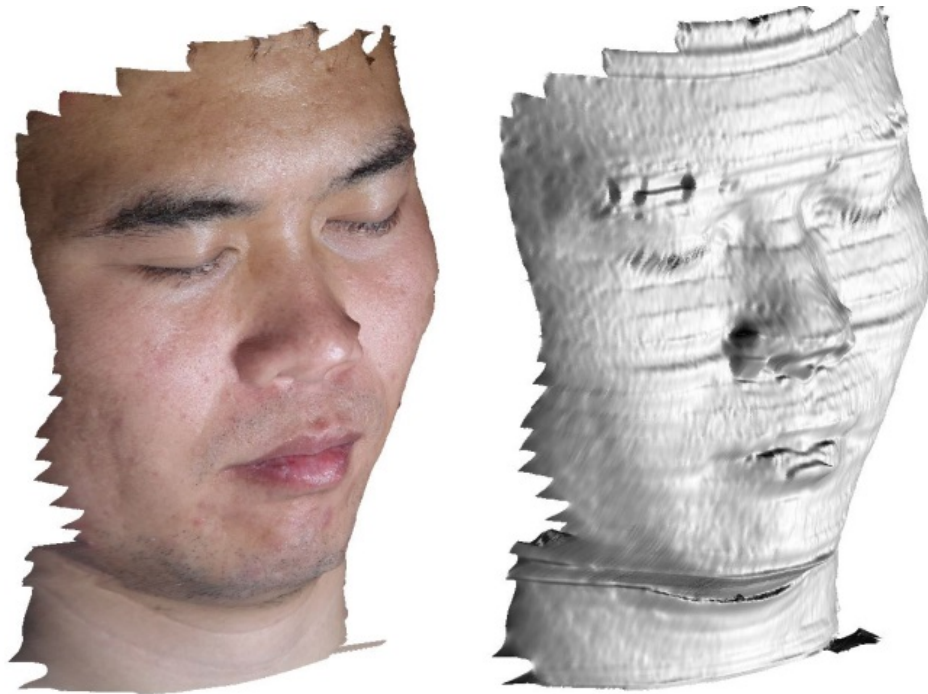


Figure 4.15 Human Face Scan. Left One is with texture, right one is metallic 3D surface

The improvement about banding error attenuation in human face scan experiment is $23\times$ better. As we know, for human face 3-D surface reconstruction, the nose area and the eyebrow area are both very hard to reconstruct accurately due to the albedo and depth jumps. In our PSDb algorithm we need to estimate the ergodic mean, so the big phase jump around the nose area affects the expectation value of the differentiated phase. These factors deteriorate the performance of PSDb algorithm for complicate surface reconstruction.

The table below lists the comparison between our algorithm and some other De-banding methods.

Table 4-2 Comparison between Different De-Banding techniques

De-Banding Method	Improvement	Require Pre-Calibration for Banding Error of Scanning System?
's Gamma Model for Gamma Calibration	33×	Yes
Active Gamma Correction Model	12.6×	No
Projector Space De-Banding Method	23× (Complicated Surface) 30×(Smooth Surface)	No

Compared with gamma correction type banding error correction algorithms in table 4-1, the PSDb is better than active gamma correction and comparable to Kai's gamma model. However, the PSDb does not require a pre-calibration. For other active De-banding algorithm, such as active gamma correction model proposed by Zhang, etal, our algorithm's performance is much better and is able to handle the complicate surface de-banding tasks, which is a significant improvement in active de-banding technology. It should also be noted that the PSDb is a post-processing algorithm so it can be used in conjunction with pre-calibration algorithm for additional performance.

4.5 Depth Modulation Transfer Function Performance Characterization for SLI system

After the development of our Two-pattern Full Lateral Resolution SLI depth measuring system and Projector Space De-Banding algorithm, we proposed a performance characterization method for performance measurement of SLI system. There are numerous techniques of 3-D reconstruction or depth measuring based on SLI system, however, there is not a very standard performance testing or characterization for SLI system. So in this section, we proposed a method for SLI system performance testing

based on the concept of the Matched Transfer Function (MTF).

The performance of the two-pattern method is demonstrated and quantified by performance measurements. For a SLI sensor, the lateral units of an SLI scan are in world coordinates $\{x_w, y_w, z_w\}$ in units of millimeters. We calculate the Matched Transfer Function in terms of “Depth”, which is called DMTF here. Analogy to the CTF of a 2D grayscale intensity image, we use depth here in place of intensity to calculate the DMTF, which shows the performance of the 3D SLI scanner [20].

4.5.1 Background of DMTF and Rotation Stage Experiment

The original MTF math model for a 2D image is based on the modulation index as

$$ModulationIndex = \frac{max-min}{max+min} \quad (4.22)$$

Where max the maximum value of the intensity and min is the minimum value of the intensity. So, MTF is calculated by computing the ratio between other frequency’s Modulation Index and the DC component’s Modulation Index. However, depth does not work in this way since the DC component of depth is not a constant value and it converges to the average height of the surface which is preset. Thus, definition of the performance measures that is independent of surface cross-section is needed. As presented by Hassebrook [23], representing a surface cross-section as a set of Fourier Components allows to access the different components separately in order to obtain DMTF measures. In this section, we use 6 sinusoidal wave grids as Fourier Components to compute the DMTF for the two-pattern scanner. Then, we measure the average Peak to Peak value in the 3D reconstructed surface, and divided by the real Peak to Peak value to get the modulation index value, and then normalize them to plot DMTF.

Based on the idea of the DMTF and Fourier Transform, we want to test the DMTF response of the 3D scanner on several directions. So we rotate the sinusoidal grid on x-y plane to get different DMTF corresponding to different angles.

4.5.2 Experiments Set up and Results

Fig. 4.16 shows the set of the sinusoidal grids (totally 6 grids) used in the experiments,

with spatial frequency from 0.0203 cy/mm to 0.32 cy/mm and peak to peak value from 10 mm to 1 mm. A rotation stage is set up to rotate the grid in x-y plane, so the average depth (z value) of the grid is not changed. Fig. 4.17 demonstrates how the rotation stage works. We mount a sinusoidal grid from the set onto the rotation stage, then we counter-clock-wise rotate the grid on the stage on the x-y plane from the 90 degree, which means the grid is vertical (the wave length direction of the grid is parallel to the x axis), to 0 degree. We record 4 positions of the grid on 90 degree, 60 degree, 30 degree and 0 degree.

The scanner apparatus is described in Chapter 3 section 2. A high-end with high definition camera is used here to capture the projected pattern. The system uses a Canon EOS-7D high definition camera with resolution 5184 x 3456 and a ViewSonic PJ260D digital projector with resolution 1024 x 768. The scanner is shown in Fig. 10 right.

The distance between the camera and the projector is 14 inches, and the object is 24 inches away from the projector lens.



Figure 4.16 Set of Sinusoidal Grid in the Experiment(left), scanner settings (right)

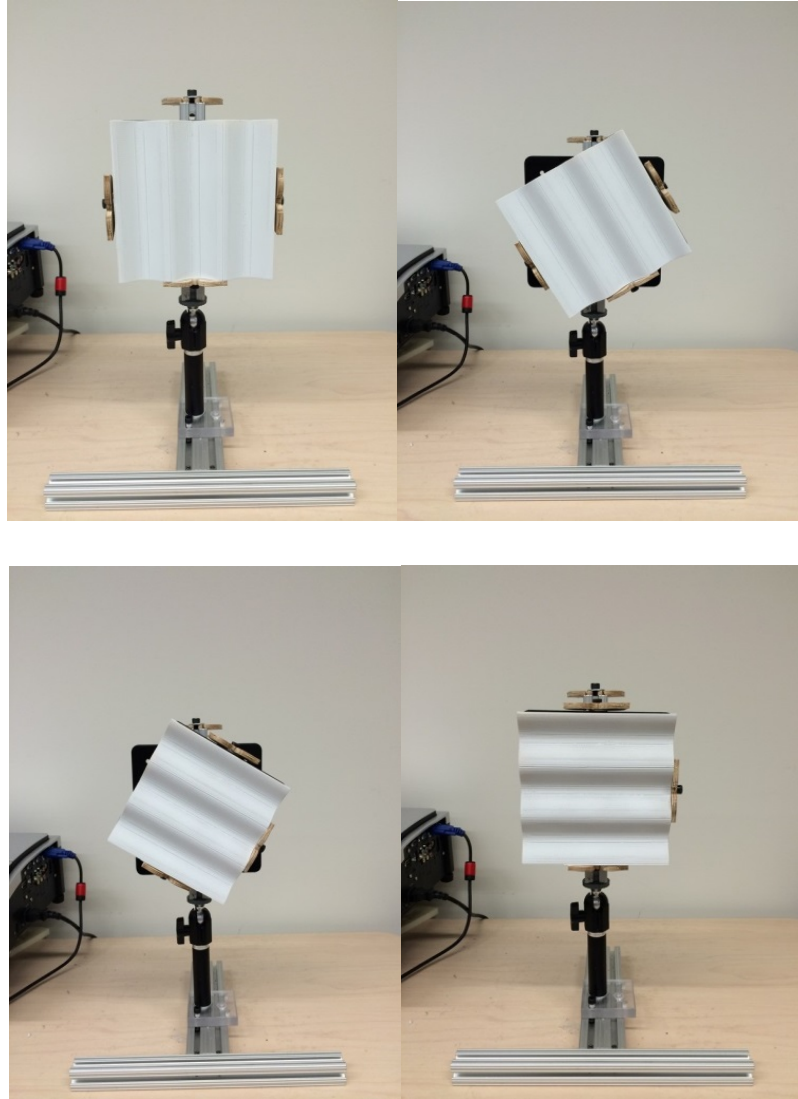


Figure 4.17 Sinusoidal Grid on the rotation stage, rotate the grid counter-clock-wisely from 90 degree (grid is vertical, top left), 60 degree (top right), 30 degree (bottom left) to 0 degree (grid is horizontal, bottom right).

The Sinusoidal Grid Rotation-Stage experiment procedure is described below:

- (1) Fix the rotation-stage to a certain angle, such as 90 degree.
- (2) Mount every grid onto the stage, and use the scanner and the software to reconstruct the 3D surface of the grid then calculate the peak to peak value of the sinusoidal surface.
- (3) Use the peak to peak values for each grid to calculate the DMTF for each angle and each frequency.

(4)Continue to rotate the stage. Repeat step 1, 2 and 3.

The result of the DMTF is shown in Fig. 4.18. Each point on the DMTF represents a ratio between peak to peak value of reconstructed 3D surface and peak to peak value of real grid at certain sinusoidal grid frequency (cy/mm).

As shown in Fig. 4.18, it shows our system achieves wide bandwidth performance when the rotation angle is 90 degree and 60 degree. Note that the peak to peak value of real grid is only 1 mm. Moreover, when the sine wave on the grid surface becomes parallel to the projected pattern, which is considered as a difficult task for SLI method, the system still performs well at lower frequency. We see a drop of performance from low frequency to high frequency and from 90 degree angle to 0 degree angle, which is our expectation of the performance of our scanner. The drop of the performance is caused by two aspects: 1) the spatial frequency of the board exceeds the spatial frequency of the projected sinusoidal pattern, this will cause the ambiguity problem; 2) the PSDb algorithm suppress the high frequency component along the phase direction.

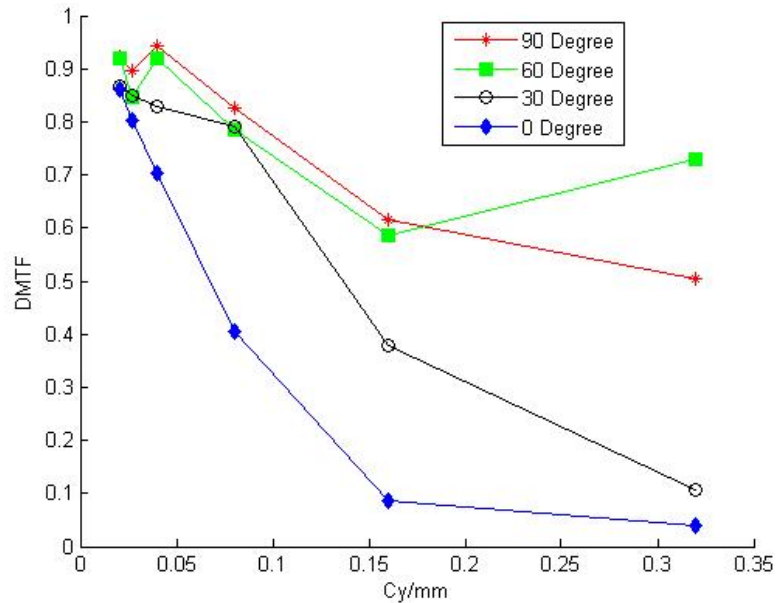


Figure 4.18 DMTF for 90 degree to 0 degree

Table 4-3 Depth measurement performance characterization for MCP only

Depth (cy/mm)	Frequency f_t	$Z_{p-p,t}$ (mm)	90 Degree $Z_{p-p,mcp}$ (mm)	0 Degree $Z_{p-p,mcp}$ (mm)
0.020=1/49.3		10	8.8	8.59
0.027=1/37.5		7.5	6.13	6.57
0.080=1/12.5		5.5	4.03	3.83
0.160=1/6.25		3	1.91	1.28
0.320=1/3.125		2	1.06	0.05

The sinusoidal target frequency f_t (cy/mm) as an inverse of spatial wavelength (mm/cy), accurate target peak-to-peak variation $z_{p-p,t}$ (mm), and MCP rendered peak-to-peak values, $z_{p-p,MCP}$ (mm), are shown in Table 4-2. The $z_{p-p,MCP}$ measurements were performed with the sinusoidal targets orientated both 90 degree and 0 degree. [10]

Table 4-4 Depth measurement performance characterization for 2PFLR

Depth (cy/mm)	Frequency f_t	$Z_{p-p,t}$ (mm)	90 Degree error ($Z_{p-p,2PFLR} - Z_{p-p,t}$) / $Z_{p-p,t}$	0 Degree error ($Z_{p-p,2PFLR} - Z_{p-p,t}$) / $Z_{p-p,t}$
0.020=1/49.3		10	7.80%	14.00%
0.027=1/37.5		7.5	10.38%	19.63%
0.080=1/12.5		5.5	27.20%	29.60%
0.160=1/6.25		3	38.33%	91.33%
0.320=1/3.125		2	49.70%	96.00%

Table 4-3 demonstrates the error measurement for 2PFLR using the developed performance characterization system.

4.6 Summary

In this chapter we illustrate our PSDb algorithm for Structured Light Illumination system. Our de-banding algorithm is based on the fundamental idea of estimation of the banding error in projector space. By mapping the phase image to projector space, all the snakes in the image are straight, which means for any one row in the image, the banding error stays the same for each column. In this way, we treat each column of phase image in projector space as a 1-D stochastic signal and by the stochastic processing described in section 4.2,

we are able to estimate the 1-D banding error. We propose a novel method to estimate the actual phase ramp without banding error based on the interpolation between each two branch cuts points. The branch cuts points are detect directly from the wrapped phase image or in our Two-Pattern Full Lateral Resolution SLI depth measuring system, the snakes' peaks detected in Modified Composite Pattern is able to be utilized to do branch cuts location estimation. Then, after we estimate the actual phase ramp, we is able to calculate the banding error by subtract the actual phase ramp out from the 1-D phase ramp with the banding error. We then correct each point in the phase image in the camera space based on this estimated 1-D banding error. Our de-banding algorithm is able to de-band the 3D reconstruction of any of the Structured Light Illumination system without pre-calibrate the banding error for the system. Also, the de-banding performance of our algorithm results in a with 30× improvement, and it has better performance than active gamma correction method and has performance comparable with sophistic gamma calibration models.

Chapter 5 Relative Motion 3-D Scanner (RM3D)

In Chapter 3, we discussed our research on 2PFLR SLI depth Measuring system to solve the problem of relative motion within the field of view of the scanner. We extend our research to solve the problem of relative motion beyond the FOV of the scanner. The goal of the research in this chapter is to extend the SLI system to scan surface of object larger than the FOV by moving the scanner across the object to capture a series of non-ambiguous single pattern scans. Then by correspondence analysis, combine the overlapping images to achieve both non-ambiguous and high lateral resolution scan, larger than the scanner FOV.

For any SLI system, a limitation of its application is the FOV of the scanning system. This is caused by the structure of SLI system itself, since we need to project at least one pattern to object surface, the object needs to be inside the FOV of both camera and projector during the scanning procedure. Further limitation to FOV is the lateral resolution of the scanner. The scanner must be close enough to the object surface to achieve desired lateral resolution which has the tradeoff of limiting the FOV. Limited by the effective distance, the FOV of a scanner is not enough to cover many large scale objects. This raises the need for the 3-D scanner that is able to scan the object by allowing the relative motion between the scanner and the object. We call this scanner as Relative Motion 3-D scanner (RM3D). The additional methodology to achieve our goal is the correspondence analysis between overlapping scans.

We present the following sections to illustrate our research on RM3D scanner. In section 5.1, an introduction briefly describes RM3D scanning system. Section 5.2 describes the processing techniques for analysis the pattern used in Relative Motion 3-D scanner. Section 5.3 illustrates the 3-D surface alignment techniques which are used for generated the completed 3-D surface for a large scale object. Section 5.4 describes our post-processing method to decrease the accumulate error for the 3D surface alignment. Experimental results of the Relative Motion 3-D scanner are demonstrated in Section 5.5. And Section 5.6 is the summary for the whole chapter.

5.1 Introduction to Relative Motion 3-D Scanning System

There are numerous techniques in Computer Vision area that are able to reconstruct the 3-D surface or scene without the restriction of the relative position of the scanner and object, such as Structure from Motion (SfM) and high speed SLI techniques [70]-[74]. However, the result from SfM method is just a point cloud and the 3D points reconstructed are very sparse compared with SLI method [89]. In RM3D scanning system research, we introduce a scanning system based on the single pattern Structured Light Illumination system. The advantage of using single pattern SLI system is that the motion of the scanner will not affect the 3-D reconstruction procedure as long as the camera captured the reflected pattern image without blurring. Moreover, many single pattern SLI techniques can reach a satisfactory accuracy using the MCP technique.

Our fundamental idea of developing Relative Motion 3-D scanning system is to utilize a non-ambiguous single pattern SLI system to scan across the surface and capture a sequence of reflected overlapping images. Then, the surface is reconstructed by using each new image with the correspondence alignment of all processed images to obtain the completed 3-D surface. Some of the previous work using the same idea is presented in [41] – [45]. However, from the mathematical model of SLI technique, we know that the 3-D model reconstructed by using SLI technique is in a coordinate space relative to the scanner. We also know that the camera will change the position during the scan so we need to estimate the scanner's trajectory to increase the accuracy of the reconstruction.

5.1.1 System Setup for Relative Motion 3-D Scanner

In order to solve the problem of estimating the camera motion, we introduce a new pattern based on MCP technique with a novel constellation correlation filter pattern analysis method.

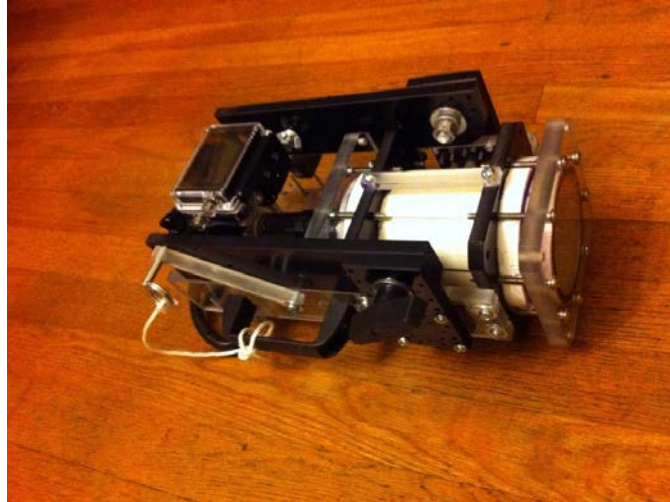


Figure 5.1 Relative Motion 3-D Scanning system, folded for portable

Fig. 5.1 and Fig. 5.2 show the prototype of the RM3D scanning system. The scanner is about 40cm high and less than 10 pounds in weight. The mechanical design makes the scanner portable and easy to use in the field or underwater. Fig. 5.2 displays the portable and operation configuration of the RM3D scanner. From Fig. 5.2 right we can see that our RM3D scanning system is built as a classical Structure Light Illumination system which consists of a projector and a camera forming triangulation geometry. A go pro camera with 1024 by 768 resolution and a LED flash light illumination source with a pattern slide cover on the aperture works as a projector. Without mounting a digital projector onto the scanner, our system is much more portable by removing the power cable for the projector and very easy to configure. Also, we can easily change the pattern that needs to be projected onto the object by replacing the 35mm slide.

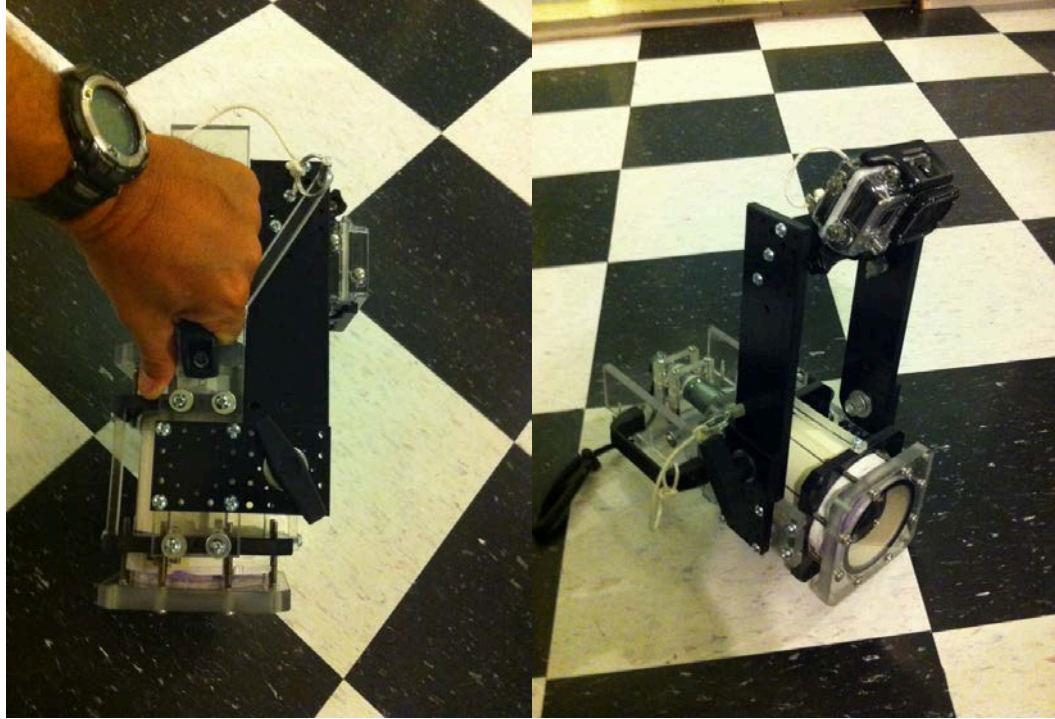


Figure 5.2 Relative Motion 3-D Scanner, Folded (left) and infolded for operation (right)

5.1.2 Pattern Design

Because we need to translate the scanner to scan the large object surfaces, it is inevitable that the operator will introduce motion of the camera. The projection pattern is designed to address this issue. We introduce a single pattern technique based on the MCP to solve the problem of estimating the camera position and alignment. We assume the object surface is static and only the camera is moving. Fig.5.3 shows the pattern used in Relative Motion 3-D scanner. There are a total of 9 snakes in the pattern in three groups. In each group there is a center snake that is modulated and on both side of that snake there is on un-modulated snake. The modulated snakes yield non-ambiguous cross section. The two un-modulated snakes are used to improve the cross section accuracy.

This RM3D pattern has two main differences from previous SLI. The first difference is that instead of using sinusoidal pattern or grid pattern that covers the whole area of captured image, the pattern for RM3D scanner only has a few of sinusoidal cycles with

three modulated snakes. In this way, there are large areas of “white space” in the pattern, The advantage of this design is the reflected surface in the white space region is used for correspondence without the disturbance of the snakes.

The second difference is that orthogonally modulated snakes are introduced to this pattern inspired by MCP. As we stated in Chapter 2, the modulated snakes yield non-ambiguous results, and the un-modulated snakes which are on both sides of the modulated snake help to locate and identify it. Also, unlike MCP, the modulated snakes in the RM3D pattern are not following the Gray Code order, so we don’t use the Matched Filter Bank technique as illustrated in Chapter 3. In this way, the process time of analyzing the pattern is much faster than process the MCP.

The RM3D pattern is shown in Fig. 5.3. The number of the snakes in the pattern affects the accuracy and the area of 3-D surface reconstructed by each frame captured by the camera, and the area of the white space between snake groups affects the accuracy of alignment of all the reconstructed 3-D patches. So there is a tradeoff between the accuracy of the 3-D reconstruction and the accuracy of the correspondence alignment between patterns. We reach a balance between the number of the snakes and the area of white space. From Fig. 5.3, the snake wavelength correspond to a total 22 cycles along the phase direction, and there are 9 snakes which are about 10.5 cycles. So the area of the snakes are about half of the image total area, and the other half is white space.

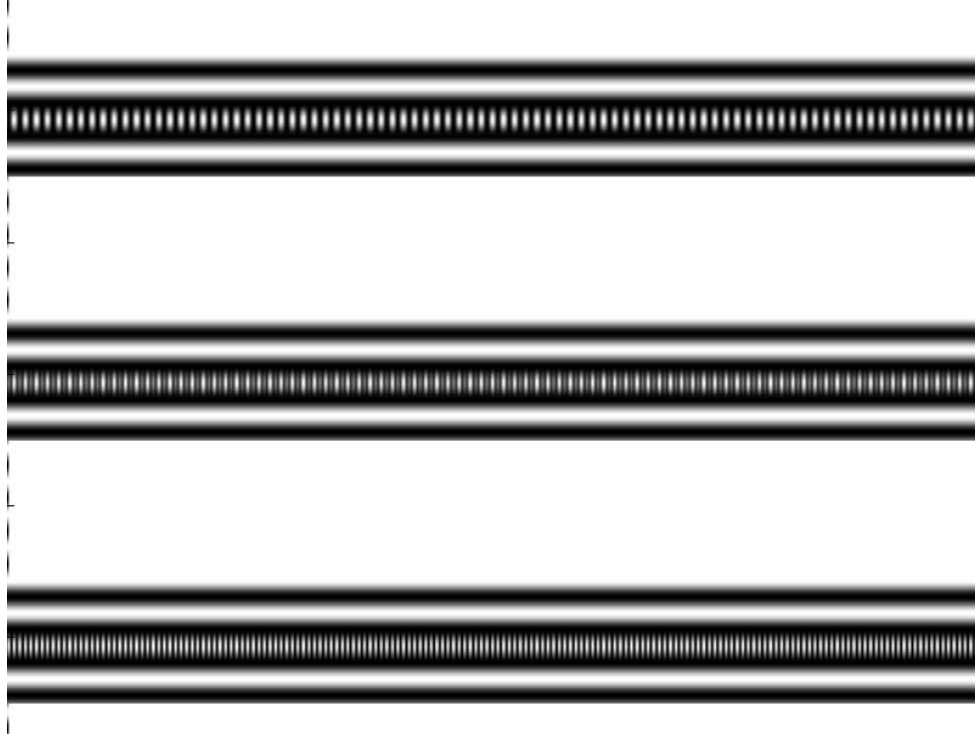


Figure 5.3 Optical Pattern for Relative Motion Scanning system

5.2 Relative Motion 3-D Pattern Analysis

The analysis and processing techniques for the RM3D pattern are illustrated. Although the RM3D pattern design is based on the MCP, we modify the pattern analysis technique described in Chapter 3, since only single pattern is used in RM3D scanning system, and a sequence of images captured by the scanner must be processed. In order to process the sequence of images efficiently, we introduce a pipeline process for analyzing the RM3D pattern. There are two processes in the pipeline which are discussed in the following sections, the first process is the snake detection and tracking for each frame, and the second part is the camera motion estimation based on a proposed Constellation Correlation Filter technique.

5.2.1 Snake Detection and Tracking

Similar to the MCP analysis techniques described in Chapter 3, for RM3D pattern analysis, the modulated snakes in the pattern need to be detected first, then after

demodulating, the phase value of each modulated snake are recovered by using the calibration parameters.

A 1-D Peak to Side-lobe Ratio (PSR) technique is proposed to isolate the snakes and identify the snakes' peaks. The 1D-PSR is defined as a 1-D space domain moving filter, for a given pixel in the image A , $P_1 = A(x_c, y_c)$, where (x_c, y_c) is its coordinate in camera space. The two neighborhood pixels along the phase direction are $P_0 = A(x_c, y_c - \tau)$ and $P_2 = A(x_c, y_c + \tau)$, where τ is a given integer constant which is a estimation of the width of a snake. So the 1-D PSR is defined as

$$PSR_\tau(P_1) \equiv \frac{P_1}{\max(P_0, P_2)} \quad (5.1)$$

Eq. (5.1) yields the PSR value for a given pixel in the image. We know that the 1-D PSR model is a peak point evaluation function which compared the intensity value of potential peak points with its side-lobe for a given peak width τ . Higher PSR value for a given pixel means this pixel is more likely being a peak value along the phase direction.

However, using a fixed τ value is not able to offer a satisfactory performance the width of the snakes vary across the surface. To optimize the result of PSR, in each calculation of PSR we loop to find the best τ to maximize the PSR value:

$$\tau(x_c, y_c) = \underset{\tau_{min} \leq \tau \leq \tau_{max}}{\operatorname{argmax}} \{PSR_\tau(A(x_c, y_c))\} \quad (5.2)$$

where τ_{min} and τ_{max} are the two bounds for τ , and their value is decided during the calibration procedure. By using the algorithm based on Eq. (5.2), we increase the robustness of peak detection. The relationship is represented as

$$\mathbf{A}_{PSR}(x_c, y_c) = \frac{P_1(x_c, y_c)}{\max(P_0, P_2)} \quad (5.3)$$

where $\mathbf{A}_{PSR}(x_c, y_c)$ is the PSR image which is then binaried as $\mathbf{B}_{PSR}(x_c, y_c) =$

$$\text{Binary}\{\mathbf{A}_{PSR}(x_c, y_c)\} \begin{cases} 1, \text{with } p > T \\ 0, \text{with } p < T \end{cases} \quad (5.4)$$

where T is a threshold set by experiment. In this research threshold is set to 1.18. An example of 1-D PSR peak isolation is shown in Fig. 5.4.

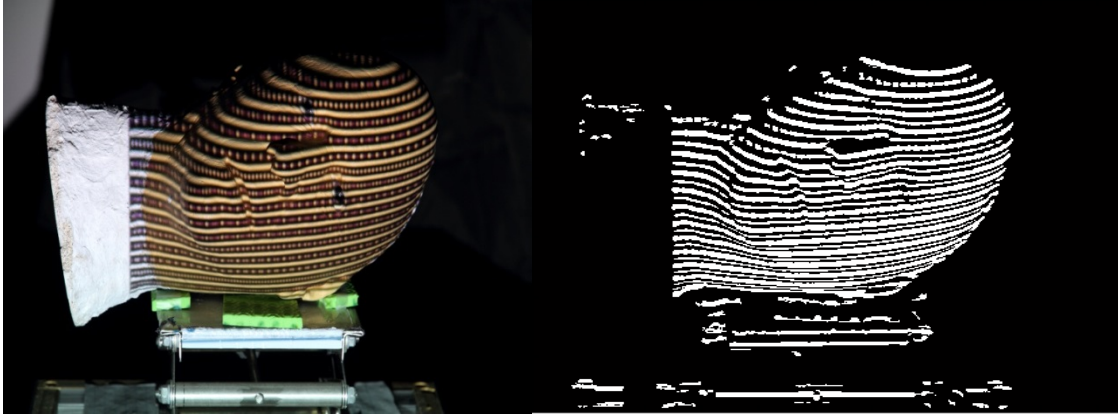


Figure 5.4 Original Image under test (left), result after PSR peak detection process (right)

As shown in Fig. 5.4, the PSR technique detects the snake regions effectively and efficiently. After generating the binarized PSR image \mathbf{B}_{PSR} , we define the very center of the region of each isolated snake along the phase direction in \mathbf{B}_{PSR} as the peak location as the same as in Chapter 3 for pattern analysis. Then we store the peaks location in the matrix \mathbf{Y} as represented in Eq. (3.7), and using the Matched Filters Bank to demodulate the snakes as the same procedures illustrated in Chapter 3.

After demodulating the snakes in the matrix \mathbf{Y} , the phase values for each snake are assigned based on the calibration file. We then save the detection result in a data structure called Snake4 Volume (S_{4V}) which consists of four snakes' matrices: S_p , S_y , S_i , and S_z .

$$S_{4V} = [S_p, S_y, S_i, S_z] \quad (5.5)$$

The definition for the four $M_S \times N$ matrices is expressed in Eq. (5.6) (a) to (d).

$S_p \equiv$ matrix of the peak intensity for each snake

$$S_p(x_c, m) = Y(x_c, m) \quad (5.6a)$$

$S_y \equiv$ matrix of the y coordinate for each snake

$$S_y(x_c, m) = y_c \quad (5.6b)$$

$\mathbf{S}_i \equiv$ matrix of the indicator for each snake

$$\mathbf{S}_i(x_c, m) = \begin{cases} 1, & \text{for } \mathbf{Y}(x_c, m) > 0 \\ 0, & \text{for } \mathbf{Y}(x_c, m) = 0 \end{cases} \quad (5.6c)$$

$$\mathbf{S}_z \equiv \text{matrix of the } z \text{ coordinate in 3D for each snake} \quad (5.6d)$$

Where matrix \mathbf{Y} is defined in Eq. (3.7), (x_c, y_c) is the coordinate for snakes' peak locations in camera space image, and m indices are the snake's index number. So for the four snakes matrices, the size is M_S height and N width, where $M_S \equiv$ Number of detected snakes, and $N \equiv$ width of original Image \mathbf{A} , and $m \in [1, M_S]$.

The reason to store the detected snakes in \mathbf{S}_{4V} data structure is to reduce the space complexity of the algorithm. Because there are only 9 snakes in the RM3D pattern, i.e. $M_S = 9$, so the total space request for \mathbf{S}_{4V} structure is $3 \times 9 \times N = 27N$. The total space required to store the PSR image in our research is $768N$, where 768 is the width of the captured image. Thus, we reduce the space costs about 28 times.

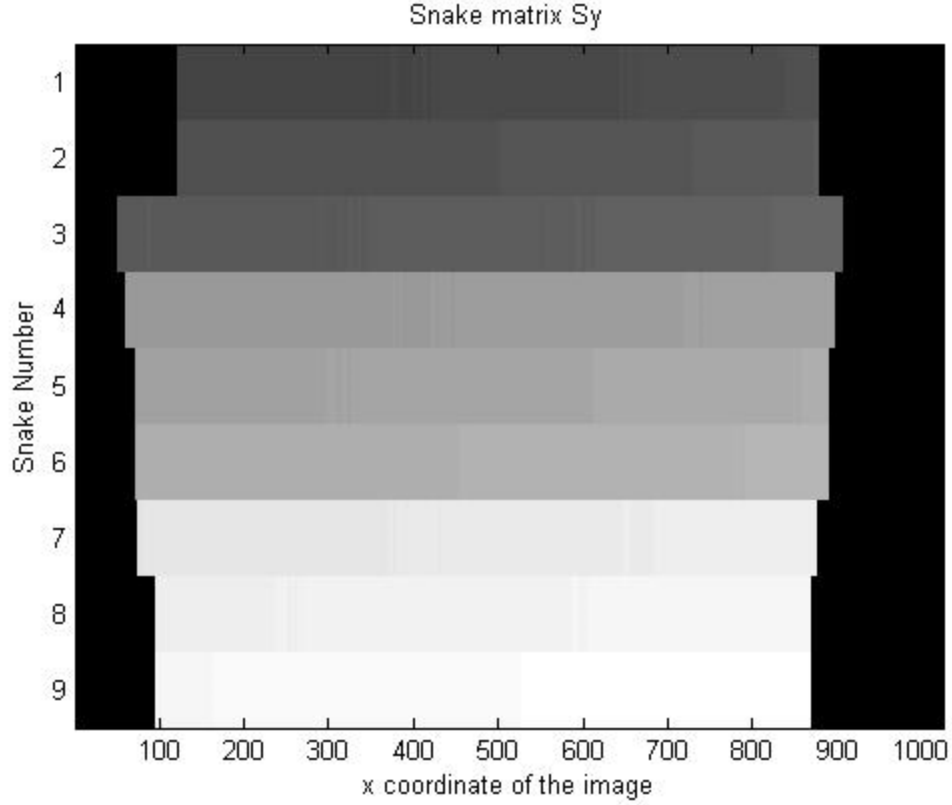


Figure 5.5 Snake Matrix S_y for Relative Motion 3-D pattern

Fig. 5.5 shows the S_y matrix after the PSR peak detection for the RM3D pattern analysis. The nine snakes are detected and stored in the matrix following the order of the snake number. The snake index number has a correspondence with the camera y coordinate as shown in Fig. 5.5.

After detecting the 9 snakes in the RM3D pattern for the first captured frame and storing the information in the S_{4V} data structure, one patch of the 3-D surface is reconstructed through reconstruction technique for Modified Composite Pattern described in Chapter 3. However, the 1-D PSR method used in snake detection is not as robust as the snake peak isolation method used in Two-Pattern SLI system, due to the variation of light conditions and the modulated snakes as shown in Fig. 5.6.

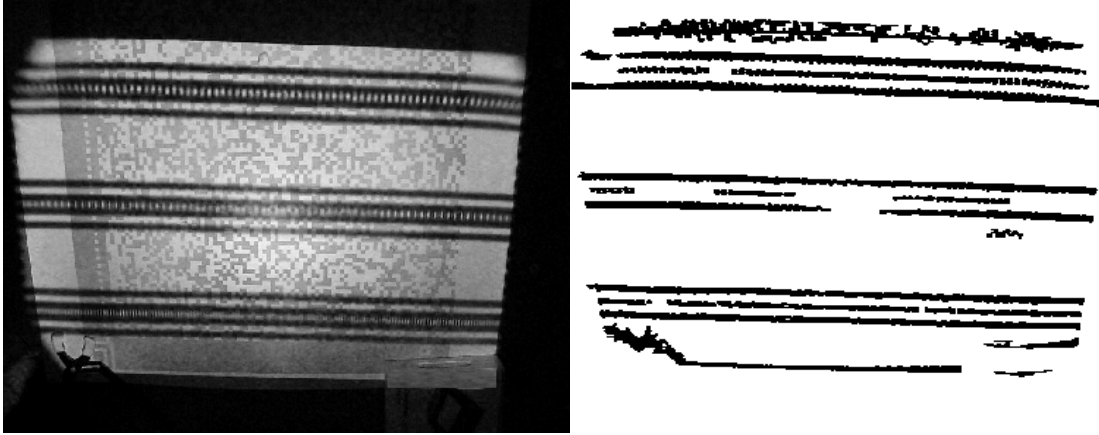


Figure 5.6 RM3D scan of test surface (left), PSR detection result(right)

Fig. 5.6 right displays the 1-D PSR detection result for a captured frame from Relative Motion 3-D scan. In the resulting PSR image, some sections of the snakes are not detected, and the detection rate for the modulated snakes are not as high as expected due to the light condition. So the snake growing technique is utilized to post process the detected snakes' peaks after PSR process.

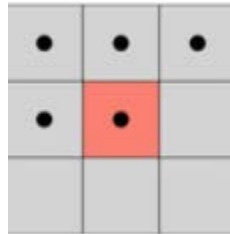


Figure 5.7 4-Connected Neighborhood

Like the snake growing algorithm used in Casey's work, we connect or "grow" from left to right, and since mathematically the 4-connected neighborhood are defined as the 4 pixels around the center pixel indicated by the black spots in Fig. 5.7, there is no need to grow from right to left. The pixel in red is the pixel under analysis.

A two pass 4-connected neighborhood checking method is used to find 4-connected component, one pass to record equivalences and assign temporary labels and the second to replace each temporary label by the label of its equivalence class [21].

Connectivity checks are carried out by checking the labels of pixels that are top right, top center to the center, top left and left of the current pixel. Conditions to check:

1. Does the pixel to the left have the same value?
 1. Yes - We are in the same region. Assign the same label to the current pixel
 2. No - Check next condition
2. Do the pixels to the top and left of the current pixel have the same value but not the same label?
 1. Yes - We know that the top and left pixels belong to the same region and must be merged. Assign the current pixel the minimum of the top and left labels, and record their equivalence relationship
 2. No - Check next condition
3. Does the pixel to the left have a different value and the one to the top the same value?
 1. Yes - Assign the label of the top pixel to the current pixel
 2. No - Check next condition
4. Do the pixel's top and left neighbors have different pixel values?
 1. Yes - Create a new label ID and assign it to the current pixel

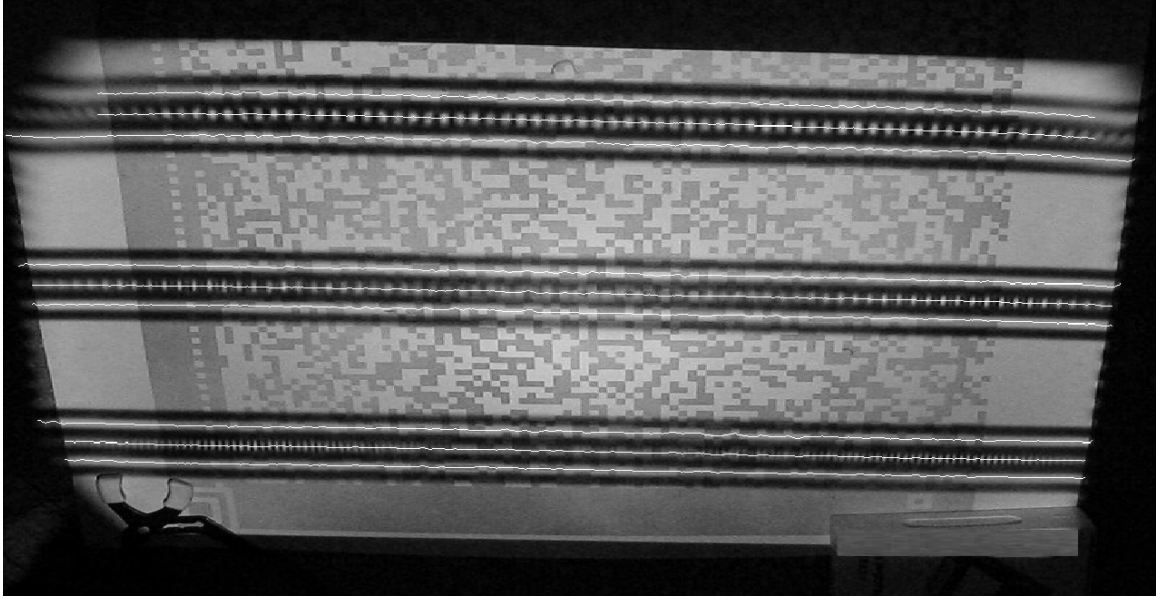


Figure 5.8 Snakes Peaks Detection result after snake growing

The final result of snake detection is shown in Fig. 5.8. The white lines which lie on the pattern are the snake's peaks detected and grown by the algorithm.

After growing the snakes in the first frame, we don't have to re-run the snake growing algorithm for every frame in our system. A tracking algorithm across frames to track snakes. The fundamental idea of the snake tracking algorithm is that the snakes' position in the captured images will not change much from frame to frame. This idea based on the assumption that the relative motion between the scanner and the object during the scanning procedure is smooth in translation and in-plane rotation and there is no extreme out-planes rotation of the scanner. Without extreme out-plane rotation, the capture image always has the pattern lies on similar location as the previous captured image. Based on this idea and assumption, the snake tracking algorithm:

- (1) For a given i th frame (not the first one), utilize the 1-D PSR detection method to detect the Snake Peaks.
- (2) Read in previous frame's S_{4V} , and generate the snake peak image based on S_{4V} .
- (3) For each detect peak point (x_i, y_i) in i th frame, compare with the all the peak points

with the same x coordinate in i -1 frame $(x_{i-1,n}, y_{i-1,n})$. If $|y_{i-1,n} - y_i| < T_s$, given $x_i = x_{i-1,n}$, where n is the snake number for the snakes' peak points in i -1th frame and T_s is a pre-defined threshold for the snake tracking process. Then this peak point (x_i, y_i) belongs to the snake with snake number n , and labels this point as valid snake peak points.

(4) Store all the labeled peak points into a new S_{4V} data structure for current frame.

(5) Continue to next frame.

In our research the threshold is set to $T_s = 4$, which means there is at most 4 pixel differences between the current frame's snake peaks and the previous frame's.

5.2.2 Camera Position Estimation by using Constellation Correlation Filters

The RM3D pattern has white space is between the number 3 and number 4 snakes, and number 6 and number 7 snakes, the white space area is able to be located by using the S_{4V} data structure. We assume the scanning speed of the scanner allows for a large overlap area between two consecutive frames in the captured frame sequence. So, we are able to align the frames based on the captured surface texture within the white space. Based on the alignment of the frames, the fundamental idea of the camera position estimation is to calculate the 2-D transformation including translation and rotation between each two consecutive frames, then secondly, the 3-D surface information is reconstructed [53] [56].

It is well known that image correlation technique based on composite filters [48]-[51] is an efficient, effective and robust method to match two similar signals. So, correlation technique is widely used in many pattern recognition and image processing applications. In our research, the correlation method is also utilized to align the surfaces between the two captured frames. However, if we directly correlate the two consecutive frames, the results are corrupted by noise and spatial distortion. To get a more accurate and robust result, we use a Constellation Correlation Filters method.

As shown in Fig. 5.9, we partitioned the captured surface into several partitions within the white space. We refer to that partitions as constellations and the alignment algorithm

correlates the constellation partitions between two consecutive frames. 14 partitions (marked as white squares) are utilized which are displayed in Fig. 5.9.



Figure 5.9 Partitions (white areas) for Constellation Correlation

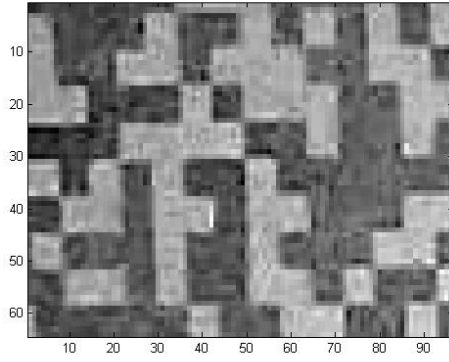
The mathematical model of correlating the constellations is illustrated as follows. For two consecutive frames A_i and A_{i+1} in the captured sequence, the partition is represented as:

$$S_{i,j} \equiv j \text{ th partition in the } i \text{ th frame} \quad (5.7)$$

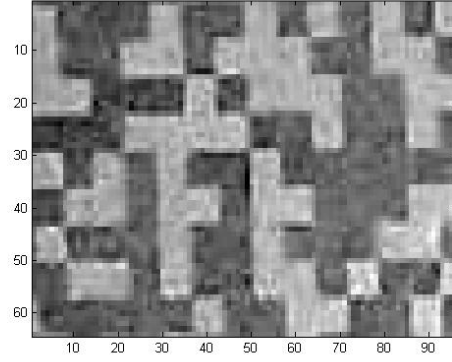
Then, the correlation result for each corresponded partition is expressed in Eq. (5.8).

$$C_j^{i,i+1} = S_{i,j} * S_{i+1,j} \quad (5.8)$$

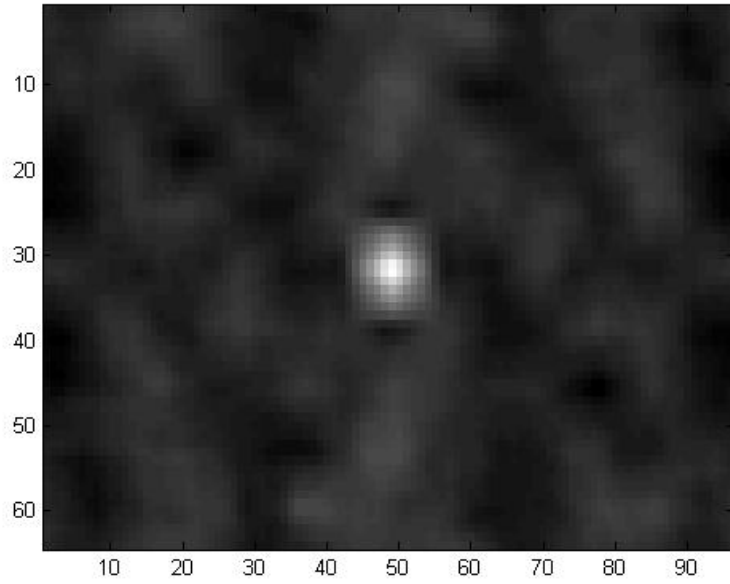
where the $C_j^{i,i+1}$ is the correlation result between the j th partition of i and $i+1$ frames, and $*$ denotes the correlation.



(a)



(b)



(c)

Figure 5.10(a) Number 3 partition in current frame; (b) Number 3 Partition in previous frame; (c) Correlation results with shifting the peak to the middle of the image

An example of two partitions and their correlation result is shown in Fig. 5.10. In Fig. 5.10(c), the peak of the correlation provides the information of the translation to align the two partitions. The translation is stored in a matrix $CT_j^{i,i+1}$ as expressed in Eq. (5.9).

$$CT_j^{i,i+1} = \begin{bmatrix} x_t \\ y_t \end{bmatrix} \quad (5.9)$$

where x_t stands for the translation in x direction and y_t stands for the translation in y direction.

However, not all the correlation results of the partitions are accurate, so a Mean Square Displacement (MSD) checking process is proposed to eliminate the wrong correlation results. The partitions in the i th frame is translated by using the matrix $CT_j^{i,i+1}$ at first:

$$ST_{i,j}(x, y) = S_{i,j}(x + x_t, y + y_t) \quad (5.10)$$

where $ST_{i,j}$ is the translated j th partition in frame i .

We calculate the Mean Square Displacement for j th partition E_j as

$$E_j = \frac{\sum_{m=1}^{M_s} \sum_{n=1}^{N_s} |ST_{i,j}(m, n) - S_{i+1,j}(m, n)|^2}{M_s N_s} \quad (5.11)$$

where M_s and N_s are the width and height of the partition. A threshold T_E is set to check if the $CT_j^{i,i+1}$ is a valid translation.

$$CT_j^{i,i+1} = \begin{cases} \text{Valid}, & \text{for } E_j < T_E \\ \text{Not valid}, & \text{for } E_j \geq T_E \end{cases} \quad (5.12)$$

In Eq. (5.12), we utilize the calculated MSD of each pair of partitions to label the translation matrix $CT_j^{i,i+1}$. The invalid translations are eliminated and only valid translations are used. Fig. 5.11 plots the exponential MSD for the 14 partition pairs.

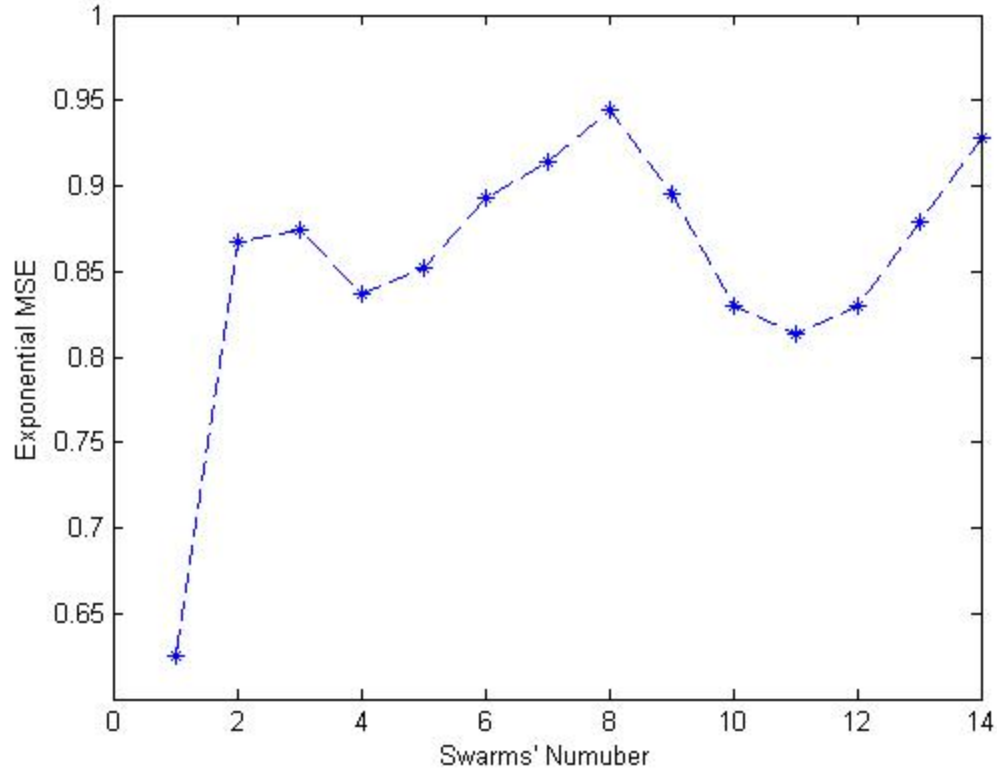


Figure 5.11 Exponential MSD of 14 Partitions

In Fig 5.11, we display the exponential MSD as

$$ExpMSD_j = e^{-E_j} \quad (5.13)$$

where E_j is the MSD in Eq. (5.12). We use $ExpMSD_j$ because low E_j approaches 1 and high E_j approaches 0.

Based on the valid correlation results which are expressed as translation matrices, the 2-D transformation matrix is able to be calculated. We express the 2-D coordinate in homogenous coordinate, so the 2-D transformation matrix is a 3 by 3 matrix, and accordingly the 3-D transformation matrix is a 4×4 matrix. The 2-D transformation matrix satisfies the Eq. (5.14) below.

$$\begin{bmatrix} x_{0,t} \\ y_{0,t} \\ t \end{bmatrix} = T_{2D} \begin{bmatrix} x_0 \\ y_0 \\ 1 \end{bmatrix} \quad (5.14)$$

where \mathbf{T}_{2D} is the 3×3 2-D transformation matrix, (x_0, y_0) is the original 2-D coordinates, and the transformed coordinates are

$$\begin{bmatrix} x_1 \\ y_1 \end{bmatrix} = \begin{bmatrix} \frac{x_{0,t}}{t} \\ \frac{y_{0,t}}{t} \end{bmatrix} \quad (5.15)$$

where the (x_1, y_1) are the transformed 2-D coordinates. From Eq. (5.14) we know that in order to calculate the 2-D transformation matrix \mathbf{T}_{2D} , the two homogenous coordinates are needed. And then, the transformation matrix is calculated as Eq. (5.16).

$$\mathbf{V}_0 \mathbf{T}_{2D} = \mathbf{V}_t \quad (5.16)$$

where

$$\mathbf{V}_t = \begin{bmatrix} x_{0,t} \\ y_{0,t} \\ t \end{bmatrix} \quad (5.17a)$$

$$\mathbf{V}_0 = \begin{bmatrix} x_0 \\ y_0 \\ 1 \end{bmatrix} \quad (5.17b)$$

From the results of the correlation for two consecutive frames A_i and A_{i+1} in the captured sequence which are illustrated in above, the two vectors \mathbf{V}_0 and \mathbf{V}_t are able to be generated. Since (x_0, y_0) is the 2-D coordinates before the transformation, all the coordinates lie in the valid partitions $S_{i,j}(x, y)$ in A_i are allowed to be utilized in the coordinate vector \mathbf{V}_0 . To get the vector \mathbf{V}_t , we use the correlation result $CT_j^{i,i+1}$ to translate the coordinates in valid partitions $S_{i,j}(x, y)$ to get the coordinates $(x_{0,t}, y_{0,t})$ as illustrated in Eq. (5.18).

$$\begin{bmatrix} x_{0,t} \\ y_{0,t} \end{bmatrix} = \begin{bmatrix} x_0 \\ y_0 \end{bmatrix} + CT_j^{i,i+1} = \begin{bmatrix} x_0 + x_t \\ y_0 + y_t \end{bmatrix} \quad (5.18)$$

However, there are at least 14 partitions and the size of the partitions are 64 by 64 in our research, so we have total $64 \times 64 \times 14 = 57344$ sample points that can be used as \mathbf{V}_0 . In order to get an accurate estimation of the 2-D transformation matrix, the more points are required to be used in the calculation process. This results in a typical least square

problem, so the classical least square method is chosen to utilize more points to improve the estimation of \mathbf{T}_{2D} . The least square representation is expressed in Eq. (5.19a).

$$\mathbf{T}_{2D} \cdot \mathbf{M}_0 = \mathbf{M}_t \quad (5.19a)$$

where \mathbf{M}_t and \mathbf{M}_0 are the matrices composed by the homogenous coordinates vectors as represented in

$$\mathbf{M}_0 = [\mathbf{V}_0^1 \quad \cdots \quad \mathbf{V}_0^n] \quad (5.19b)$$

$$\mathbf{M}_t = [\mathbf{V}_t^1 \quad \cdots \quad \mathbf{V}_t^n] \quad (5.19c)$$

In order to calculate the 2-D transformation matrix, we need to calculate the pseudo-inverse of the matrix \mathbf{M}_0 . A widely used pseudo inverse calculation method is Moore-Penrose pseudo inverse method, which is expressed in Eq. (5.20).

$$\mathbf{T}_{2D} = \mathbf{M}_t \mathbf{M}_0^T (\mathbf{M}_0 \mathbf{M}_0^T)^{-1} \quad (5.20)$$

where \mathbf{M}_0^T is the transpose of the matrix \mathbf{M}_0 .

The 2-D transformation between two consecutive frames is estimated from the constellation and has the parameters as

$$\mathbf{T}_{2D} = \begin{bmatrix} \cos\theta & \sin\theta & t_x \\ -\sin\theta & \cos\theta & t_y \\ 0 & 0 & 1 \end{bmatrix} \quad (5.21)$$

where θ denotes the clock-wise rotation angle, t_x and t_y are the translation in x and y directions, respectively.

The camera is moving in 3-D coordinates, so the estimation of \mathbf{T}_{2D} is not enough to determine the 3-D of the camera. However, if we make some assumptions, the 3-D transformation matrix \mathbf{T}_{3D} can be approximated by using the 3-D cross section information.

In the prototype RM3D Scanner, we assume there is no significant movement along the z direction, and we assume no out of plane rotation. Under these assumptions, the

translation in z in T_{3D} is zero, and there is only in-plane rotation relate to z axis. T_{3D} is expressed as

$$T_{3D} = \begin{bmatrix} \cos\theta & \sin\theta & 0 & t'_x \\ -\sin\theta & \cos\theta & 0 & t'_y \\ 0 & 0 & 1 & t'_z \\ 0 & 0 & 0 & 1 \end{bmatrix} \quad (5.22)$$

where θ is the clock-wise rotation angle, and t'_x , t'_y , and t'_z are the translation along x, y and z directions, respectively and t'_z is almost 0.

The θ is estimated in Eq. (5.21), so the 3-D rotation is estimated in Eq. (5.22). Our goal is to estimate t'_x , t'_y , and t'_z based on 2-D translation t_x and t_y . In our research, we proposed a method to solve this problem based on the calibration based on the assumption that there is not a big depth jump between two consecutive frames. Fig. 5.12 demonstrates the geometry of estimation of t'_x and t'_y .

As shown in Fig. 5.12, O is the optical center of the camera. During the calibration process, we calibrate for a translation in t_x and its corresponding translation in 3-D at depth d_1 , which is $t'_{x,d1}$. The relationship is expressed as

$$t'_{x,d1} = \frac{d_1}{f} t_x \quad (5.23)$$

And for t'_y , we have the same relationship and same calculation procedures.

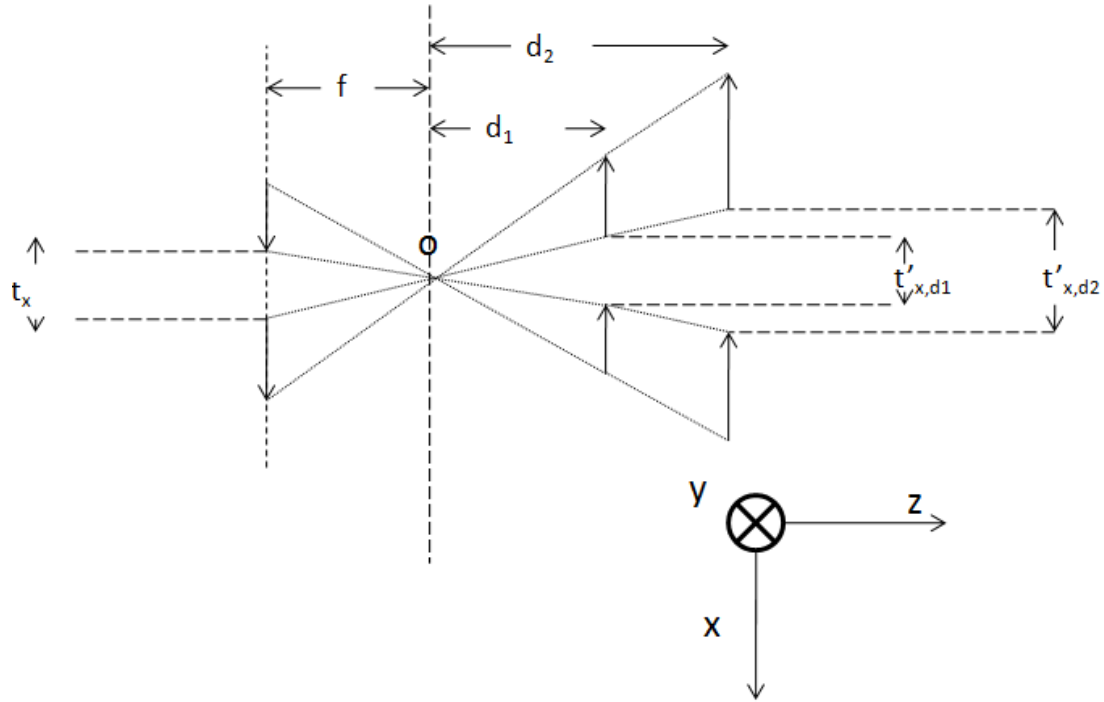


Figure 5.12 Geometry of estimation of 3-D transformation matrix

As described in section 5.2.1, after we demodulated the snakes, we are able to get the depth of the snakes. So in Eq. (5.25), depth d_l is known, and f is calibrated during the calibration process. In this way the 3-D translation $t'_{x,d1}$ at d_l depth is calculated. Also for the 3-D translation at y direction t'_y , we have the same process. Then, the 3-D transformation matrix \mathbf{T}_{3D} is recovered. Fig. 5.13 summarizes the pattern analysis algorithm.

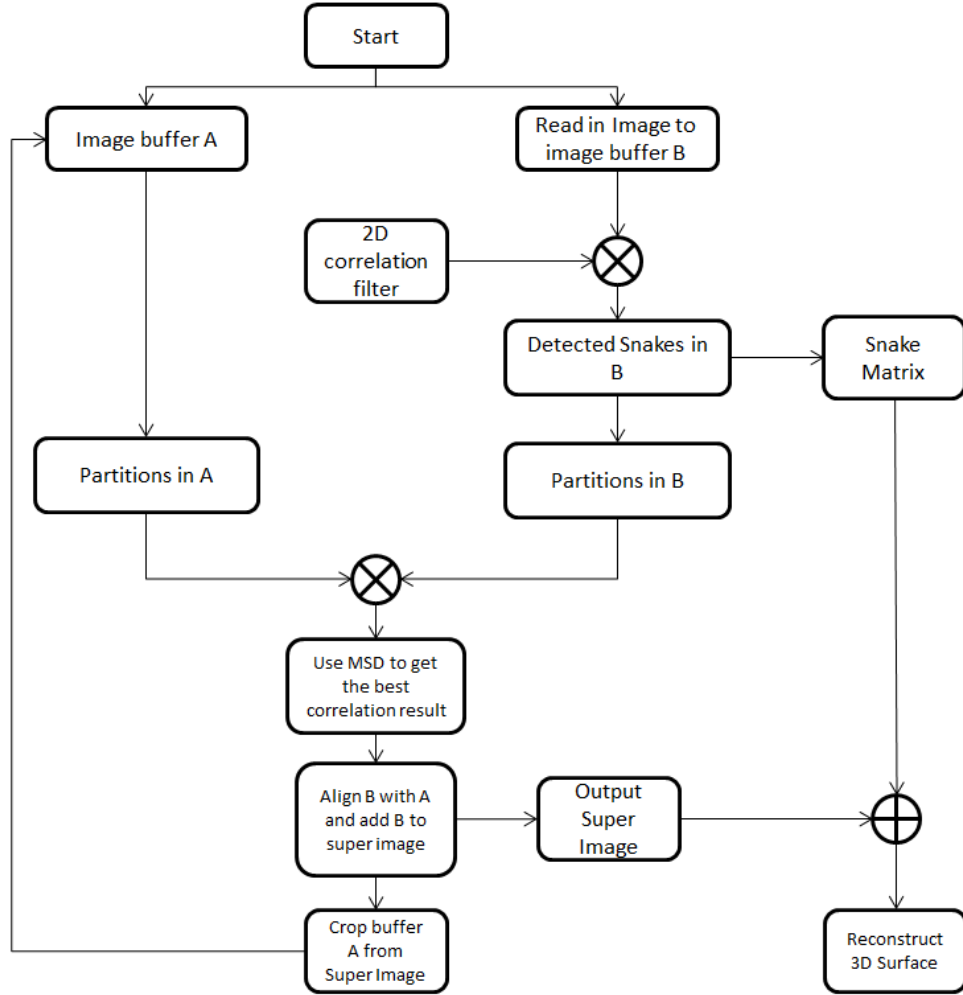


Figure 5.13Block Diagram for Snake Tracking and Constellation Correlation for Transformation Matrix Estimation algorithm

5.3 3-D Surface Alignment Based on Estimated Transformation Matrix

Based on the results from section 5.2, in this section we illustrate the technique and process of aligning the 3-D patches into a big large scale 3-D surface.

The fundamental idea is to use each frames' detected snakes which are stored in the S_{4V} data structure to reconstruct a 3-D patch for the frame, then use the estimated 3-D transformation matrix to align the 3-D patches for each frame into a larger point cloud representing the surface. Fig. 5.14 displays the recovered phase image of the nine snakes

for one frame. Based on this phase image, we are able to directly reconstruct the 3-D surface which are captured in this frame by using the MCP 3-D reconstruction technique.

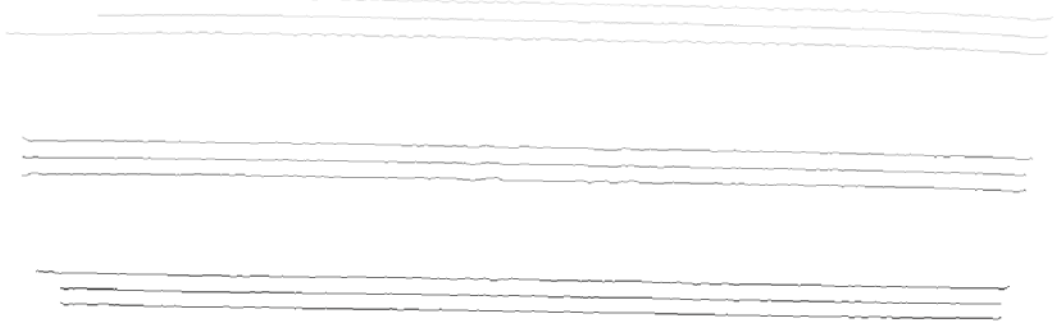


Figure 5.14 Recovered Phase Image for the nine snakes, depth information for only nine snakes

We use the 3-D transformation matrix between each two frames which is $T_{3D}^{i,i+1}$, to transform the reconstructed 3-D coordinates. Fig. 5.15 shows the point cloud of transformation result.

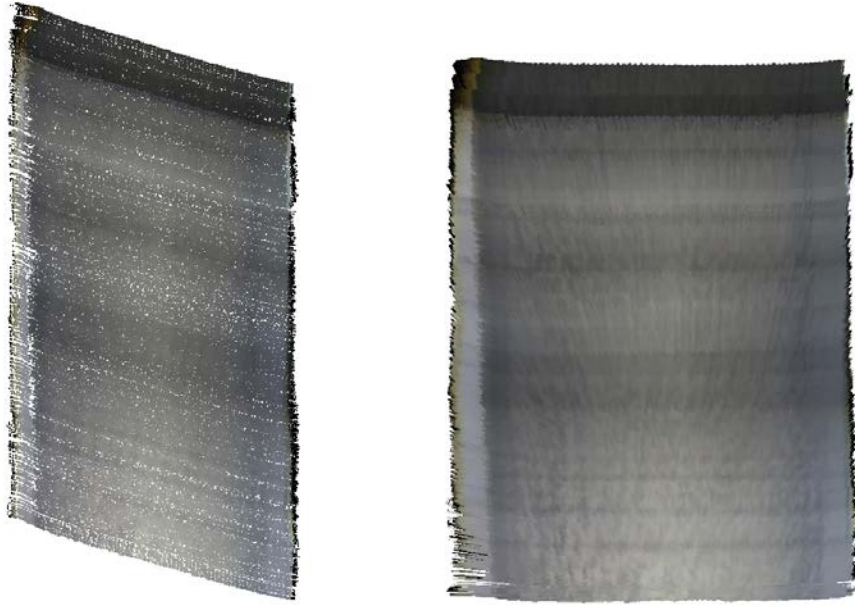


Figure 5.15 Point Cloud for 3-D reconstruction of all aligned patches, side view (left), frontal view (right)

5.4 Post Processing to Decrease the Accumulate Error

We know that the transformation matrix \mathbf{T}_{3D} is calculated based on the correlation between two consecutive frames, however, this technique will have the accumulate error. In this section, we describe the post processing method for decrease the accumulate error for the aligned 3-D reconstruction.

Our goal is to decrease the accumulated error and correct the \mathbf{T}_{3D} between each two consecutive frames. Since the 3-D transformation matrix \mathbf{T}_{3D} is calculated based on the transformation matrix \mathbf{T}_{2D} , we decide to correct \mathbf{T}_{2D} directly then re-calculate \mathbf{T}_{3D} . The basic idea of decreasing the accumulate error is to re-calculate the $\mathbf{T}_{2D}^{n-1,n}$ based on not just on an adjacent frame but a series of frames more distant in displacement. That is, the two frames are separated by k frames in time, let $\mathbf{T}_{2D}^{n-k,n}$ be the transformation matrix between the $n-k$ th frame and n th frame, and k denotes the distance between two frames.

Firstly, in order to effectively decrease the accumulate error, we varies the k from 2 to a fixed upper-bound K as expressed as follows:

$$k \in [2, K] \quad (5.24)$$

Then, we re-calculate the 2-D transformation matrix between n th frame and $n-k$ th frame, which is expressed as

$$\mathbf{T}_{2D}^{n-k,n} = \prod_{i=0}^{k-1} \mathbf{T}_{2D}^{n-i,n-(i-1)} \quad (5.25)$$

Then, by using the 2-D transformation matrix $\mathbf{T}_{2D}^{n-k,n}$, we align the $n-k$ th frame and n th frame. Since we have accumulated error, the two frames are not perfectly aligned.

Then, we follow the procedures described in section 5.2 to use the constellation correlation filters to calculate a 2-D transformation matrix \mathbf{T}_C which is a correction matrix. This \mathbf{T}_C corrected the matrix $\mathbf{T}_{2D}^{n-k,n}$ to achieve improved alignment as

$$\mathbf{T}_{2D,C}^{n-k,n} = \mathbf{T}_C \mathbf{T}_{2D}^{n-k,n} \quad (5.26)$$

where $\mathbf{T}_{2D,C}^{n-k,n}$ is the corrected 2-D transformation matrix with decreases accumulated error.

Then, we calculate the corrected 2-D transformation as

$$\mathbf{T}_k^{n-1,n} = \mathbf{T}_{2D,C}^{n-k,n} \cdot \prod_{i=1}^{k-1} (\mathbf{T}_{2D}^{n-i,n-(i-1)})^{-1} \quad (5.27)$$

where $\mathbf{T}_k^{n-1,n}$ is the corrected 2-D transformation matrix for $\mathbf{T}_{2D}^{n-1,n}$ based on the correlation between $n-k$ and n frame. The final step is to average all the calculated $\mathbf{T}_k^{n-1,n}$ for each k to get a 2-D transformation matrix with decreased accumulated error.

$$\mathbf{T}_{2D,DAE}^{n-1,n} = \frac{1}{K-1} \sum_{k=2}^K \mathbf{T}_k^{n-1,n} \quad (5.28)$$

We refer $\mathbf{T}_{2D,DAE}^{n-1,n}$ as reduced accumulated error (RAE). Then we repeat the process for all the transformation matrices to decrease the accumulate error.

The algorithm for decreasing the accumulated error is summarized as follows:

for n th frame in the captured frames:

for k from 2 to K :

calculate $\mathbf{T}_{2D}^{n-k,n}$;

transform frame A_n to align with frame A_{n-k} by using $\mathbf{T}_{2D}^{n-k,n}$;

calculate the correction transformation matrix \mathbf{T}_C ;

use \mathbf{T}_C to correct 2-D transformation matrix $\mathbf{T}_{2D,C}^{n-k,n}$, the result is $\mathbf{T}_{2D,C}^{n-k,n}$;

calculate the corrected 2-D transformation matrix $\mathbf{T}_k^{n-1,n}$;

end

average $\mathbf{T}_k^{n-1,n}$ to get $\mathbf{T}_{2D,DAE}^{n-1,n}$;

end

5.5 Experimental Results of 3-D Motion Scanner

The experiment setup is shown in Fig. 5.16, we mounted the scanner on to a train in order

to ensure there is no out-plane rotation. The object is surface is shown in Fig. 5.17. We put a towel onto an artifact to create a large scale object surface.

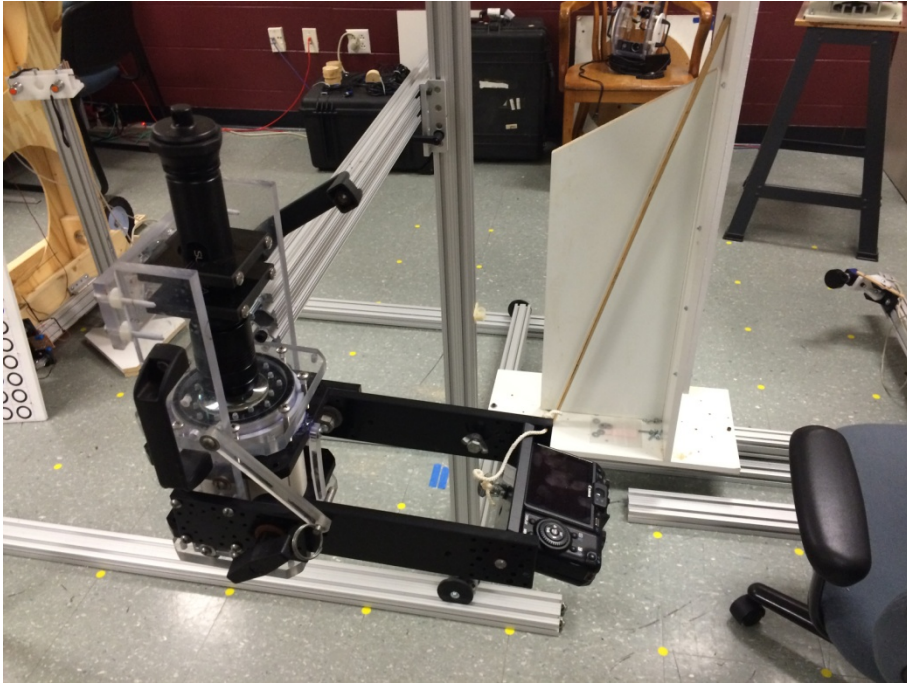


Figure 5.16 Experimental setup

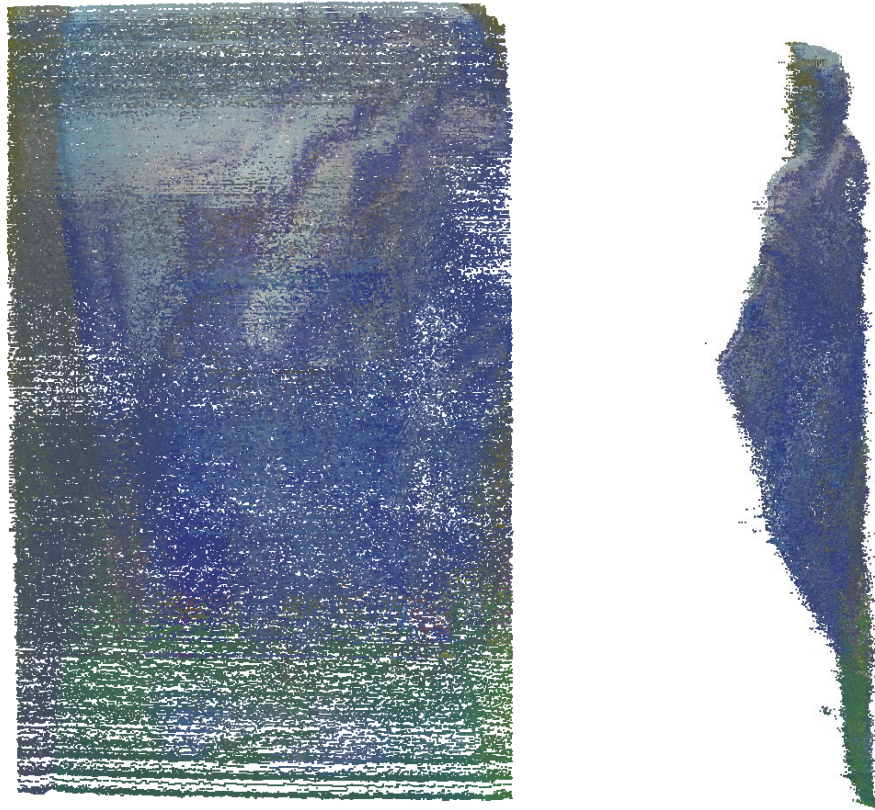


Figure 5.17 Front view of scanned object surface (left), side view of scanned object (right)

Fig. 5.18 displays the result of points cloud of the scanned object surface. We can see the points cloud is not as dense as traditional SLI scan. However, the actual shape of the object surface is reconstructed. And further research needed to achieve a higher accuracy of the reconstruction.

5.6 Summary

In this chapter the Relative Motion 3-D Scanning system is discussed and illustrated. Unlike the classical SLI depth measuring system, our system focus on developing a 3-D scanner allows the relative motion beyond the Field of View of scanner. In our research, we designed a new pattern especially for the Relative Motion 3-D scanning system, and this pattern is designed based on the MCP technique. Not only the 3-D depth information is able to be retrieved by the 9 snakes in the pattern, but also we can use the captured surface texture to do the alignment. A constellation correlation filters technique is developed to align the frames in the captured image sequences. By utilizing this

technique, the 2-D transformation matrix between two consecutive frames is estimated robustly. Furthermore, the 3-D transformation matrix for the estimation of camera position is estimated by using the 2-D transformation matrix. In this way, the points cloud for the large scale object surface is recovered by aligning the 3-D patches reconstructed from each frame through the 3-D transformation matrix. The final step is to decrease the accumulated error to achieve a better reconstruction. A post processing technique is developed.

Chapter 6 Conclusion and Future Research

We summarize our present and the future research in section 6.1 and 6.2 respectively. Section 6.1 summarizes all the work in our present research for 2PFLR SLI and RM3D SLI depth measuring, and section 6.2 provides the direction for future research based on the results of our current research.

6.1 Conclusion

Our research focuses on developing high speed and high accuracy SLI depth measuring system which can be applied to solve many problems in Computer Vision and 3-D data acquisition area. SLI technique is widely researched and already being used in many industrial 3-D scanners due to its high accuracy and non-ambiguity reconstruction. However, in order to achieve a high accuracy result, most of the SLI techniques rely on multi-pattern SLI techniques which are sensitive to continuous relative motion between the scanning system and the object surface. Multi-pattern method suffer from banding distortion and require lower velocities of the object and have tolerance toward depth ambiguity. This raises the need for developing high speed 3-D scanning systems with reduced sensitivity to the relative motion between the scanner and the object.

Based on the fundamental idea of the single pattern SLI technique, our first research direction is to study a high speed SLI system that allows the relative motion within the FOV of the scanner. We introduce Two-pattern Full Lateral Resolution (2PFLR) SLI depth measuring system. At first analysis, this seems to share the same sensitivity to motion between patterns but in fact we have separated functionality of the two patterns to allow continuous motion, certainly more than 3 patterns PMP technique. Single pattern SLI system, such as Composite Pattern (CP), Modified Composite Pattern, and de-bruijn modulated Pattern are not able to achieve a high accuracy result. To solve this problem and inspired by the non-ambiguous MCP technique, we introduce the 2PFLR SLI system. By including a second high frequency sinusoidal pattern, we not only achieve the full lateral resolution which in turn leads to a high accuracy 3-D reconstruction, but also reduce the number of the patterns utilized to two. Since there are only two patterns in our

2PFLR, the system is comparable to the single pattern technique in the term of the speed. And the most significant feature is our 2PFLR system allows the relative motion between the scanner and the object as long as the object stays in the FOV of the scanner. In our 2PFLR system, the first pattern is a MCP associated with an improved processing technique based on Casey's work, and the second pattern is a high frequency sinusoidal pattern. The MCP is utilized to achieve non-ambiguous 3-D reconstruction. The 2nd pattern is used to achieve full lateral resolution with a novel Quadrature Processing technique.

Although our 2PFLR SLI system achieves the goal of high scanning speed, the 3-D reconstruction has a significant banding distortion. The banding distortion is an issue in the SLI techniques due to the gamma distortion of the projected sinusoidal wave, interference by surface contrast, and quantization error of the hardware system. The banding artifact corrupts the 3-D surface and affects the accuracy of the depth measurement. To reduce the banding error, we introduce a Projector Space De-banding (PSDb) algorithm which is applicable to most SLI systems. Our PSDb algorithm is based on the estimation of the banding error in projector space, and actively suppresses it in camera space.

The second research direction is to allow the relative motion beyond the FOV the scanner. The goal of this research is to develop a portable SLI scanning system for large scale object 3-D reconstruction. We introduce a single pattern SLI system combined with image correspondence alignment to achieve surface scan areas beyond the scanner FOV. We design a new single pattern based on MCP technique that has open areas for image correspondence. To achieve robust correspondence that allows for irregular scanner trajectory, a Constellation Correlation Filter method is developed to track the camera by estimating the 3-D transformation matrix sequence of the camera. We use a two pass approach to increase the accuracy of the alignment across several frames to reduce accumulated error. By using the 3-D transformation matrix sequence, all the image frames are aligned to a single point cloud of the entire surface.

6.2 Future Research

For the 2PFLR SLI depth measuring system, the accuracy depends on the frequency of the 2nd sinusoidal pattern, however this spatial frequency is limited by the first MCP, so the future research may try other types of non-ambiguous single pattern for non-ambiguous phase recovery. For the RM3D scanner research, the scanning system needs estimation of out plane rotation to allow more robust images in uncontrolled environment. The future research may include testing other Computer Vision technologies and algorithms to improve the camera tracking problem and combine with the SLI techniques to achieve a more robust and portable 3-D scanning system.

References

- [1] H. S. Yang, K. L. Boyer, and A. C. Kak, "Range data extraction and interpretation by structured light," in *Proc. 1st IEEE Conference Artificial Intelligence. Applications, Dec. 1984, pp. 199-205.*
- [2] K. L. Boyer, and A. C. Kak, "Color-Encoded Structured Light for Rapid Active Ranging", *IEEE Transactions on Pattern Analysis and Machine Intelligence, VOL, PAMI-9, NO.1, January 1987*
- [3] V. Srinivasan, H. C. Liu, and M. Halioua, "Automated Phase-measuring Profilometry of 3D Diffuse Objects", *Applied Optics, Vol 23, Issue 18, 1984*
- [4] Mitsuo Takeda, and Kazuhhiro Mutoh, "Fourier Transform Profilometry for the Automatic Measurement of 3D Object Shapes", *Applied Optics, Vol. 22, No. 24, Decemeber, 1983*
- [5] Dalit Capspi, Nahum Kiryati, and Joseph Shamir, "Range Imaging With Adaptive Color Structured Light", *IEEE Transactions on Pattern Analysis and Machine Intelligence, Vol. 20, NO. 5, May, 1998*
- [6] C. Guan, L. G. Hassebrook, and D. L. Lau, "Composite Structured Light Pattern for Three-Dimensional Video", *Optics Express, Vol. 11, No. 5, March 2003*
- [7] G. Schmaltz of Schmaltz Brothers Laboratories, "A method for presenting the profile curves of rough surfaces", *Naturwiss 18, 315–316 (1932).*
- [8] Chun Guan, Laurence G. Hassebrook, Daniel L. Lau, Veeraganesh G. Yalla, and Charles J. Casey, "Improved Composite-Pattern Structured Light Profilometry by Means of Post processing", *Optical Engineering, Vol. 47, No. 9, September, 2008.*
- [9] Pratibha Gupta, "Gray Code Composite Pattern Structured Light Illumination", *Master Thesis, University of Kentucky, 2007.*
- [10] Charles Casey, Laurence G. Hassebrook, Minghao Wang, "Depth Matched Transfer

Function of the Modified Composite Pattern Structured Light Illumination Method”, *high-speed 3D optical metrology and applications, Optical Engineering*, 2014

[11] Li Zhang, Brian Curless, and Steven M. Seitz, “Rapid Shape Acquisition Using Color Structured Light and Multi-pass Dynamic Programming”, *IEEE 1st International Symposium on 3D Data Processing Visualization and Transmission*, 2002

[12] Paul M. Griffin, Lakshmi S. Narasimhan and Soung R. Yee, “Generation of Uniquely Encoded Light Patterns for Ranged Data Acquisition”, *Pattern Recognition*, Vol. 25, No. 6, 1992.

[13] Jieli Li, Laurence G. Hassebrook, and Chun Guan, "Optimized two-frequency phase-measuring profilometry light-sensor temporal-noise sensitivity," *J. Opt. Soc. Am. A*, 20(1), 2003.

[14] H. Morita, K. Yajima, S. Sakata, Reconstruction of surfaces of 3-d objects by m-array pattern projection method, in: IEEE International Conference on Computer Vision, 1988, pp. 468–473.

[15] O. Hall-Holt and S. Rusinkiewicz, “Stripe Boundary Codes for Real-Time Structured-Light Range Scanning of Moving Objects,” *Proc. Int’l Conf. Computer Vision*, pp. 359-366, 2001.

[16] C. J. Casey, L.G. Hassebrook and D. L. Lau, “Structured Light Illumination Methods for Continuous Motion Hand and Face-Computer Interaction,” *Human-Computer Interaction, New Developments, International Journal of Advanced Robotic System*, edited by Kikuo Asai, published by In-Tech, Croatia branch of I-Tech Education and Publishing KG, Vienna, Austria, pp 297-308, (copyright 2008) ISBN 978-953-7619-14-5.

- [17] Jaihui Pan, Peisen S. Huang, and Fu-Pen Chiang, “Color-phase shifting technique for three-dimensional shape measurement,” *Optical Engineering -- January 2006 -- Volume 45, Issue 1, 013602*
- [18] M. Maruyama and S. Abe, “Range sensing by projecting multiple slits with random cuts,” *IEEE Trans. Pattern. Anal. Mach. Intell.* 15, 647–651 (1993).
- [19] Ryusuke Sagawa, Ryo Furukawa, and Hiroshi Kawasaki, “Dense 3D Reconstruction from High Frame-Rate Video Using a Static Grid Pattern”, *Submitted to IEEE Transactions on Pattern Analysis and Machine Intelligence, 2013.*
- [20] C. Radhakrishna Rao, “Wiley Series in Probability and Mathematical Statistics”, Chapter 1, Section 1b, John Wiley & Sons, Inc. 1965
- [21] H. Samet and M. Tamminen (1988). "Efficient Component Labeling of Images of Arbitrary Dimension Represented by Linear Bintree". *IEEE Transactions on Pattern Analysis and Machine Intelligence, 1988.*
- [22] Dennis C. Ghiglia, and Mark D. Pritt, “Two-Dimensional Phase Unwrapping – Theory, Algorithms, and Software”, Chapter 4, section 4.2, John Wiley & Sons, Inc. 1998
- [23] H. Zhao, W. Chen, and Y. Tan, “Phase-unwrapping Algorithm for the Measurement of Three-dimensional Object Shapes”, *Applied Optics*, 33, 4497-4500 (1994).
- [24] Daniel L. Lau, Kai Liu, and Laurence Hassebrook, “Real-time three-dimensional shape measurement of moving objects without edge errors by time-synchronized structured illumination”, *Optics Letters*, Vol. 35, No. 14, July 15, 2010.
- [25] Xu Zhang, Limin Zhu, Youfu Li, and Dawei Tu, “Generic non-sinusoidal fringe model and gamma calibration in phase measuring profilometry”, *Opt. Soc. Am. A*, Vol. 29, No. 6, June 2012.
- [26] B. Pan, Q. kema, L. Huang, and A. Asundi, “Phase error analysis and compensation

for non-sinusoidal waveforms in phase-shifting digital fringe projection profilometry”, *Opt. Lett.* 34(4), 2906-2914, 2009.

[27] K. Liu, Y. Wang, D. L. Lau, Q. Hao, and L. G. Hassebrook, “Gamma model and its analysis for the phase measuring profilometry”, *Opt. Lett.* 35(2), 1992-1994, 2010.

[28] Minghao Wang, Laurence G. Hassebrook, “A novel two-pattern full lateral resolution structured light illumination method”, *Optical Pattern Recognition XXV conference, SPIE Defense + Security, May 14, 2014*

[29] De Piero, F. and M. Trivedi, “3D Computer Vision using Structured Light: Design, Calibration, and Implementation Issues”, *Advanced in Computers*, 43, pp. 243-278, 1996

[30] E. Trucco and A. Veri, “Introductory Techniques for 3-D Computer Vision”, Prentice Hall, 1998

[31] J. Weng, P. Cohen, and M. Herniou, “Camera Calibration with distortion models and accuracy evaluation”, *IEEE Trans. Pattern Analysis Machine Intel.*, 14: 965-980, 1992

[32] Faugeras, “Three Dimensional Computer Vision: a geometric approach”, *Cambridge, Mass: MIT Press, 1993*

[33] Yongchang Wang, Kai Liu, Qi Hao, Xianwang Wang, D.L. Lau and L.G. Hassebrook, “Robust Active Stereo Vision Using Kullback-Leibler Divergence,” *IEEE PAMI*, Vol. 34, no. 3, pp. 548-563, March 2012.

[34] Jie-lin Li, “Camera Calibration and Noise Analysis Structured Light Illumination Active Range Finders” (2000). University of Kentucky Master’s Theses.

[35] Y. Wang, K. Liu, Q. Hao, D. L. Lau, and L. G. Hassebrook, “Period coded phase shifting strategy for real-time 3-D structured light illumination acquisition and reconstruction,” *IEEE Trans. Image Proc.*, vol. 20, no. 11, pp. 3001-3013, Nov. 2011.

[36] Charles Casey, L.G. Hassebrook, Eli Crane and Aaron Davidson, “Multi-Feature Distortion-Insensitive Constellation Detection,” *Applied Optics*, Vol. 50, No. 12, pp 1650-1659, April (2011).

- [37] Yongchang Wang, L.G. Hassebrook and D.L. Lau, "Data Acquisition and Processing of 3-D Fingerprints," *IEEE Transactions on Information Forensics & Security*, Vol. 5, No. 4, pp 750-760, December (2010).
- [38] K. Liu, Y. Wang, D. L. Lau, Q. Hao, and L. G. Hassebrook, "A maximum SNR pattern strategy for phase shifting methods in structured light illumination," *J. Opt. Soc. Am. A*, vol. 27, no. 9, pp. 1962-1971, Sept. 2010.
- [39] Kai Liu, Yongchang Wang, Daniel L. Lau, Qi Hao and L. G. Hassebrook, "Dual-frequency pattern scheme for high-speed 3-D shape measurement," *Optics Express*, Vol. 18(5), pp. 5229-5244, March 2010.
- [40] Y. Ohta and T. Kanade, "Stereo by intra- and inner-scanline search using dynamic programming", *IEEE Transactions on Pattern Analysis and Machine Intelligence*, PAMI7(2):139-154, March 1985.
- [41] Wei Su and L. G. Hassebrook, "Pose and position tracking with Super Image Vector Inner Products" *Applied Optics*, Vol. 45, No. 31, pp 8083-8091 (November 2006).
- [42] Jie-lin Li, L.G. Hassebrook and Chun Guan, "Optimized Two-Frequency Phase-Measuring-Profilometry Light-Sensor Temporal-Noise Sensitivity," *JOSA A*, **20**(1), 106-115, (2003).
- [43] W. J. Chmilt and L.G. Hassebrook, "Scene reconstruction from partially overlapping images with use of composite filters," *JOSA A*, **16**(9), 2124-2135, September (1999).
- [44] R. C. Daley and L. G. Hassebrook, "Channel capacity model of binary encoded structured light-stripe illumination," *Applied Optics*, **37**(17), 3689-3696, June (1998).
- [45] M. Wang, J. Evans, L. G. Hassebrook and C. Knapp, "A Multi-Stage, Optimal Active Contour," *IEEE Transactions on Image Processing* , **5**(11), 1586-1591, (November 1996).
- [46] M. Rahmati and L. G. Hassebrook, "Intensity- and Distortion-Invariant Pattern Recognition with Complex Linear Morphology," *Pattern Recognition*, **27**(4), 549-568, (April 1994).

- [47] L. G. Hassebrook, Subramanian and P. Pai, "Optimized Three-Dimensional Recovery From Two-Dimensional Images by Means of Sine Wave Structured Light Illumination," *Optical Engineering*, **33**(1), 219-229, (January 1994).
- [48] L. G. Hassebrook, M. Rahmati and B.V.K. Vijaya Kumar, "Hybrid Composite Filter Banks for Distortion-Invariant Optical Pattern Recognition," *Optical Engineering*, **31**, 923-933, (May 1992).
- [49] L. G. Hassebrook, B.V.K. Vijaya Kumar and L. Hostetler, "Linear Phase Coefficient Composite Filter Banks for Distortion-Invariant Optical Pattern Recognition," *Optical Engineering*, **29**, 1033-1043, (Sept. 1990).
- [50] B.V.K. Vijaya Kumar and L. G. Hassebrook, "Performance Measures for Correlation Filters," *Applied Optics*, **29**, 2997-3006, (July 1990).
- [51] B.V.K. Vijaya Kumar, Z. Bahri and L. G. Hassebrook, "Correlation Filters for Distortion-Invariant Pattern Recognition," *Journal of the Institute of Electronics and Telecommunications Engineer*, **35**(2), 105-113, (1989).
- [52] L. G. Hassebrook, Minghao Wang, Raymond C. Daley, "Performance characterization of structured light based fingerprint scanner," invited paper to be submitted to SPIE International Symposium on Defense and Security + Sensing, Biometric and Surveillance Technology for Human and Activity Identification, Baltimore, Vol. 8712, 871205-(pp. 1-11) May 2013.
- [53] V. Yalla, L. G. Hassebrook, R. Daley, C. Boles and M. Troy, "Full-hand 3D non-contact scanner using sub-window-based structured light-illumination technique," *Proc. SPIE* 8371, Sensing Technologies for Global Health, Military Medicine, Disaster Response, and Environmental Monitoring II; and Biometric Technology for Human Identification IX, 837110 (May 1, 2012).
- [55] Charles Casey and L.G. Hassebrook, "Automated modified composite pattern single image depth acquisition," Three-Dimensional Imaging, Visualization, and Display 2011. *SPIE Defense and Security Symposium*, edited by Bahram Javidi, Jung-Young Son,

Orlando, Florida, Vol. 8043, (May 2011).

[56] V. Yalla, R. Daley, C. Boles, L. Hassebrook, K. Fleming and M. Troy, "High Quality 3D Fingerprint Acquisition Using Novel Sub-window Based Structured Light Illumination Approach," *SPIE Optics and Photonics for Information Processing IV*, edited by Abdul A. S. Awwal, Khan M. Iftekharruddin and Scott C. Burkhart, San Diego, CA, Vol. 7797, 77970R, pp 1-10 (August 2010).

[57] E. R. Crane, L.G. Hassebrook, C.T. Begley, W. F. Lundby and C. J. Casey, "Methodology and Technology for Rapid Three-Dimensional Scanning of In Situ Archaeological Materials in Remote Areas," "Fusion of Cultures," F.J. Melero, P. Cano, and J. Revelles (eds), Granada; pp 51-54, ISBN: 978-84-693-0772-4 (April 2010).

[58] Wei Su, Laurence G. Hassebrook and Siddarth Hariharan, " Facial Feature Tracking with the Super Image Vector Inner Product," *Automatic Target Recognition XVII, SPIE Defense and Security Symposium*, edited by Firooz A. Sadjadi, Orlando, Florida. Vol. 6555, (April 2007).

[59] Yongchang Wang, Kai Liu, Qi Hao, Daniel Lau, and Laurence G. Hassebrook, "Multicamera Phase Measuring Profilometry For Accurate Depth Measurement," *Sensors and Systems for Space Applications, SPIE Defense and Security Symposium*, edited by Richard T. Howard; Robert D. Richards, Orlando, Florida. Vol. 6555, pp 655509-1 to 655509-12, (April 2007).

[60] Wei Su, L.G. Hassebrook and D. L. Lau, "Active Pattern Projection for Increasing Range of Pulsed Range Sensors," Edited by Peter Tchoryk, Jr. and Brian Holz, *SPIE Defense and Security, Spaceborne Sensors II*, Orlando, Florida, Vol. 5798-18, (March 28, 2005).

[61] Veera Ganesh Yalla and L.G. Hassebrook, "Very-High Resolution 3D Surface Scanning using Multi-Frequency Phase Measuring Profilometry," Edited by Peter Tchoryk, Jr. and Brian Holz, *SPIE Defense and Security, Spaceborne Sensors II*, Orlando, Florida, Vol. 5798-09, pp 44-53 (2005).

- [62] Chun Guan, L.G. Hassebrook and D. L. Lau, "Composite Pattern Structured Light Projection for Human Computer Interaction in Space," Edited by Peter Tchoryk, Jr. and Brian Holz, *SPIE Defense and Security, Spaceborne Sensors II*, Orlando, Florida, Vol. 5798-05, (March 28, 2005).
- [63] Chun Guan, L.G. Hassebrook and Daniel Lau, "Optical Processing of Composite Pattern Structured Light Projection for High Speed Depth Measurement," Edited by Bahram Javidi and Demetri Psaltis, *SPIE Symposium on Optical Science and Technology, Optical Information Systems II*, Denver, Colorado, Vol. 5557-5, (August 2004).
- [64] Chun Guan, L.G. Hassebrook and Daniel L. Lau, "Real-Time 3-D Data Acquisition for Augmented Reality Man and Machine Interfacing," Edited by N. L. Faust and W. E. Roper, *SPIE Proceedings on Geo-Spatial and Temporal Image and Data Exploitation III*, Vol. 5097, pp 40-47, (April 2003).
- [65] L. G. Hassebrook, William J. Chimitt, Jr., and Jieli Li, "Registration of Partially Overlapping Images Using Composite Filters," Edited by D.P. Casasent and T.H. Chao, *SPIE Proceedings on Optical Pattern Recognition XI*, (April 2000).
- [66] William J. Chimitt and L. G. Hassebrook, "Automatic scene reconstruction from partially overlapping images using on line filter design," Edited by D.P. Casasent and T.H. Chao, *SPIE Proceedings*, 3386-22, 171-181, (April 1998).
- [67] L. G. Hassebrook, Ray C. Daley and William Chimitt, "Application of Communication Theory to High Speed Structured Light Illumination," Edited by Harding and Svetkoff, *SPIE Proceedings*, **3204**(15), 102-113 (October 1997).
- [68] L.G. Hassebrook, M. Rahmati, R.C. Daley and M.E. Lhamon, "Complex Linear Morphology for Intensity- and Distortion-Invariant Pattern Recognition," *SPIE Proceedings*, **2237**(4), 27-39, (April 1994).
- [69] Robert Sitnik, "Four-dimensional measurement by a single-frame structured light method", *Applied Optics*, Vol. 48, No. 18, 20 June 2009.
- [70] Thibaut Weise, Bastian Leibe and Luc Van Gool, "Fast 3D Scanning with

Automatic Motion Compensation”, 1-4244-1180-7/07, IEEE.

[71] Evan Lally, Jianmin Gong, and Anbo Wang, “Method of Multiple References for 3D imaging with Fourier Transform Interferometry”, *Optics Express*, Vol. 18, No. 17, August 2010.

[72] Sai Siva gorthi, Gannavarpu Rajshekhar, and Pramod Rastogi, “Investigation to realize a computationally efficient implementation of the high order instantaneous-moments-based fringe analysis method”, *Optical Engineering*, Vol. 49, No. 6, June, 2010.

[73] Martin Schaffer, Marcus Grosse, and Richard Kowarschik, “High-speed pattern projection for three-dimensional shape measurement using laser speckles”, *Applied Optics*, Vol. 49, No. 18, June 2010.

[74] Martin Schaffer, Marcus Grosse, Bastian Harendt, and Richard Kowarschik, “Coherent two-beam interference fringe projection for high speed three-dimensional shape measurements”, *Applied Optics*, Vol. 52, No. 11, April 2013.

[75] Marcus Grosse, Martin Schaffer, Bastian Harendt, and Richard Kowarschik, “Fast data acquisition for three-dimensional shape measurement using fixed-pattern projection and temporal coding”, *Optical Engineering*, Vol. 50, No. 10, October, 2011.

[76] Yajun Wang, Song Zhang, “Superfast multifrequency phase-shifting technique with optimal pulse width modulation”, *Optic Express*, Vol. 19, No. 6, March 2011.

[77] Thomas T. Lu, and Tien-Hsin Chao, “A high-resolution and high-speed 3D imaging system and its application on ATR”, *SPIE Symposium on Defense and Security, Optical Pattern Recognition XVII*, 2006.

[78] Deokhwa Hong, Hyunki Lee, Min Young Im, Hyungsuck Cho, and Jeon II Moon, “Sensor fusion of phase measuring profilometry and stereo vision for three-dimensional inspection of electronic components assembled on printed circuit boards”, *Applied Optics*, Vol. 48, No. 21, July 2009.

[79] Katherine Miller, “Communication Theory: Perspectives, Process, and Contexts”,

ISBN: 978-0072937947.

[80] Keller K and Ackerman J, “Real-time structured light depth extraction”, SPIE Photonics Wet-Electronic Imaging, 3158, pp. 11-19, 2000.

[81] J. Proakis and M. Salehi, “Communication Systems Engineering”, 2nd Edition, Prentice Hall, 2002.

[82] R. Kolluri, “Provably Good Moving Least Squares”, Proc. Of the 2005 ACM-SLAM Symposium on Discrete Algorithms, 1008-1018, Vancouver, Canada, January 2005.

[83] T. Weyrich, M. Pauly, R. Keiser, S. Heinzle, S. Scandella and M. Gross, “Postprocessing of 3D Scanned Surface Data”, Proc. Of the Eurographics Symposium on Point-Based Graphics, 2004.

[84] L. W. Couch II, “Digital and Analog Communication System”, Seventh Edition, Prentice Hall, 2001.

[85] V. Yalla, Wei Su, and L.G. Hassebrook, “Multi-spot projection, tracking and calibration”, Optical Pattern Recognition XIV, SPIE’s Aerosense 2003, Vol. 5106-26, 2003.

[86] L. G. Hassebrook, and Daniel L. Lau, “Lock and Hold Structured Light Illumination”, recommended for Patent Application, University of Kentucky Intellectual Property Development CASE 1428, University of Kentucky, August, 2006.

[87] K. Itoh, “Analysis of the phase unwrapping algorithm”, Applied Optics, 21 2470, 1982.

[88] N. G. Durdle, J. Tayyoor and V. J. Raso, “An improved structured light technique for surface reconstruction of the human trunk”, IEEE Canadian Conference on Electrical and Computer Engineering, 2, 874-877, 1998.

[89] T. Strand, “Three-Dimensional Sensing for Machine Vision”, Optical Engineering, 24, 33-40, 1985.

- [90] S. Zhang, "Recent progresses on real-time 3-D shape measurement using digital fringe projection techniques," *Opt. Laser Eng.*, 48(2), 149-158 (2010)
- [91] S. Zhang, "High-resolution 3-D profilometry with binary phase-shifting methods," *Appl. Opt.*, 50(12) 1753-1757 (2011).
- [92] Yang Wang, M Gupta, S Zhang, S Wang, X Gu, D Smaras, P Huang, "High resolution tracking of non-rigid motion of densely sampled 3D data using harmonic maps", *International Journal of Computer Vision*, Vol. 76, No. 3, pp 283-300, 2008.
- [93] L. Ekstrand and S. Zhang, "3-D profilometry with nearly focused binary phase-shifting methods," *Opt. Lett.* 36(23) 4518-4520 (2011).
- [94] Guan Chun, "Composite pattern for single frame 3D acquisition", University of Kentucky Doctoral Dissertation.
- [95] Charles Casey, "Enhancement to the Modified Composite Pattern method of Structured Light 3D capture" (2011), University of Kentucky Doctoral Dissertation. Page 226.
- [96] Eli Crane, "Rotate and Hold and Scan (RAHAS): Structured Light Illumination in the Rio Platano Biosphere, Honduras" (2011) University of Kentucky Master's Thesis. Page 119.
- [97] Pethe, Akshay, "Super resolution 3d scanning using spatial light modulator and band correction" (2008). University of Kentucky Master's Theses. Page 550.
- [98] Cavaturu, Raja Kalyan Ram, "Motion Correction Structured Light using Pattern Interleaving Technique" (2008). University of Kentucky Master's Theses. Page 551.
- [99] D. Nister. Automatic Dense Reconstruction from Uncalibrated Video Sequences. PhD Thesis, Royal Institute of Technology KTH, Stockholm, Sweden, ISBN 91-7283-053-0, 2001.
- [100] Liang Wang, "Novel Dense Stereo Algorithms for High-quality Depth Estimation

from Images” (2011). University of Kentucky Doctoral Dissertation.

[101] R. Hartley and A. Zisserman, “Multiple View Geometry in Computer Vision”, Cambridge University Press, ISBN: 0521623049, 2000.

[102] Pierre Payeur and Danick Desjardins, “Structured light stereoscopic imaging with dynamic pseudo-random noise patterns”, Image analysis and recognition, Vol. 5627, pp 687-699, 2009.

VITA

Minghao Wang received his B.S in Electrical Engineering from Beihang University in 2011. Since then Minghao has pursued a Ph.D in Electrical and Computer Engineering at University of Kentucky. His research interests include Structured Light Illumination, Computer Vision, Image Processing, and Digital Signal Processing.